Study of Optical and Radiative Properties of Inhomogeneous Metallic Structures

by

Rajagopalan Ramesh

A Dissertation Presented in Partial Fulfillment
of the Requirements for the Degree
Doctor of Philosophy

Approved July 2022 by the
Graduate Supervisory Committee:

Liping Wang, Co-Chair
Bruno Azeredo, Co-Chair
Hongbin Yu
Patrick Phelan
Konrad Rykaczewski

ARIZONA STATE UNIVERSITY

August 2022

ABSTRACT

The objective of this dissertation is to study the optical and radiative properties of inhomogeneous metallic structures. In the ongoing search for new materials with tunable optical characteristics, porous metals and nanowires provides an extensive design space to engineer its optical response based on the morphology-dependent phenomena.

This dissertation firstly discusses the use of aluminum nanopillar array on a quartz substrate as spectrally selective optical filter with narrowband transmission for thermophotovoltaic systems. The narrow-band transmission enhancement is attributed to the magnetic polariton resonance between neighboring aluminum nanopillars. Tuning of the resonance wavelengths for selective filters was achieved by changing the nanopillar geometry. It concludes by showing improved efficiency of Gallium-Antimonide thermophotovoltaic system by coupling the designed filter with the cell.

Next, isotropic nanoporous gold films are investigated for applications in energy conversion and three-dimensional laser printing. The fabricated nanoporous gold samples are characterized by scanning electron microscopy, and the spectral hemispherical reflectance is measured with an integrating sphere. The effective isotropic optical constants of nanoporous gold with varying pore volume fraction are modeled using the Bruggeman effective medium theory.

Nanoporous gold are metastable and to understand its temperature dependent optical properties, a lab-scale fiber-based optical spectrometer setup is developed to characterize the in-situ specular reflectance of nanoporous gold thin films at temperatures ranging from 25 to 500 ^{o}C. The in-situ and the ex-situ measurements suggest that the

specular, diffuse, and hemispherical reflectance varies as a function of temperature due to the morphology (ligament diameter) change observed.

The dissertation continues with modeling and measurements of the radiative properties of porous powders. The study shows the enhanced absorption by mixing porous copper to copper powder. This is important from the viewpoint of scalability to get end products such as sheets and tubes with the requirement of high absorptance that can be produced through three-dimensional printing.

Finally, the dissertation concludes with recommendations on the methods to fabricate the suggested optical filters to improve thermophotovoltaic system efficiencies. The results presented in this dissertation will facilitate not only the manufacturing of materials but also the promising applications in solar thermal energy and optical systems.

ACKNOWLEDGMENTS

I would like to express my utmost gratitude to Dr. Liping Wang and Dr. Bruno Azeredo for guiding me through my PhD, providing valuable insights and direction throughout the process. I would also like to thank Dr. Phelan, Dr. Milcarek, Dr. Rykaczewski and Dr. Yu for agreeing and being a valuable part of the Graduate committee.

I would like to thank my colleagues and friends at Arizona State University for their support and friendship. I would especially like to thank Dr. Qing Ni, Dr. Linshuang Long, Dr. Jui-Yung Chang, Dr. Sydney Taylor, Dr. Payam Sabbaghi, Stanislau Niauzorau, Aliaksandr Sharstniou, Natalya Kublik, Ram Teja Kondakindi, Ryan McBurney, Amm Hasib, Emmanuel Dasinor, Chaitanya Potaraju, Praneeth Mudunuri, Sai Gomath Swaminathan and Phanindra Guthi for the fruitful discussions both academically and on personal level.

I could not have pursued a career in academia without the important counsel from my parents, fiancée, and close family members, who supported me through all the endeavors.

Finally, I would like to thank Arizona State University for their financial support with the PhD scholarships and Fellowships.

This work was supported in part by Air Force Office of Scientific Research under Grant No. FA9550-17-1-0080 and National Science Foundation under Grant No. CMMI-19328.

TABLE OF CONTENTS

Page

LIST OF TABLES vi

LIST OF FIGURES vii

CHAPTER

1 BACKGROUND AND MOTIVATION 1

1.1 Overview of Thermophotovoltaic Systems 1

1.2 Nanoporous Metals with Morphology Dependent Radiative Properties 3

1.3 In-situ Temperature Dependent Characterization of Nanoporous Gold 4

1.4 Optical Characterization of Porous Powders 5

1.5 Primary Objective of the Dissertation 6

2 DESIGN OF SELECTIVE METASURFACE FILTER FOR THERMOPHOTOVOLTAIC ENERGY CONVERSION 8

2.1 State-of-the-art Selective Filters 9

2.2 Selective Metasurface Filter Design and Simulation 10

2.3 Elucidation of Magnetic Polariton Effect 13

2.4 Geometric Dependence of Magnetic Polariton Resonance 17

2.5 Effects of Incidence Angle and Polarization 19

2.6 Theoretical Analysis of Thermophotovoltaic System Performance 20

3 NANOPOROUS GOLD THIN FILMS 27

3.1 Introduction 27

3.2 Sample Fabrication and SEM Characterization 28

3.3 Experimental Method of Optical Characterization 34

CHAPTER Page

3.4 Optical Model 37

3.5 Modeled and Measured Reflectance Comparison 40

4 IN-SITU TEMPERATURE DEPENDENT OPTICAL CHARACTERIZATION AND MODELING OF DEALLOYED THIN-FILM NANOPOROUS GOLD ABSORBERS 49

4.1 Lab-scale Fiber-optic Reflectance Measurement Equipment 50

4.2 Thermal Annealing and Ligament Coarsening 53

4.3 Room Temperature Hemispherical and Diffuse Reflectance 55

4.4 In-situ Temperature Dependent Specular Reflectance 57

4.5 Theoretical Model 59

4.6 Surface Roughness Dependent Reflectance 60

5 RADIATIVE PROPERTIES OF POROUS POWDERS 66

5.1 Optical Model 66

5.2 Optical Characterization of Powder Mixtures 74

6 CONCLUSIONS AND RECOMMENDATIONS 81

REFERENCES 84

APPENDIX

A OPTICAL FILTER 94

B NANOPOROUS GOLD THERMAL PROPERTIES AND HEATER SETUP 105

C POWDER OPTICAL MODEL SUPPORTING MATERIAL 116

LIST OF TABLES

Table Page

1. Dealloying Temperature, Dealloying Time, Pore Diameter, Pore Area Fraction, Residual Silver Content, and PVF of the Fabricated Nanoporous Gold Samples 34

2. Initial and Final Ligament Diameter, Maximum Sample Heating Temperature, Pore Diameter, Pore Area Fraction, Residual Silver Content, and Apparent Pore Volume Fraction (*f*) of the Fabricated NPG Samples 54

LIST OF FIGURES

Figure Page

1. (a) Schematic of the Proposed Aluminum Nanopillars Metasurface Filter on Quartz Substrate Showing Wave Propagation at Normal Incidence. (b) Two-dimensional Schematic of the Proposed Alnp Metasurface Filter Structure on a Thick Quartz Substrate with Thickness of d_s and the Wave Propagation at Oblique Angles of Incidence.. 10
2. The Spectral Reflectance, Transmittance, and Absorptance of the Selective Metasurface Filter at Normal Incidence for TM Polarized Light Based on FDTD Simulations with Nanopillar Diameter, d = 370 nm with Period, a = 450 nm and height, h = 700 nm. 13
3. (a) The LC Circuit Model Based on Charge and Field Distribution and the Electromagnetic Field Distribution Contour Plots on the x–y Plane when MP Resonances are Excited at Wavelengths (b) 1.9 μm, (c) 0.93 μm, and (d) 0.54 μm. 16
4. The Spectral Transmittance with Respect to Different Nanopillars: (a) Diameter, (b) Height and (c) Period Simulated by FDTD. The MP1 Wavelengths Predicted by FDTD, and LC Circuit Model with Respect to Different Nanopillars: (d) Diameter, (e) Height and (f) Period with Fixed Base Values of d = 370, a = 450 nm, and h = 700 nm. 18
5. Theoretical Spectral Transmittance of the Proposed AlNP Metasurface Filter at Different Incident Angles for (a) TM and (b) TE Polarizations. 20

Figure Page

6. (a) Schematic of a Simple TPV System Consisting of an Emitter, Optical Filter, and a Cell, (b) Spectral Absorptance of the Gasb Cell, (c) Spectral Emittance of a Black Emitter, and (d) Spectral Transmittance of an Ideal Broadband and Narrowband Optical Filter to Transmit the Light with Energy above the Band Gap of the Cell. 21

7. (a) Spectral Efficiency, (b) TPV Efficiency, (c) Net Radiative Heat Flux and (d) Output Power at Different Emitter Temperatures from 1000 K to 2000 K with Theoretical AlNP Metasurface Filter, and Black Emitter paired with a Gasb Cell. 26

8. (a) Top-view and (b) Cross-sectional Sem Images of Fabricated Nanoporous Gold Thin-film Samples with Varying Pore Diameters and Apparent Pore Volume Factions (*f*) as Listed in Table 1: Sample 1 (S1, f = 45%), Sample 2 (S2, f = 53%), Sample 3 (S3, f = 56%), Sample 4 (S4, f = 58%), Sample 5 (S5, f = 59%), Sample 6 (S6, f = 60%), Sample 7 (S7, f = 60%), and Sample 8 (S8, f = 60%). The Scale Bar is 200 nm for all the SEM Images. 30

9. Correlations Between the Fabrication Conditions and Morphology for Fabricated Nanoporous Gold Samples: (a) the Residual Silver Content Dependence on the Dealloying Time; (b) Average Ligament Diameter Dependence on the Dealloying Time; (c) Average Pore Diameter Dependence on the Dealloying Time; (d) Pore Area Fraction Dependence on the Pore Diameter; (e) Pore Area Fraction Dependence on the Dealloying Time; and (f) Pore Volume Fraction Dependence on the Dealloying Time. 32

Figure Page

10. (a) Optical Schematic to Illustrate the Working Principle of the Tunable Light Source and the Integrating Sphere (IS) for Spectral-directional Hemispherical Reflectance Measurement. (b) Photo of the 8° Sample Mount at the Back Side of the IS with a Heater and a Thermocouple for Temperature-dependent Measurement in Air from Room Temperature up to 100 °C. (c-1) Photo of the Center Mount for Oblique Incident Angle Measurement. (c-2) Photo of the Monochromatic Light Focused on the Sample Mounted on the Center Stage. (c-3) Photo of the Optical Polarizer Used for TE or TM Polarization Selection. (c-4) Photo of the Radial Dial on the Center Sample Mount for Selecting the Incidence Angle θ_i. 35
11. Schematic of a Nanoporous Gold Film with Isotropic Pores in Gold Matrix with an Effective Dielectric Function $\mathcal{E}_{2,\text{eff}}$ from the Effective Medium Theory. The Light is Incident from Air ($\mathcal{E}_1 = 1$) at an Angle of θ_i and Wavelength λ with the Spectral Reflectance R_λ. As the Layer Thickness Is Much Larger than the Penetration Depth, the Nanoporous Gold Layer Is Considered to Be Semi-infinite here. 39
12. (a) Optical Measurements of Spectral Near-normal Hemispherical Reflectance of Fabricated Nanoporous Gold Samples with Different Pore Volume Fractions at Room Temperature. (B) Predicted Spectral Normal Reflectance of Semi-infinite Nanoporous Gold with Different Pore Volume Fractions from the Optical Modeling. 42

Figure Page

13. (a) Refractive Index *n*, (b) Extinction Coefficient *k*, (c) Penetration Depth δ of the Nanoporous Gold in the Wavelength Range From 0.4 to 1.6 μm Calculated from the BR Effective Medium Theory at Different Volume Fractions *f* of Air Pores from 40% to 65%. 43
14. Optical Measurements of Spectral Directional Hemispherical Reflectance of Fabricated Nanoporous Gold (Sample 1) at Different Incident Angles for (a) TE and (b) TM Polarized Waves. Modelled Spectral Directional Reflectance of Semi-infinite Nanoporous Gold with Volume Filling Ratio *f* = 45% at Different Incident Angles for (c) TE and (d) TM Polarized Waves, and Angular Reflectance as a Function of Incidence Angle for Both Polarizations at the Selected Wavelengths of (e) λ = .5 μm and (F) λ = 1 μm..... 47
15. Temperature-dependent Spectral Near-normal Hemispherical Reflectance in the Visible and Near-infrared Spectral Range from Room Temperature up to 100 ^{o}C for Fabricated Nanoporous Gold: (a) Sample 2 (S2) and (b) Sample 3 (S3)..... 48
16. (a) Optical Layout of the High-temperature Reflectance Measurement Setup Consisting of a QTH Light Source, a Heater Assembly, a CCD Spectrometer, Optic Fibers, and a Collimator. (b) QTH Lamp and CCD Spectrometer Connected to Either Ends of the Bifurcated Fiber Cable. (c) Collimator Focusing Light on the Sample Mounted Inside the Heater Assembly. 52
17. Top View SEM Images of Fabricated NPG Thin-film Samples Dealloyed at 40 ^{o}C for 30 min before and after Heating: S1 (125 ^{o}C), S2 (200 ^{o}C), S3 (275 ^{o}C), S4 (350 ^{o}C), and S5 (500 ^{o}C)..... 55

Figure Page

18. Room-temperature Optical Measurements of Spectral Near-normal Reflectance of Fabricated NPG Samples Dealloyed at Same Conditions Pre- and Post-heat Treatment: (a) Hemispherical and (b) Diffuse Reflectance at Near-normal Incidence. Solid and Dashed Lines Correspond to Measurements Made before and after the Heating Cycle. T_{max} Indicates the Maximum Temperature During the Heating Cycle..... 56

19. In-situ Optical Measurements of Spectral Near-normal Specular Reflectance of Fabricated NPG Samples Heated to Different Temperatures as Listed in Table 2: (A) Sample 1 (S1, T= 125 ^{o}C), (B) Sample 2 (S2, T= 200 ^{o}C), (C) Sample 3 (S3, T= 275 ^{o}C), (D) Sample 4 (S4, T= 350 ^{o}C), and (E) Sample 5 (S5, T= 500 ^{o}C) Using the Fiber Optic Setup. 58

20. (a) Plot Relating the Relative Specular Reflectance at Fixed Wavelength of 1μm Varying with Temperature and Ligament Diameter for 5 Samples Exposed to Different Maximum Temperatures. (b) Arrhenius Plot Containing the Ligament Diameter after Coarsening for Short Durations at Elevated Temperatures (600-1200 Sec). The Blue Line Is the Linear Fit, Whose Slope Equals $-nE_a$ and the Intercept Equals $\ln[(kD_0)]^n$..... 62

Figure Page

21. (a) Predicted Spectral Specular Normal Reflectance of Semi-infinite NPG with Root-mean-square Roughness Values from the Optical Modeling. (b) Plot Relating the Relative Specular Reflectance at Fixed Wavelength of 1μm Varying with Final Ligament Diameter and Hence Surface Roughness for 5 Samples Exposed to Different Maximum Temperatures Considering Initial Surface Roughness of the Samples σ_i = 20 nm. 63
22. Flowchart Depicting the Modeling Process to Calculate the Powder Mixture Reflectance. 67
23. (a) Homogeneous Dense Material and (b) Powder Bed Hemispherical Reflectance Measurement Layout Where D Is Base Diameter of the Conic Detector; L, Distance Between the Detector and the Sample; And Θ, Maximum Reflection Angle of Collected Radiation. 70
24. Schematic of a Particle Bed Sandwiched Between Two Transparent Window Materials, and the Ray-tracing Diagram of Multiple Reflections by the Window and Particle Bed (which Is Thick Enough to Be Opaque). 74
25. (a) Measured and Calculated Reflectance and Transmittance of Glass Window From .38 μm to 1.8 μm (Literature). (b) Calculated Reflectance and Transmittance of Glass Window from 1000 nm to 2500 nm using Ray Tracing Model. 76
26. (a) Measured Sample Hemispherical Reflectance of the Sample Consisting of the Powder Bed Sandwiched Between Glass Slides. (b) Calculated Hemispherical Reflectance of the Powder Bed Particles from the Measured Sample Reflectance and Calculated Thick Glass. 77

Figure Page

27. (a) Calculated Surface Area Fractions of Copper and Porous Copper Powder Particles Varying with Weight Fraction of Porous Copper Calculated Using Copper (Particle A) and Porous Copper (Particle B) Measured Apparent Density Values of of ρ_A = 8.96 g/cm^3, ρ_B = 1.3 g/cm^3 and Diameters d_A=30 μm and d_B=10 μm. The Calculated Hemispherical Reflectance Values Using Model 1 and 2 Compared to Measured Values at Wavelength (b) 1.07 μm, and (c) 2 μm. (d) the Error Percentage Between Calculated and Measured Reflectance Values Using Model 2. 78

28. (a) The Measured Reflectance of Mixtures with Varying Fractions of Copper and Porous Copper Powders Using an Integrating Sphere. (b) Calculated Reflectance of Powder Mixtures Using the Linear or the Checkerboard Model. (c) the Error Percentage Between Calculated and Measured Reflectance Values Using Model 1. 80

29. The Spectral Absorptance of the Selective Absorber Varying with Nanowire Height Based on FDTD Simulation from (a) Literature and (B) Current Modeling. 96

30. The Spectral Reflectance, Transmittance, and Absorptance of the Selective Metasurface Filter at Normal Incidence for TM Polarized Light Based on (a) HFSS and (b) FDTD Simulations with Nanopillar Diameter, *d* = 370 Nm with Period, *a* = 450 nm and Heigh, *h* = 700 nm. 98

31. (a) the Refractive Index (*n*) and Extinction Coefficient (*k*) of Gasb Cell Obtained from Adachi. (b) the IQE of GaSb Cell Used in the Study Obtained from Tang et al. 99

Figure Page

32. (a) Spectral Efficiency (Literature), (b) TPV Efficiency (Literature), (c) Spectral Efficiency (Current Calculation) and (d) TPV Efficiency (Current Calculation) at different Emitter Temperatures from 800 K to 1200 K with Theoretical Ge-based Emitter, Fabricated Ge-based Emitter and Black Emitter Paired with a Gasb Cell. 100
33. The Spectral Absorptance with Respect to Different Nanopillars: (a) Diameter, (b) Height and (c) Period Simulated by FDTD. The MP1 Wavelengths Predicted by FDTD, and LC Circuit Model with Respect to Different Nanopillars: (d) Diameter, (e) Height and (f) Period. 101
34. (a) Spectral Efficiency, (b) TPV Efficiency, (c) Net Radiative Heat Flux and (d) Output Power at Different Temperatures from 1000 K to 2000 K with Theoretical AlNP Metasurface Filter, and Black Emitter Paired with a Gasb Cell for Different Below Band gap Absorptance of the Cell. 103
35. Convergence Plot for FDTD Comparing the Absorptance of the Metasurface Structure for Mesh Sizes 3, 4 and 5 nm. 104
36. (a) Initial Ag-au Alloy after Co-sputtering with 60% of Ag by Volume. (b) Porous Gold Layer after Dealloying for 30 Mins at 40 ^{o}C Containing 1-3% of Residual Silver Content. 106
37. In-situ Temperature Measurement Setup and Heat Transfer Model. (a) Illustration of the Sample Holder Setup. (b) Equivalent Thermal Resistance Network. 108

Figure Page

38. Validations of Spectral Optical Reflectance Measurements with the Integrating Sphere in Comparison with Theoretical Modelling: (a) Spectral Near-normal Hemispherical Reflectance of Undoped Silicon Wafer at Room Temperature; (b) Spectral Directional Hemispherical Reflectance of Undoped Silicon Wafer at Multiple Incidence Angles (I.E., 10º, 30º, 45º, and 60º) for TE Polarized Waves and (c) TM Polarized Waves. 109
39. Near Normal Specular Reflectance of Lightly Doped Silicon Measured Using the In-situ Temperature Dependent Reflectance Fiber-optic Setup Compared to the Theoretical Value. 110
40. (a) Front View of the Nickel-plated Copper Disk with Diameter 1.688 Inch Containing 4 thru Threaded Holes to Attach the Sample and 4 thru Holes to Fasten to the Steel Base. (b) Isometric View of the Heater Setup Encapsulated by Firebrick. (c) Exploded View Showing Cartridge Heater, Fire Brick, Steel Base and Nickel-plated Copper Disk. (d) Side View of the Heater Setup Showing the Press Fitted Cartridge Heater, Fire Brick, and Steel Base. 111
41. Temperature Histogram of Sample (a) 1, (b) 2, (c) 3, and (d) 5 112
42. Time Dependent Specular Reflectance of Samples Measured at 0,2 and 5 Mins at the Maximum Exposed Temperature (a) S1-125 ºC, (b) S2-250 ºC, (c) S3-275 ºC, (d) S4-350 ºC and (e) S5-500 ºC 113

Figure Page

43. (a) Refractive Index N, (b) Extinction Coefficient K of the Nanoporous Gold in the Wavelength Range from 400 to 1000 nm Calculated from the BR Effective Medium Theory at Different Temperatures for a Fixed Volume Fraction of f = 58%..... 114

44. Predicted Spectral Normal Reflectance of Semi-infinite Nanoporous Gold (a) with Varying Dielectric Function of Gold Thin Film as a Function of Temperature (b) with Different Pore Volume Fractions of the Samples from the Optical Modeling. 115

45. XRD Data for Porous Copper Powder Suggesting the Presence of 46.1% of Cu_2O by Weight. 117

46. Schematic of Porous Copper and Copper Powder Mixture Reflectance Calculation Using the Checkerboard Method. 118

47. Sensitivity Analysis Showing the Reflectance of a Function of Varying Weight Fractions of Porous Copper in the Powder Mixture for Changing d_b from 5-25 μm and fixed d_a of 30 μm Using (a) Model 1 (B) Model 2 and changing d_a from 15-45 μm and Fixed d_b of 10 Mm Using (a) Model 1 (B) Model 2 at a Wavelength of 2 μm. 120

48. Sensitivity Analysis Showing the Reflectance of a Function of Varying Weight Fractions of Porous Copper in the Powder Mixture for Changing d_b from 5-25 μm and fixed d_a of 30 μm Using (a) Model 1 (B) Model 2 and changing d_a from 15-45 μm and Fixed d_b of 10 Mm Using (a) Model 1 (B) Model 2 at a Wavelength of 1.07 μm. 121

CHAPTER 1

BACKGROUND AND MOTIVATION

1.1 Overview of Thermophotovoltaic Systems

A thermophotovoltaic cell (TPV) system uses photovoltaic effect to convert the thermal infrared radiation from an emitter into electricity. The TPV system is composed of a thermal emitter, a selective filter and a photovoltaic cell [1]. The temperature for the emitter ranges between 1000 and 2000 K which is usually optimal for a cell with a bandgap range 0.5-0.75 eV [1], [2]. TPV energy conversion system allows recycling of the waste heat and improves the thermal to electricity conversion efficiency [3]–[6]. Potential use of TPV systems include nuclear power generation for space applications [7], hybrid electric vehicles [8], industrial and home power supplies [9], waste heat recovery [10], solar photovoltaic systems [11] and portable electric generators [12].

The maximum theoretical efficiency of a TPV system is constrained by the radiative limit [2], [13], but this number is not achievable due to practical limitations such as low output power generation and poor conversion efficiency, partly due to the radiation spectrum mismatch between the thermal radiation spectrum of the emitter and absorption spectrum of the cell. In 2014, Fraas et al.[14] projected a TPV planar module performance for steel industry application at 1400 K and 1500 K blackbody temperature with 20% efficiency and output power of 1.8 W/cm^2. Subsequently, a cell efficiency of 29% with an electric power of 1.5 W/cm^2 for a single Gallium Antimonide (GaSb) cell measured under 1548 K radiator temperature was reported [14]. Tan et al.[15] compared the performance of $In_{0.53}Ga_{0.47}As$ and $In_{0.68}Ga_{0.32}As$ and demonstrated that the cells obtained an efficiency of 16.4% and 19.1% at 1323 K blackbody temperature, respectively. Recent

demonstrations show TPV cell efficiency ≥ 30% using two different cell materials at different thermal emitter temperatures surpassing 1500 K [16]. Highest conversion efficiency of more than 40% has been demonstrated with TPV systems consisting of two-junction cells made of III-V materials with bandgaps between 1.0 and 1.4 eV [17]. The cells exploited the edge-spectral filtering using highly reflective back surface reflectors to reject sub-bandgap radiations and were optimized for emitter temperatures of 1,900–2,400 °C.

To further improve the TPV cell performance, research has been done on designing selective emitters and optical filters. Selective and broadband emitters are the two most common types of emitters used in TPV applications. Broadband emitters follow the Planck's law [18] and emit photons across broad range of wavelengths whereas selective emitters are designed to emit photons within a certain wavelength range. Bendelela et al. [19] presented a TPV system with a metamaterial acting as the selective emitter. For a blackbody temperature of 1500 and 300 ^{o}C, a combination of InAs/GaInAsSb TPV tandem cell yielded conversion efficiencies of 41% and 11.82%, respectively. TPV system efficiency of 40% was reported by integrating indium-tin oxide plasmonic emitter with InAs cell delivering a power density of 11 W/ cm^2 at an emitter temperature of 900 K [20].

While great progress has been reported recently to achieve spectrally selective thermal emitters made of photonic crystals [21], metamaterials and multilayers [22], a wavelength selective optical filter [23] is another possible route to increase the TPV efficiency by reflecting photons below the bandgap and selectively transmitting photons above the bandgap into the TPV cell [2]. The incorporation of a selective filter into a TPV system provides a benefit in terms of spectral shaping and control of the emitter's spectral

output. Reducing extremely high energy photons to a range just above the TPV cell bandgap energy may minimize thermalization losses and therefore improve cell conversion efficiency [2], [24]. Moreover, the temperature stability of material is of concern for selective emitters compared to selective filters that operate at lower temperatures. Selective filters also have easier fabrication process than compared to selective cells making them the best choice for spectral control.

Extensive research has been ongoing to understand the application of isotropic and uniaxial metamaterials as spectrally selective filters, emitters, and absorbers for solar thermal and optical thermal energy conversion. The objective in this part of the dissertation is to design a nanopillar based metasurface filter. The designed metasurface filter taps into resonating the magnetic polaritons to obtain enhanced narrowband transmission. The current design provides a way to fabricate narrow band filters at low cost.

1.2 Nanoporous Metals with Morphology Dependent Radiative Properties

Mesoporous metal thin films have drawn significant interest in the last 20 years due to their high surface area and electrical conductivity coupled with chemical stability and rich modulation of its surface chemistry, yielding applications in energetics [25], carbon sequestration [26], and electrochemical sensing [27]. Among nanoporous metals, nanoporous gold (NPG) has received great attention due to its facile chemical synthesis and morphology tunability as its ligament and pore sizes can be reduced to the sub-100 nm range. Therefore, its optical, mechanical and chemical behavior can be tailored (e.g. size-dependent plasmonic resonance and surface plasmon polaritons (SPPs) [28]). These optical characteristics have been exploited to construct sensing devices for gas detection and

catalysis [29], to create substrates for surface-enhanced Raman scattering (SERS) [30], [31], and enhanced luminescence in emitters for thermophotovoltaics [32], [33]. In the ongoing search for new materials with tunable absorption, transmission and radiation characteristics, NPG provides an extensive design space to engineer its optical response based on the morphology-dependent phenomena, however, its structure-property relationships have not been extensively explored [34], [35].

At the center of exploiting the morphology of NPG in the aforementioned applications is its ability to be controlled through advanced synthesis methods, including dealloying with selective dissolution from colloidal precursor mixtures [36], anodization [37], electrochemical deposition onto sacrificial scaffolds [38], hydrogen bubble dynamic template synthesis [39], ultra-thin porous sputtered layers [40], spray deposition of gold nanoparticles [25], [41], [42] and evaporation-induced self-assembly of colloidal crystals [37]. In the process of dealloying, the pore diameter and the pore volume fraction (PVF) can be modified by controlling the dealloying conditions such as temperature, time and the relative contents of the alloy elements [26], [31], [35], [43]–[45]. Unlike nanoparticles, nanoporous metals are only metastable and understanding its morphology evolution during sintering and laser matter interactions remains relevant for both its synthesis and applications. Hence a comprehensive temperature dependent optical study of NPG is required.

1.3 In-situ Temperature Dependent Characterization of Nanoporous Gold

The optical properties of bulk metal materials at elevated temperatures have been previously studied via in-situ monitoring of reflected or transmitted light [13,16].

Investigations have correlated the ligament diameter of NPG thin films as a function of temperature through a well-known Arrhenius relationship [35], [44].

Annealing beyond 100°C activates adatom surface diffusion which leads (i) to coarsening of the pore and ligament sizes in NPG and, consequently, to a decrease in the refractive index (n) at wavelengths greater than 500 nm associated with the NPG structure as the ligaments coarsens and its n-index approaches that of bulk [35]. At the same time, an increase in extinction coefficient (k) in the entire visible wavelength range occurred during its coarsening which is a shift towards k-values for bulk gold [35]. Further, this heat treatment introduces surface roughness during annealing due to coarsening of its structure which affects the optical properties of NPG. In previous studies of sintering of solid Au thin-films, its surface roughness (ranging from 2.6 nm to 4.5 nm) and grain size were used to model and understand its specular reflectance [46], however that has never been employed for NPG thin films which possess much higher root-mean-square values (e.g. 19 to 150 nm).

To further extend this study on the absorbers based on porous metals, and to improve their scalability to produce large objects through 3D printing, we need to understand the optical properties of these metals and porous metals in their powdered form.

1.4 Optical Characterization of Porous Powders

Laser powder bed fusion (L-PBF) is a kind of additive manufacturing (AM) in which a small layer of powder is placed on a baseplate and a design is created by a laser. New layers are added, and the melting process is repeated, resulting in the formation of a 3D structure layer by layer [47], [48]. This technique has piqued the scientific community's

interest due to its ability to create component geometries that would be difficult to create using traditional processing methods [49]. Additionally, materials with metastable phases or microstructures that vary spatially can also be produced [50], [51]. With target applications including heat exchangers, induction [49], and electric motor [50] coils as well as radio frequency cathodes, there has been an interest in manufacturing various defect free parts from copper, gold and silver alloys using L-PBF [48].

This is however challenging due to the high optical reflectivity in the near infrared spectra (>95%) and thermal conductivity (400 W/m·K) of copper. Most of the input energy into the system either gets reflected or quickly dissipated away [51]. The components have somewhat a high amount of porosity when processing copper powder at the laser powers available in many commercial L-PBF equipment, which are generally between 200 and 400 W [52], [53]. Copper's L-PBF processability has recently been improved by covering the powder's surface with materials that have a greater absorptivity. This was accomplished by oxidizing the surface of the copper [54], which led to lower porosity. Another method tried was mixing the copper powder with carbon nanoparticles [55]. This method did not have any significant effect on the porosity [55]. In this search for methods to produce defect free copper parts and to control the optical reflectivity of the powders and the end product of L-PBF, optical properties of porous copper powder and its mixture with copper powders were studied as a part of this dissertation.

1.5 Primary Objective of the Dissertation

The primary objective of this dissertation is to study and comprehend the underlying physics of uniaxial and isotropic metamaterials to use them in energy harvesting

systems and 3D printing for process improvement. The dissertation is organized as follows: Chapter 2 investigates the use of uniaxial nanopillar metasurface on a quartz substrate as a spectrally selective narrowband filter for TPV systems. The chapter discusses the underlying physics behind the selective narrowband transmission and ways to tailor it for a specific requirement. This chapter also analyzes the theoretical performance of a TPV system coupled with the designed metasurface filter. Chapter 3 delves into the room temperature optical characterization of nanoporous metals. It discusses how nanoporous gold thin films can be easily fabricated by chemical dealloying. It deeply explores the change in the optical properties due to the change in the porosity introduced in the gold thin films. Chapter 4 discusses the temperature dependent optical properties of nanoporous gold thin films. The chapter also discusses a measurement technique developed to study the in-situ temperature dependent specular reflectance in the visible to NIR wavelength range. This chapter also includes the temperature dependent measurement results of the fabricated nanoporous gold samples with a focus on structure-property relationship. Chapter 5 presents for a way to improve the absorptance of metal powders for applications in L-PBF. This chapter also discusses an optical model to analytically calculate reflectance in powder mixtures to compare with experimental results. It includes the measurement results of powdered copper, porous copper and their mixtures reflectance compared to the results obtained analytically from the optical model. Finally, Chapter 6 summarizes the findings from the investigations on metamaterials and porous structures reported in Chapters 2, 3, 4, and 5, along with possible future directions of research based on results from those studies.

CHAPTER 2

DESIGN OF SELECTIVE METASURFACE FILTER FOR THERMOPHOTOVOLTAIC ENERGY CONVERSION

In this chapter, we numerically design a selective metasurface filter made of an aluminum (Al) nanopillar array on quartz substrate to achieve spectrally selective transmission above the bandgap of TPV cell and theoretically analyzed its effect on the TPV performance. Full-wave numerical simulations were performed to determine the appropriate nanopillar diameter, period, and height such that the resulting Al nanopillar array will show narrowband transmission at a wavelength of 1.9 μm, which is the bandgap of a commercial GaSb TPV cell. Numerical simulations indicate that the narrow-band transmission is due to the presence of magnetic resonance between neighboring Al nanopillars, which channels energy through at wavelengths near the resonance. Magnetic polariton (MP) refers to the coupling between incident electromagnetic wave and internal magnetic resonance inside the structure. Although magnetic resonance in micro/nanostructures result in enhanced absorptivity or emissivity, increased transmission could also occur at nearby resonant frequencies for those on transparent substrates [56]. MP excitation has been widely investigated for 1D and 2D gratings, disk arrays, cross bars, and ring array structures [57]–[59]. An inductor–capacitor (LC) circuit model is used to analytically predict the fundamental MP resonance mode in deep grating with slight modifications for verification of underlying physical mechanisms by comparing with numerical simulation. Furthermore, the incidence angle dependence on the transmission spectra and EM fields for elucidating the resonant transmission behavior of the nanopillar-based filter is investigated. By pairing the designed filter with a black emitter at 1000°C or

higher, the I-V curve from the GaSb TPV cell and the heat-to-power TPV efficiency was theoretically calculated. Lastly TPV performance of a selective cell concept with nanopillar arrays directly on GaSb semiconductor is determined.

2.1 State-of-the-art Selective Filters

Selective filters improve TPV systems through spectral control of incident radiant energy. A lot of research is being done on the selective optical filter front that uses various phenomenon like the interference effect, surface polariton resonance (SP) modes, etc. to achieve superior spectral performance of TPV systems. Rahmlow et al. demonstrated a 70 % spectrally efficient tandem filter coupled with 0.6 eV InGaAs cell that had high transmission below the bandgap due to highly doped epitaxially grown layer of InPAs layer [60]. One dimensional (1D) 8-layer SiO_2/Si nanostructure TPV selective filter showed a 95% transmission at a wavelength of 1.73 μm and reflected most of the radiated photons in the wavelength range from 1.73 to 3.9 μm [61]. A ten-layer quarter wave photonic crystal was designed and fabricated with 40% spectral efficiency for 1500 K blackbody emitter [4]. A recent study suggested the use 1D photonic crystal with a passband range of 991 nm to 1788 nm as a filter for GaSb cell with a bandgap of 0.7 eV [21]. Most filters proposed transmit majority of the radiation spectrum above the bandgap. With all the advances in developing optical filters for TPV system, we propose a narrow band filter that has high transmission near the bandgap of the cell to prevent photons with lesser and excess energy from heating up the cell. The designed filter used MP physics to obtain the enhanced narrow band transmission with feasibility to fabricate at low-cost. Moreover, an optimized MP resonant wavelength can be obtained by tuning the geometry of the nanopillar array.

2.2 Selective Metasurface Filter Design and Simulation

The designed spectrally selective metasurface filter is made up of a vertically aligned aluminum nanopillar array coated on a quartz substrate, will be placed in between the emitter and the cell as shown in Figure 6 (a). The nanopillar array period, diameter, and height are represented by the geometric parameters *a*, *d*, and *h*, respectively. The electric field and magnetic field directions of a transverse magnetic (TM or *p*-polarized) wave at normal incidence are also depicted in the image by $\bar{E}$ and $\bar{H}$, respectively. Due to the geometric symmetry of nanowires, the radiative parameters of the spectrally selective filter, such as spectral transmittance under different polarized waves, will be the same for normal incidence.

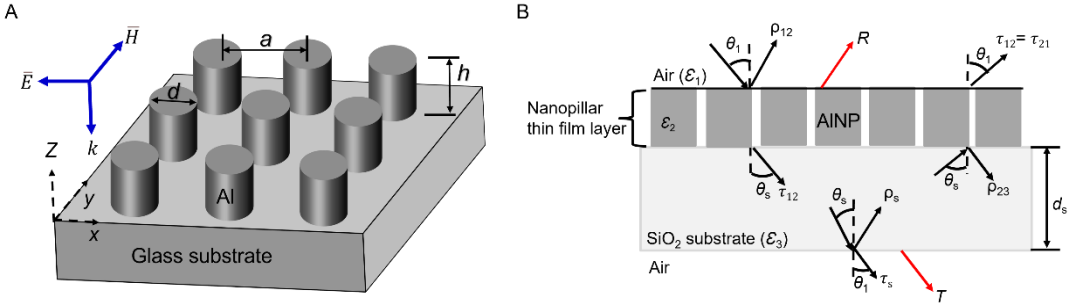

Figure 1: (a) Schematic of the proposed aluminum nanopillar metasurface filter on quartz substrate showing wave propagation at normal incidence. (b) Two-dimensional schematic of the proposed AlNP metasurface filter structure on a thick quartz substrate with thickness of d_s and the wave propagation at oblique angles of incidence.

The finite difference time domain (FDTD) technique (Lumerical Solutions, Inc., Canada) was used to acquire the radiative characteristics of the intended selective optical filter over a wavelength range of 0.4 μm to 4 μm using 300 data points with mesh size of 5 nm. By comparing the findings to those obtained from smaller mesh size of 3 nm, good numerical convergence is established as seen from Figure 35. Wavelength dependent

material properties were obtained from Palik data for aluminum and quartz [31]. A plane-wave source with a 0^o polarization angle (TM wave, as shown in Figure 1 (a)) is placed on the left side (-*x* direction) of the filter. Periodic boundary conditions were specified on both the *y* and *z* axes to account for phase changes between each period for modeling periodic structures, and completely matched layers were set on the *x* direction to eliminate wave reflections from simulation domain borders. Since the quartz substrate is non absorbing, ray tracing optics [32] was used to calculate the reflectance and transmittance of the filter structure and the wave propagation shown in Figure 1 (b) in order to consider the entire thickness of the substrate.

Radiative properties of thin coatings on a substrate are done for a variety of reasons: to eliminate transmission of ultraviolet radiation, to increase or decrease transmission over certain spectral regions. The substrate is usually thick enough to be considered incoherent while being semi-transparent for energy transfer consideration.

The refraction angle θ_s in the substrate can be calculated from the incidence angle θ_i by neglecting the absorption of the substrate. Figure 1 (b), ρ_{12} or ρ_{23} refers to the reflectance of the nanopillar film structure for rays originated from air or the substrate, τ_{12} and τ_{21} are the corresponding transmittance. ρ_{12}, ρ_{23}, τ_{12} and τ_{21} were numerically obtained from FDTD. ρ_s and τ_s represent the reflectance and transmittance for rays originated from the substrate and can be calculated using the Fresnel coefficients. The internal transmittance of the substrate is:

$$\tau = \exp\left(\frac{-4\pi k_s d_s}{\lambda \cos \theta_s}\right) \qquad 2.1$$

where k_s is absorption coefficient of the substrate for the wavelength and d_s is the thickness of the substrate. The reflectance and transmittance of the multilayer structure can be calculated as:

$$R = \rho_{12} + \frac{\rho_S \tau^2 \tau_{12} \tau_{21}}{1 - \rho_S \, \rho_{21} \tau_{12} \tau_{21}} \tag{2.2}$$

$$T = \frac{\tau_{12} \tau_s \tau}{1 - \rho_S \, \rho_{21} \tau_{12} \tau_{21}} \tag{2.3}$$

FDTD result shown in Figure 2 is compared to that of high frequency structure simulator (HFSS) (APPENDIX A Figure 30) to check the simulations validity, as FDTD is a full-wave simulation that numerically solves the Maxwell equations in every mesh element. The geometric characteristics of the selective optical filter are d = 370 nm, a = 450 nm, and h = 700 nm, which are utilized as base values to trigger resonances at the bandgap of the GaSb cell. These geometric parameters were determined based on the feasibility of manufacturing [62]–[64] and their ability to enhance the transmission peak. As demonstrated in Figure 30 in the appendix section, the magnitude of the spectral reflectance, absorptance and transmittance acquired by FDTD and HFSS show reasonable agreement.

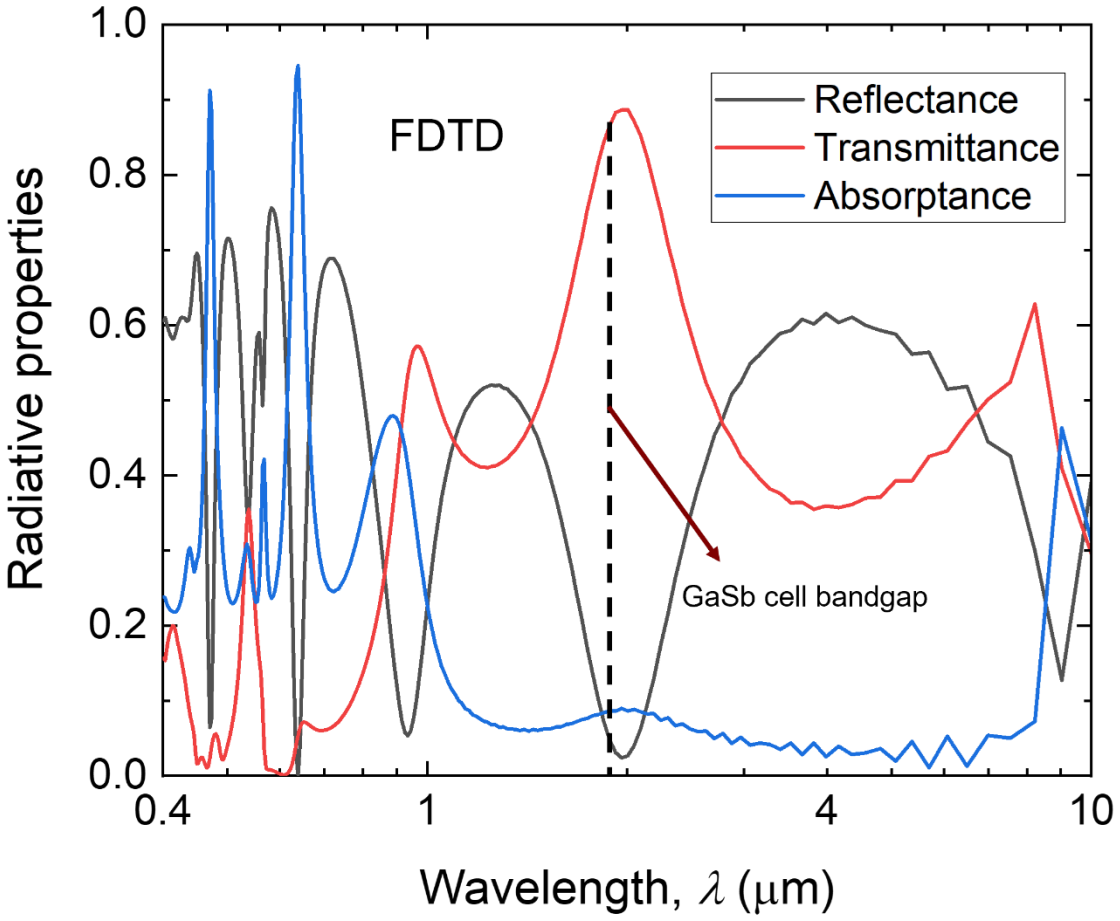

Figure 2: The spectral reflectance, transmittance, and absorptance of the selective metasurface filter at normal incidence for TM polarized light based on FDTD simulations with nanopillar diameter, d = 370 nm with period, a = 450 nm and heigh, h = 700 nm

2.3 Elucidation of Magnetic Polariton Effect

To explain the resonance effect indicated by the spectral transmission peak, the electromagnetic field distributions at resonance wavelengths: (a) 1.9 μm, (b) 0.93 μm, and (c) 0.54 μm are estimated using FDTD as shown in Figure 3. The electric field vectors are represented by arrows, and the magnetic field normalized to the incident field as seen from

the contour plots. The confinement of the magnetic energy between the nanopillars can be clearly seen from Figure 3 (b). The electric field vectors pointing in the opposite directions indicate that the electric field forms a closed loop surrounding the confining region (the circles between the pillars). Grating based metamaterials have shown similar behavior that has been proven to be the resonance of MP [41]. When incoming electromagnetic fields excite MP, an oscillating resonant electrical current is formed inside the nanopillar formations, which is caused by free charges at the surface. With severely restricted electromagnetic energy in the air gap, the resonant electrical current loop oscillates between nearby nanopillars, resulting in an increase in spectral transmittance at resonance wavelengths. As shown in Figure 3 (b)-(d), higher harmonic modes of MP (i.e., MP2 and MP3) contribute to the selective transmittance at shorter resonance wavelengths in the visible range. The harmonic modes play a significant role in the case of filters as they achieve high transmissions at wavelengths lower than the bandgap. An analytical inductor–capacitor (LC) model based on surface charge distribution at MP resonant wavelength has been successfully applied to forecast the resonance condition for grating-based metamaterials, as established in prior works [28], [42], [43].

The major challenge is quantifying the inductance and capacitance of a nanowire. Given that the LC circuit model is a basic estimation approach, integrating the parameters over the circular nanowire surfaces would result in complex expressions, which would defeat the purpose of the model. To get over this difficulty, a modified LC model has been proposed by simplifying nanowires to an effective plate, based on the similar strongly localized magnetic field distributions based on the literature [65]. The equivalent LC circuit model is used to predict the resonance for the fundamental mode. As shown in Figure 3

(a), C_g and C_{sub} forms a capacitor in the air gap and substrate respectively between the nanopillars, $L_{m,NP}$ is the mutual inductance between nanowires, and $L_{k,NP}$ is the kinetic inductance contributed by the drifting electrons in nanowires. Therefore, the total impedance of the LC circuit can be expressed as:

$$Z_{total} = i[\omega(2\mathrm{L_{m,NP}} + \mathrm{L}_{k,\mathrm{NP}}) - \frac{1}{\omega c_g} - \frac{1}{\omega c_{sub}}] \quad 2.4$$

When the overall impedance Z_{total} is zero, MP resonance occurs. As a result, Equation (2.5) may be used to calculate the MP resonance wavelength λ_0, where c_0 is the speed of light.

$$\lambda_0 = \sqrt{\frac{2c_g c_{sub}(\mathrm{L_{m,NP}} + \mathrm{L}_{k,\mathrm{NP}})}{c_g + c_{sub}}} \quad 2.5$$

where

$$L_{m,NP} = 0.5\mu_0 hb \quad 2.6$$

$$L_{k,NP} = \frac{b}{\varepsilon_0\, \delta_{\mathrm{NP}} \omega^2 \varepsilon'_{NP}} \quad 2.7$$

$$c_{sub} = \mathrm{c_2}\varepsilon_0 \varepsilon_{\mathrm{sub}} \frac{h}{b} \quad 2.8$$

$$c_g = c_1 \varepsilon_0 \frac{h}{b} \quad 2.9$$

where μ_0 is the magnetic permeability of free space, $\mathcal{E}_0$ is the permittivity of free space, $\mathcal{E}_{sub}$ is the dielectric function (real part) of SiO_2, h is the height of the nanopillar, and b is the difference between the interpore distance (a) and diameter of the nanopillars (d). The non-uniform charge distribution factor c_1 and c_2 of 0.2 to 0.3 is typical [66]. In this computation, to accommodate for curved surface of the nanowire the nonuniform charge distribution factor c_1 is set as 0.4 based on prior literature [65] and c_2 to be 0.1 due to negligible effect of the non-absorbing quartz substrate.

As a result, the LC circuit model predicts a resonance wavelength of 1.9 μm for MP1 on the base geometry, same as the value found via FDTD simulation, showing that the resonance is attributable to magnetic resonance excitation. The distribution of the electromagnetic fields at the *X*-*Z* cross section at λ= 1.9 μm was presented in Figure 3 (b) to assist elucidate the underlying causes for the absorption peaks. Figure 3 (b) reveals the electromagnetic field distribution in *X*–*Y* plane located at 0.3 μm above the bottom of the nanowires (i.e., at the middle of the nanowires) when MP1 resonance is excited (1.9 μm).

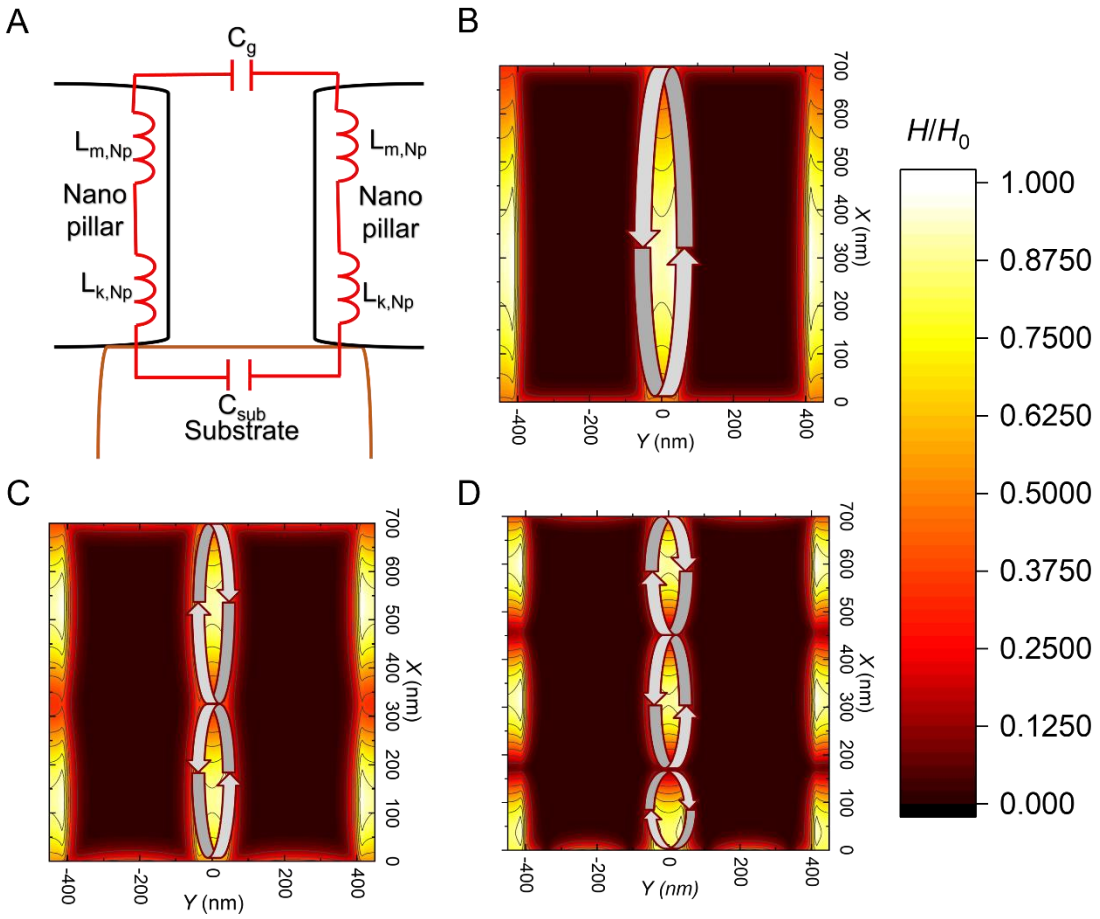

Figure 3: (a) The LC circuit model based on charge and field distribution and the electromagnetic field distribution contour plots on the *X*–*Y* plane when MP resonances are excited at wavelengths (b) 1.9, (c) 0.93 μm, and (d) 0.54 μm.

As a consequence, the resonance wavelength of MP1 on the base geometry predicted by the LC circuit model is 1.88 μm, compared to 1.9 μm derived via FDTD simulation with a ~5% relative error, demonstrating that the resonance is caused by magnetic resonance excitation.

2.4 Geometric dependence of MP resonance

The aim of this study is to achieve selective spectral transmittivity for improving GaSb TPV cell. In other words, near-unity transmittivity above the bandgap, especially near the bandgap of the cell and high reflectivity at all wavelengths corresponding to below the bandgap. The tunability given by geometric parameters, as seen in Figure 4, is one of the most advantageous properties of MP resonance. The impact of geometric parameters on MP resonance were investigated. The spectral normal transmittance of the film-coupled metamaterial structure was determined by altering the nanowire diameter (*d*), period (*a*), and height (*h*) separately while keeping all other geometric parameters constant. With both *d* and *a* fixed at 370 and 450 nm, respectively, Figure 4 (a) demonstrates the influence of nanowire height varying from 200 to 800 nm on spectral absorptance. Although the red shifting of resonance peaks is visible, but the tunability of *h* on spectral absorptance enhancement is not that obvious. The Figure 4 (b) depicts the structure's spectral absorptance as the nanowire diameter changes from 200 nm to 400 nm. When the diameter is increased, the absorption peak caused by MP excitation moves to longer wavelengths, which is consistent with prior observations [65]. Figure 4(c) illustrates the spectral absorptance with different array periods and the simulation result shows that the resonance

peaks blue shift to shorter wavelengths the array period (*a*) is increased. Meanwhile, the amplitude of the enhancement peaks at shorter wavelengths also increased to higher values. The resonance wavelengths of MP obtained by FDTD simulation with varied geometric parameters are also compared with those predicted by the LC circuit model. Figure 4(e) depicts a comparison of the MP resonance wavelength as a function of nanowire diameter between the FDTD simulations and the LC circuit model prediction. The MP resonance wavelength increases monotonically with nanowire diameter, as anticipated by the LC circuit model, due to increase in capacitance and inductance values according to Eqs. (2.6–2.9). The FDTD findings accord well with the LC circuit model, which verifies the simulation's reliability. Similar patterns are seen for the impacts of nanowire height and

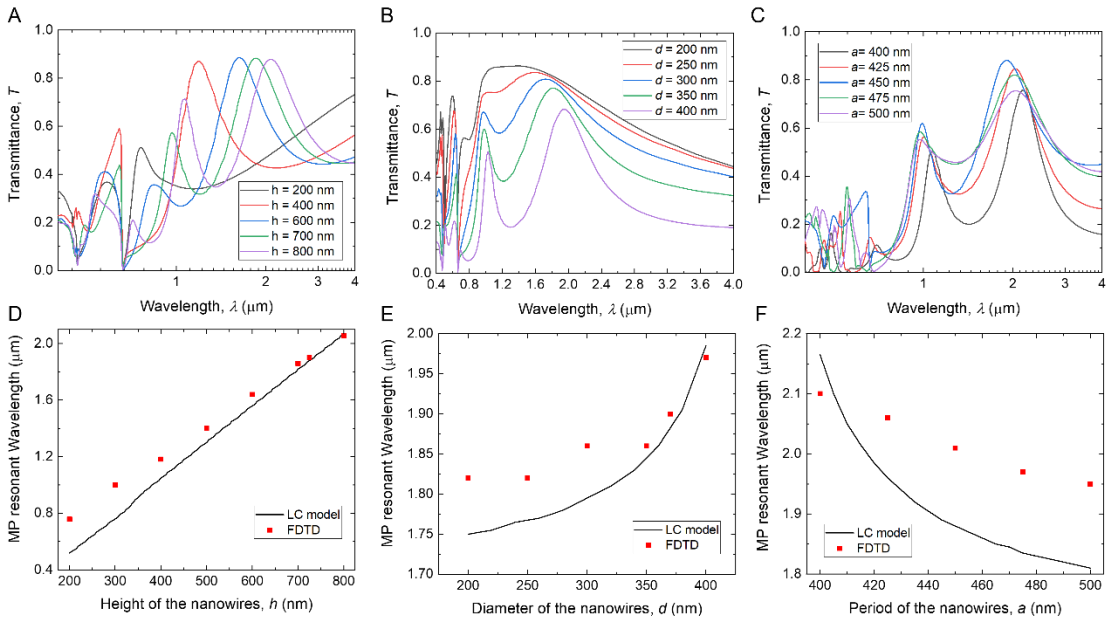

Figure 4: The spectral transmittance with respect to different nanopillars: (a) diameter, (b) height and (c) period simulated by FDTD. The MP1 wavelengths predicted by FDTD, and LC circuit model with respect to different nanopillars: (d) diameter, (e) height and (f) period with fixed base values of d = 370, a = 450 nm, and h = 700 nm

period, as illustrated in Figure 4(d) and Figure 4(f), which can further validate the correctness and reasonableness of the LC circuit model proposed in this work.

2.5 Effects of Incidence Angle and Polarization

Figure 5 shows the spectral-directional transmittance of the nanopillar metasurface TPV filter as a function of wavelength for TM (Figure 5 (a)) and TE (Figure 5 (b)) incident waves to understand the behaviors of MP at oblique incidences. The transmittance is plotted as a function of wavelength ranging from 0.3 to 2.1 μm which spreads over all the three MP resonance peaks. All the 3 MP peaks are important for the enhanced transmittance as they fall below the bandgap wavelength and hence can lead to enhanced TPV efficiency. As demonstrated in Figure 5, these three resonance peaks are independent for incidence angles up to ±60 degrees for TE and TM waves. That is, spectral transmittance can still be about 0.8 at ±60 degrees for both polarizations at the bandgap wavelength. This shows that the MP resonance is independent of angle of incidence as seen in prior literature [65]. We have used the hemispherical transmittance of the filter for our calculations as the incident light from all angles of incidence should be considered when calculating the effective absorptance of the cell.

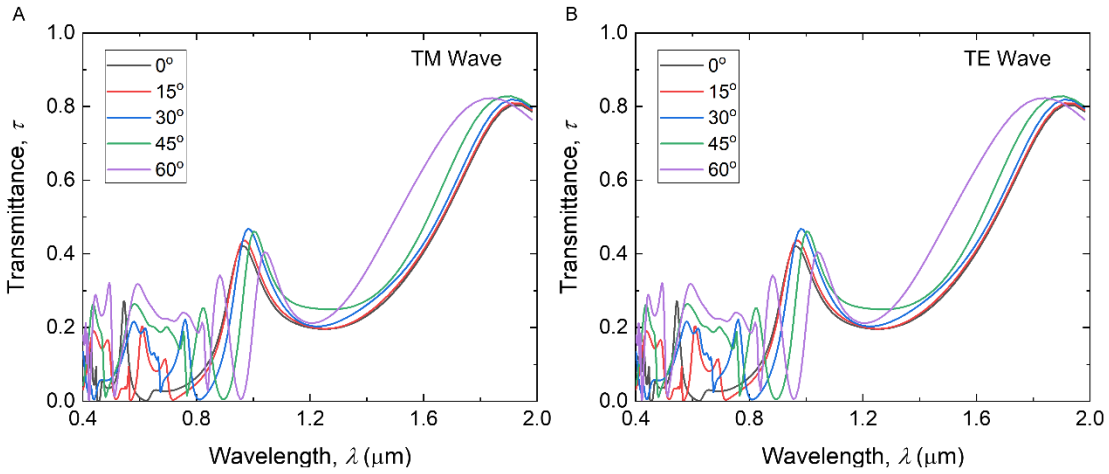

Figure 5: Theoretical spectral Transmittance of the proposed AlNP metasurface filter at different incident angles for (a) TM wave and (b) TE wave.

2.6 Theoretical analysis of Thermophotovoltaic system performance

The TPV system considered in this study consists of a black emitter, spectrally selective optical filter and a cell as shown in Figure 6 (a). GaSb cell has spectral absorptance as shown in Figure 6 (b), the cell has high absorptance near the bandgap of the cell. Figure 6 (c) shows the reference radiative property of an emitter i.e., the emittance of the black emitter. A black emitter has unity emittance at all wavelengths. In this regard, the use of an optical filter becomes vital to improve the TPV system efficiency. An ideal optical broadband filter transmits all the radiation above the bandgap of the ideal cell and reflects all the radiation below where the ideal narrowband filter transmits unity in the spectral range of λ_1 to λ_2 as shown in Figure 6 (d). The long cutoff wavelength λ_2 is fixed at 1.9 μm corresponding to the GaSb cell bandgap whereas the variable value of short cutoff wavelength λ_1 impact the TPV system efficiency.

In this study, the TPV system comprises of a black emitter, a filter that selectively transmits photons with energy suited to the bandgap of the cell receiving them. Short-circuit current density, open-circuit voltage, output electric power, and cell efficiency were determined to objectively assess the performance of the filter coupled TPV system. The total thermal-to-electricity energy conversion efficiency for a TPV system is defined as the

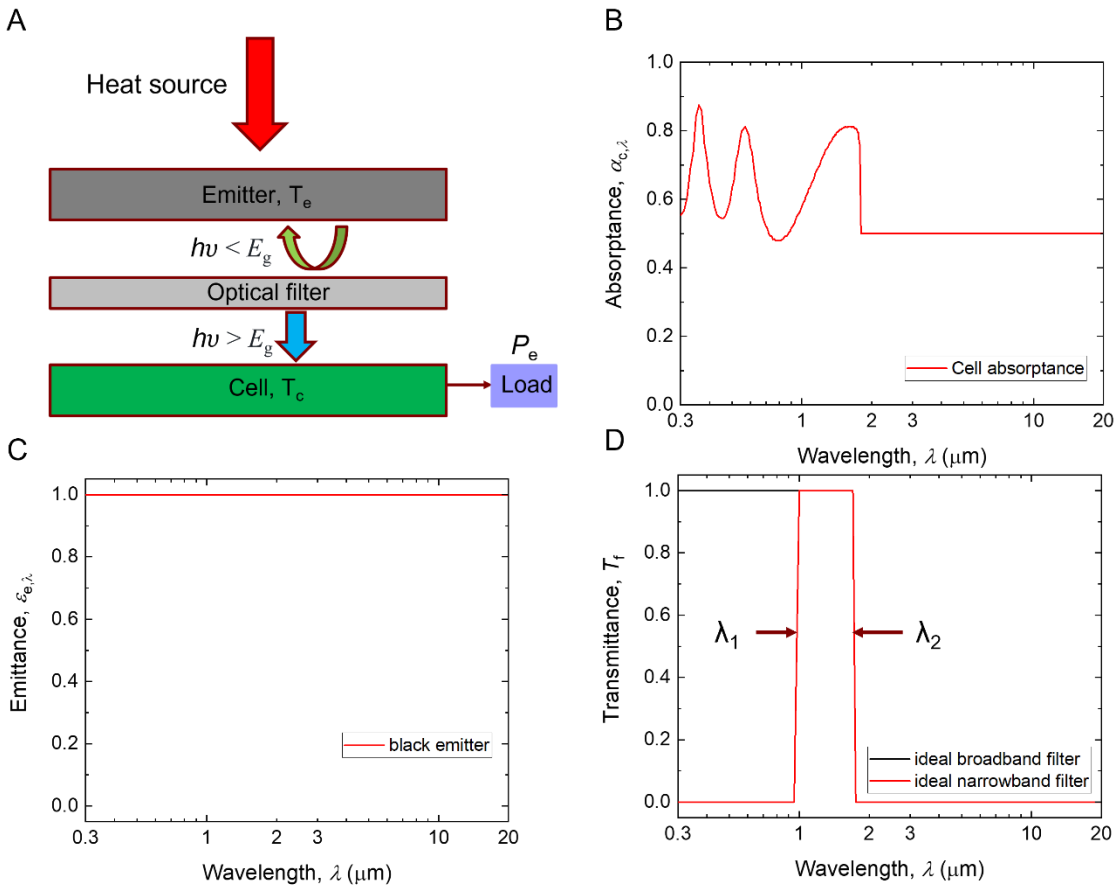

Figure 6: (a) Schematic of a simple TPV system consisting of an emitter, optical filter, and a cell, (b) spectral absorptance of the GaSb cell, (c) spectral emittance of a black emitter, and (d) spectral transmittance of an ideal broadband and narrowband optical filter to transmit the light with energy above the band gap of the cell.

ratio of the output electric power (P_e) to the total radiative heat flux incident (q_{in}) on the TPV cell.

$$\eta_{TPV} = \frac{P_e}{Q_{in}} \tag{2.10}$$

In Eq. (2.10), the generated maximum power density P_e (W/cm^2) is calculated by [67]:

$$P_e = \mathrm{V_{OC}}\, I_{SC} \left(1 - \frac{1}{X}\right)\left(1 - \frac{\ln X}{X}\right) \tag{2.11}$$

where $X = \ln\left(\frac{I_{Sc}}{I_0}\right)$. The above equation considers the current–voltage diode characteristics. Due to charge accumulation at the TPV cell's two electrodes, an open-circuit voltage develops between the cell's terminals, which is represented as [68]:

$$V_{\mathrm{OC}} = \left(\frac{k_B\, \mathrm{T_c}}{e}\right) \ln\left(\frac{\mathrm{I_{sc}}}{I_0 + 1}\right) \tag{2.12}$$

where k_B is the Boltzmann constant, T_c is the cell temperature, which is assumed to be 300 K, and I_0 is the dark current which can be calculated by [27]:

$$I_0 = \mathrm{e}\left(\frac{n_i^2\, D_{\mathrm{h}}}{L_h\, \mathrm{N_D}} + \frac{n_i^2\, D_{\mathrm{e}}}{L_e\, \mathrm{N_A}}\right) \tag{2.13}$$

where n_i is the intrinsic carrier concentration of GaSb, N_D and N_A are respectively the donor concentration and acceptor concentration, D_h and D_e are respectively the hole diffusion coefficient and electron diffusion coefficient, and L_h and L_e are respectively the hole and electron diffusion length [69].The values used for n_i, N_D, N_A, D_h, D_e, L_h and L_e are provided in the supplementary section.

The short-circuit current density I_{SC} (A/cm^2) is calculated by:

$$I_{SC} = \int_0^{\frac{hc_0}{E_g}} \frac{e\lambda}{hc_0} \tau_{filter}\, \alpha\,(\lambda)\eta_i(\lambda) q_{e-c}(\lambda) d\lambda \qquad 2.14$$

where h is Planck's constant, c_0 is the speed of light in vacuum, e is the elementary electric charge, E_g is the bandgap of the GaSb cell (0.72 eV), $\alpha(\lambda)$ is the normalized energy absorption in the GaSb layer only, $\eta_i(\lambda)$ is the internal quantum efficiency (IQE) of the GaSb TPV cell form Tang et al. [70]. Bulk and surface non-radiative recombination losses lead to reduction of IQE [69]. Under the assumption that $\eta_i(\lambda)$ is 100%, all absorbed photons with energies greater than the energy bandgap contribute to photocurrent production [68]. This can be achieved by eliminating the surface recombination losses by passivating the cell [69], introducing morphological structural effects and optimizing the emitter and base layer thicknesses to improve spectral selectivity and reduce bulk non-radiative recombination losses [69]. Finally, $q_{e-c}(\lambda)$ is the spectral net radiative heat transfer between the emitter and the cell, and the total incident radiative heat flux q_{in} on the TPV cell is

$$q_{in} = \int_0^{\infty} q_{e-c}(\lambda)\, d\lambda = \int_0^{\infty} \frac{\mathrm{E_{b\lambda,e}(T_e)} - \mathrm{E_{b\lambda,c}}(T_c)}{\frac{1}{\varepsilon_{\lambda,e}} + \frac{1}{\varepsilon_{\lambda,c}} - 1} \qquad 2.15$$

where subscripts e and c represent emitter and cell, respectively. $\varepsilon_{\lambda,e} = 1$ and $\varepsilon_{\lambda,c} = \tau_{filter}\, \alpha_{cell}$ are the spectral emittance of the emitter and the cell, both of which are assumed diffuse. The emissivity formula for the cell is valid assuming that the optical filter absorbs negligible incoming radiation energy. The view factor between the emitter and the cell is assumed to be one here for simplicity and the emitter area and cell area are assumed to be equal.

$$q_{in} = \int_0^\infty q_{e-c}(\lambda)\, d\lambda = \int_0^\infty \tau_{filter}\, \alpha_{cell}[\mathrm{E_{b\lambda,e}(T_e)} - \mathrm{E_{b\lambda,c}}(T_c)] \qquad 2.16$$

The emitter temperature T_e is varied from 1000 to 2000 K, the filter temperature is assumed to be 300 K and cell temperature, T_c = 300 K. The blackbody emissive power $E_{b\lambda}(T)$ can be calculated by [71]:

$$E_{b\lambda}(T) = \frac{2\pi h c_0^2}{\lambda^5[e^{\frac{hc_0}{\lambda k_B T}} - 1]} \qquad 2.17$$

In order to evaluate the performance of the proposed filter as a part of the TPV system, the spectral and the TPV system overall efficiency were quantitively calculated. Figure 7 (a) shows the spectral efficiency of the theoretical metamaterial based selective filter coupled with black emitter at different temperatures. For comparison, the spectral efficiencies with and without ideal narrowband and broadband filter coupled with black emitter ($\varepsilon_{e,\lambda}$ = 1) are also shown. The spectral efficiency improves with emitter temperature because the thermal radiation spectrum moves to a lower wavelength as temperature rises, increasing the fraction of photons with energies over the PV cell's bandgap. The proposed filter coupled with the black emitter improves the spectral efficiency to 65% at 2000 K from 49% for the standalone emitter.

Figure 7 (b)–(d) show the predicted TPV efficiency, net radiative heat flow between the emitter and the PV cell, and output power for the TPV system using AlNP selective filter combined with a GaSb cell, respectively. It should be noted that the in-band spectral absorptance and the of the GaSb cell is acquired from Ref [70], and the out-of-band absorptance is assumed to be 0.5 as a nominal value based on absorptance of typical GaSb cells from JX crystals [72]–[74]. The calculations using other nominal values of 0.05, 0.2,

0.75 and 0.95 for out-of-band absorptance were done for reference and the results of the system efficiency, spectral efficiency, net radiative flux, and output power are shown in Figure 34 (APPENDIX A). The results using ideal narrowband and broadband filter coupled with black emitter and standalone black emitter are shown for comparison. The TPV system efficiency ranges from 1.5% to 18% with stand-alone black emitter at temperature range from 1000 to 2000 K. While with the modeled AlNP filter, the TPV efficiency improves ranging from 3.8 to 24.1% because of spectral selectivity of the designed filter with lower transmission below the bandgap. With a cell having 100% IQE and the designed filter, the TPV efficiency can be further improved ranging from 5.4% to 31.1% due to improved spectral efficiency. Note that these three filters paired with black emitter produce similar P_e below 1200 K. The standalone black emitter will outperform the suggested filter pairing as the emitter temperature rises. P_e is determined by the net radiative heat flux over the cell's bandgap. The emissive power of the emitter is low at shorter wavelengths (above the bandgap) at low temperatures which causes the similar power. It is observed that as T_e increases, so does the output electric power and cell efficiency. The output electric power drops while the cell efficiency rises as the transmittance bandwidth decreases (i.e., λ_1). To achieve high efficiency, a selective filter with a narrow transmittance band and an elevated temperature of the emitter are required. The maximum TPV efficiency can be obtained using the proposed metasurface filter as η_{TPV} = 24.1% with output power P_e = 3.67 W/cm^2 at T_e = 2000K.

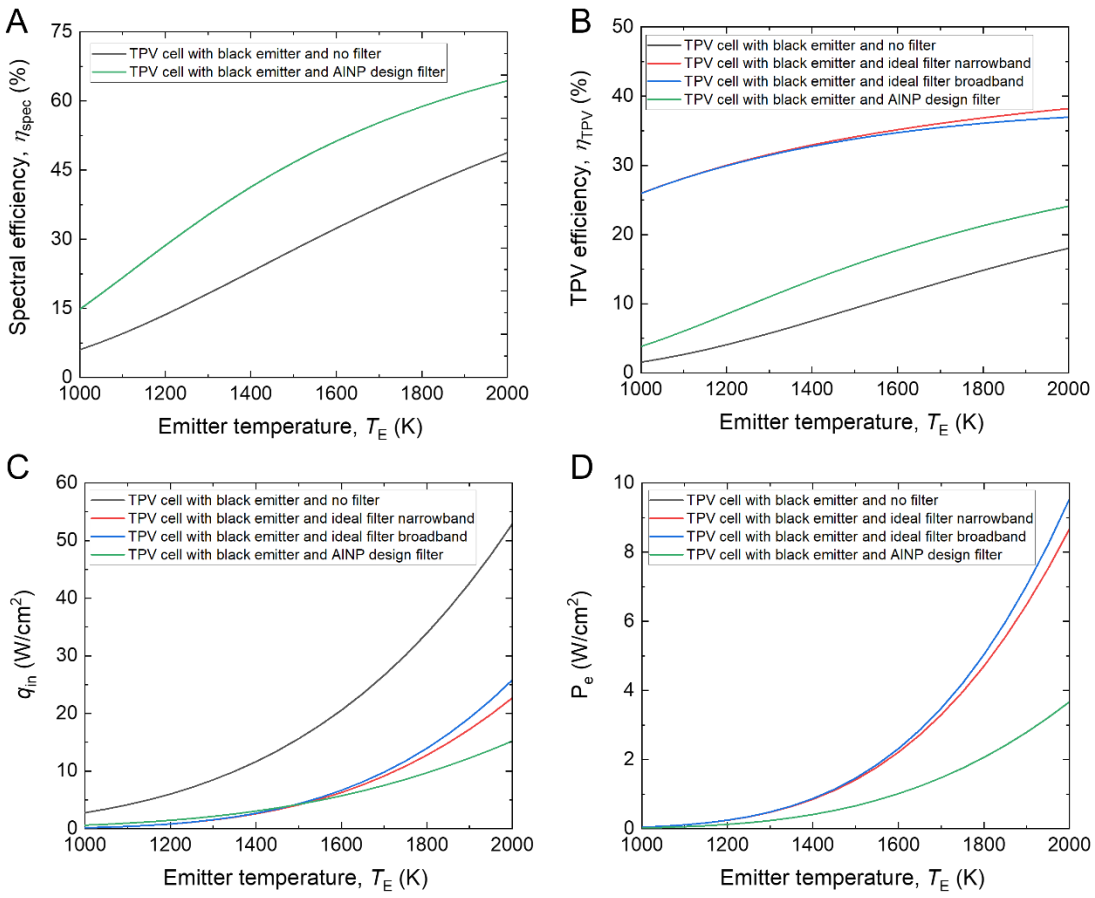

Figure 7: (a) Spectral efficiency, (b) TPV efficiency, (c) net radiative heat flux and (d) output power at different temperatures from 1000 K to 2000 K with theoretical AlNP metasurface filter, and black emitter paired with a GaSb cell.

CHAPTER 3

NANOPOROUS GOLD THIN FILMS

In this work, NPG thin films with varying pore diameters and PVF were fabricated by timed chemical dealloying of an Au-Ag thin film alloy. By synthesizing NPG thin films at short dealloying time scales and low temperatures, the residual silver content is significantly reduced (i.e., down to 1-12 vol.%) and can be measured with Energy dispersive X-ray spectroscopy (EDS) to estimate the PVF through a simple formula that neglects shrinkage effects during dealloying. PVF varying from 45% to 60% were estimated using combined Scanning electron microscopy (SEM) and EDS data and average ligament size ranged between 30 nm and 80 nm. The reflectance of these samples was measured at room temperature using an integrating sphere (IS) for varying angles of incidence at different polarizations and compared with results obtained from Bruggeman (BR) effective medium theory. Finally, the optical response of the NPG remained unaltered up to 100 °C indicating its excellent thermal stability.

3.1 Introduction

At the center of exploiting the morphology of NPG in the aforementioned applications is its ability to be controlled through advanced synthesis methods, including dealloying with selective dissolution from colloidal precursor mixtures [36], anodization [37], electrochemical deposition onto sacrificial scaffolds [38], hydrogen bubble dynamic template synthesis [39], ultra-thin porous sputtered layers [40], spray deposition of gold nanoparticles [25], [41], [42] and evaporation-induced self-assembly of colloidal crystals [37]. In the process of dealloying, the pore diameter and the PVF can be modified by

controlling the dealloying conditions such as temperature, time and the relative contents of the alloy elements [26], [31], [35], [43]–[45].

To relate the theoretical and experimental optical data, it is critical to measure or estimate the PVF and pore sizes in dealloyed nanoporous thin films. While existing SEM image analysis software [75] outputs ligament size and pore area fraction, the latter quantity is not easily translated into a PVF value. During timed dealloying, the estimated PVF progressively increases with dealloying time, and it is used to qualitatively predict the changes in optical reflectance data at varying wavelengths and incidence angles. The ability to red shift the effective refractive index of the NPG with increasing PVF and, hence, to broaden the absorption spectrum, along with its thermal stability, makes NPG a viable candidate for solar thermal energy harvesting.

3.2 Sample fabrication and SEM characterization

P-type boron doped silicon wafer (100) was cut into 2×2 cm^2 chips and adhered on the outer circumference of a 100-mm carrier wafer to reduce variation in thickness and composition during magnetron sputtering. The loaded carrier wafer was placed into the magnetron sputtering chamber (NanoMaster NSC-3000). Metal targets of Cr, Ag and Au (2 inch in size) were magnetically attached onto MeiVac deposition sources which are placed at 8-1/8 inches from the substrate. The system was pumped down to a base pressure of 1.0×10^{-7} Torr before sputtering. Si chips were sputtered with three layers in the following order: (i) 20 nm of Cr as an adhesion layer, (ii) 50 nm of Au, and (iii) 700 nm of Au-Ag alloy by co-sputtering. The system was calibrated with a crystal monitor prior to deposition. During every sputtering operation, the deposition pressure was set to 1 mTorr

and the Ar flow rate set to 4.5 sccm. During co-sputtering of the Ag-Au layer, the powers on Au and Ag targets were set to 58 W (DC) and 150 W (RF), respectively, and its corresponding sputtering rates measures to be 1 Å/s and 1.5 Å/s, which gave an alloy with 60 vol.% of Ag. All sputtering was performed with constant rotation and the carrier wafer placed horizontally. A total of 8 samples were produced. Sputtered samples were dealloyed in 7.85 M HNO_3 at conditions summarized in first three columns of Table 1. After dealloying, samples were quenched and thoroughly washed in DI water and dried in air.

As shown in Figure 8, a scanning electron microscope (Phillips XL-30) was employed to analyze morphology, ligament, and pore sizes as well as layer thickness after dealloying for all 8 samples with top-view and cross-sectional images. The cross-sectional SEM image Au-Ag alloy precursor sample before dealloying of the precursor had a measured thickness of 731 nm. Clearly the nanopores are quite uniform within the whole layer, and there is no multilayer formed as those seen in Ref. [76]. The ligaments are randomly oriented without preferable directions different from the columnar dealloying patterns observed by others [77], indicating optically isotropic nanoporous structures from the NPG samples in this study.

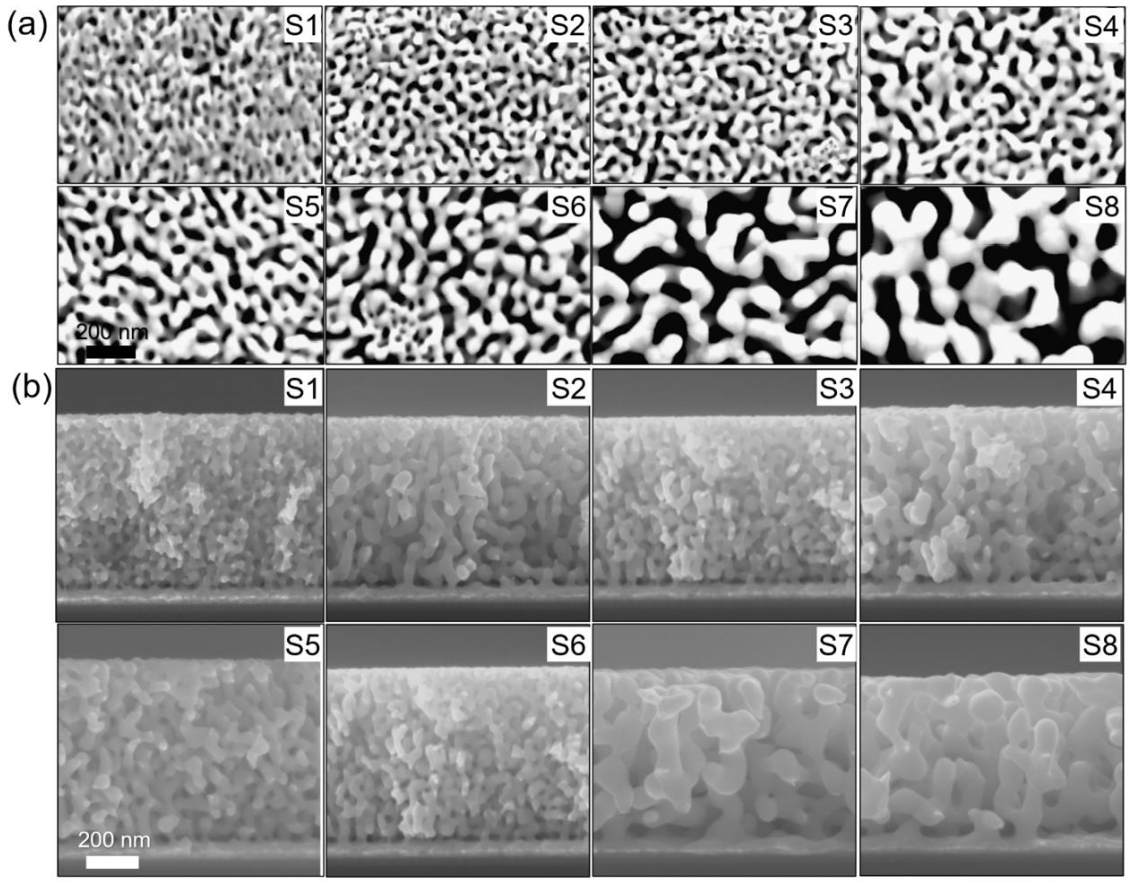

Figure 8: (a) Top-view and (b) cross-sectional SEM images of fabricated nanoporous gold thin-film samples with varying pore diameters and apparent pore volume factions (*f*) as listed in Table 1: Sample 1 (S1, $f = 45\%$), Sample 2 (S2, $f = 53\%$), Sample 3 (S3, $f = 56\%$), Sample 4 (S4, $f = 58\%$), Sample 5 (S5, $f = 59\%$), Sample 6 (S6, $f = 60\%$), Sample 7 (S7, $f = 60\%$), and Sample 8 (S8, $f = 60\%$). The scale bar is 200 nm for all the SEM images.

A Python-based AQUAMI software [75] automatically applies image threshold and calculates ligament and pore diameter, and pore area fraction of all NPG samples. The SEM images analysis with AQUAMI software outputs the average pore diameter, average ligament diameter, and average pore area fraction. One SEM image per sample was analyzed and an average was calculated. Figure 9 is constructed by relating the average ligament diameter, average pore diameter, average pore area fraction and residual silver

content with the dealloying time for different temperatures. EDS analysis is employed to quantify the low levels of residual silver content after dealloying as the computational modeling does not account for silver as shown in Figure 9 (a). During dealloying, silver residue remains in NPG structure and slowly decreased with longer dealloying time. Moreover, it can be seen that silver etching rate is higher for elevated temperatures, which can be evidenced by low silver content (< 2 vol.% for 70°C and 85°C). Also, there is coupling between ligament and pore diameter (Figure 9 (b) and (c)), and they scale with etching temperature and time similarly. This evidence is similar to that observed by other researchers [78]. From Figure 9 (d), there is an exponential empirical correlation between pore diameter and pore area fraction, indicating that these two variables cannot be independently controlled via the selected process conditions.

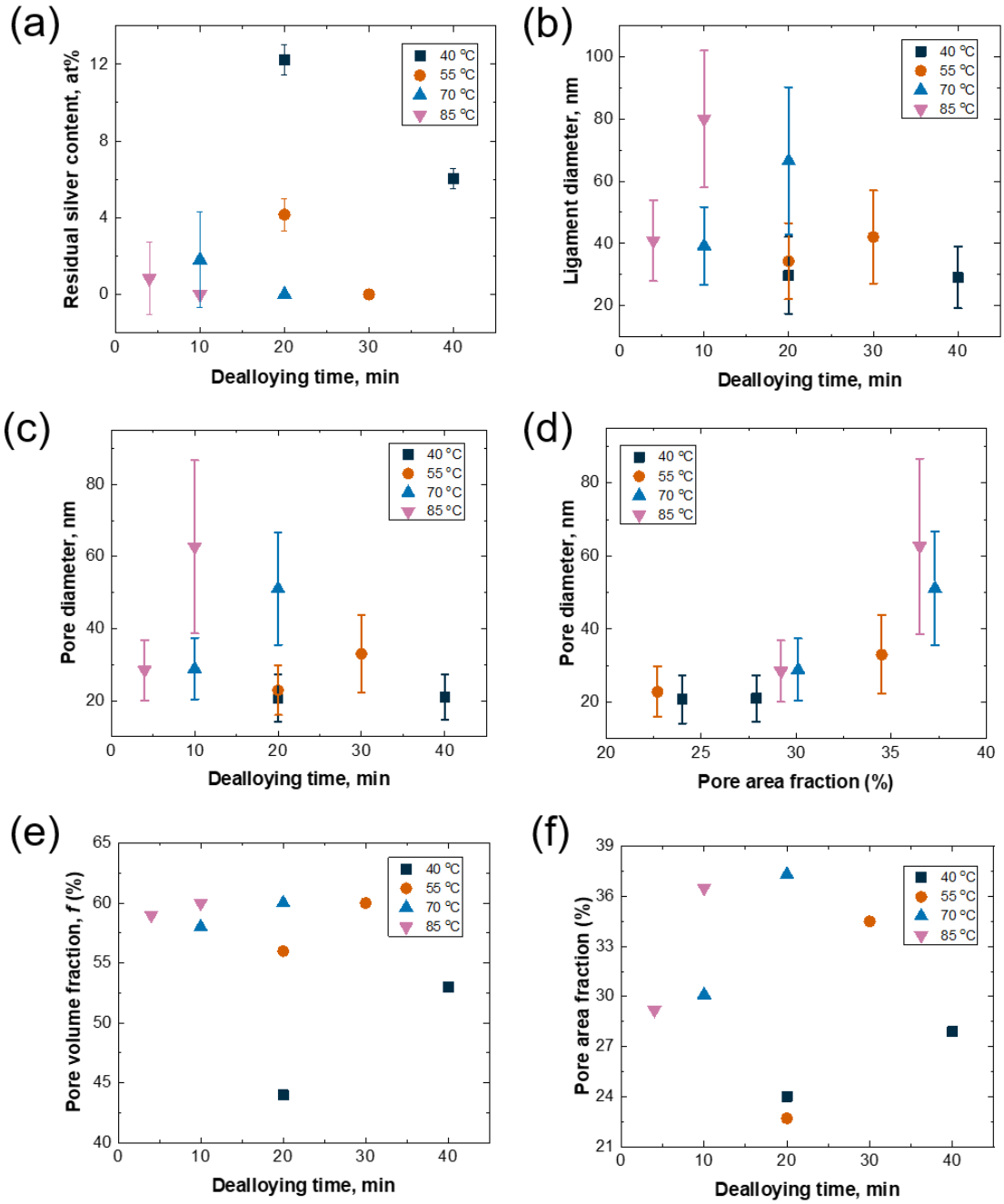

Figure 9: Correlations between the fabrication conditions and morphology for fabricated nanoporous gold samples: (a) the residual silver content dependence on the dealloying time; (b) average ligament diameter dependence on the dealloying time; (c) average pore diameter dependence on the dealloying time; (d) pore area fraction dependence on the pore diameter; (e) pore area fraction dependence on the dealloying time; and (f) pore volume fraction dependence on the dealloying time.

Besides, the residual silver content in the dealloyed sample was used to determine apparent PVF of the samples, this was calculated by subtracting the residual silver content after de-alloy from the initial amount of silver (60% by volume) in the Au-Ag alloy. By assuming that Au is not etched, and its volume does not shrink after dealloying, the apparent PVF (*f*) can be calculated from the residual silver content in the samples as:

$$f = \frac{V_{pores}}{V_{total}} = \frac{f_{v,Ag}^{i} - f_{v,Ag}^{f}}{1 - f_{v,Ag}^{f}} \quad 3.1$$

where V_{pores} is the volume of the air pores, V_{total} is total volume of the sample, $f_{v,Ag}^{i}$ is the initial volume fraction of the silver in the Ag-Au alloy, and $f_{v,Ag}^{f}$ is the residual silver by volume in the NPG film. Note that from the cross-sectional SEM images of the precursor Au-Ag alloy were obtained and NPG films in Figure 8, film thickness shrinkages from 9% to 17% can be estimated, which are much smaller than the 30% shrinkage observed in literature [79]. This would lead to about 5% decrease of the PVF due to the shrinkage, which is considered as part of uncertainty without correcting the apparent PVF values. The pore diameter, pore area fraction, residual silver content, and PVF for all 8 fabricated NPG samples are listed in Table 1.

Table 1. Dealloying temperature, dealloying time, pore diameter, pore area fraction, residual silver content, and PVF of the fabricated nanoporous gold samples.

Sample No.	Dealloying temperature (°C)	Dealloying time (min)	Pore diameter (nm)	Pore area fraction (%)	Residual silver content (%)	Apparent Pore volume fraction (%)
1	40	20	20	24	12.5	45
2	40	40	20	28	6.0	53
3	55	20	25	23	4.0	56
4	70	10	30	30	2.0	58
5	85	4	29	29	1.0	59
6	55	30	35	35	0.0	60
7	70	20	50	37	0.0	60
8	85	10	65	36	0.0	60

3.3 Experimental Method of Optical Characterization

The hemispherical reflectance $R_\lambda^\cap$ of the fabricated NPG samples was measured by an 8-inch PTFE integrating sphere (Labsphere Inc.) coupled with a tunable light source (TLS-250Q, Newport Inc.), a pre-amplifier (PDA200C, Thorlabs), and a lock-in amplifier (Merlin, Oriel Inc.) from 0.35 to 1.7 μm in wavelength with spectral resolution of 10 nm. As illustrated in Figure 10 (a), the Quartz-Tungsten-Halogen (QTH) lamp source emits broadband light from ultraviolet to near infrared range. After the light enters the monochromator through the entrance slit, it gets diffracted by the gratings. By rotating the

gratings with a high precision stepper motor at a particular angle, a quasi-monochromatic light at a desired wavelength is delivered through the exit slit. A synchronized chopper modulates the monochromatic light before entering the IS to eliminate ambient noise with the lock-in-amplifier. The directional-hemispherical reflectance was measured at each

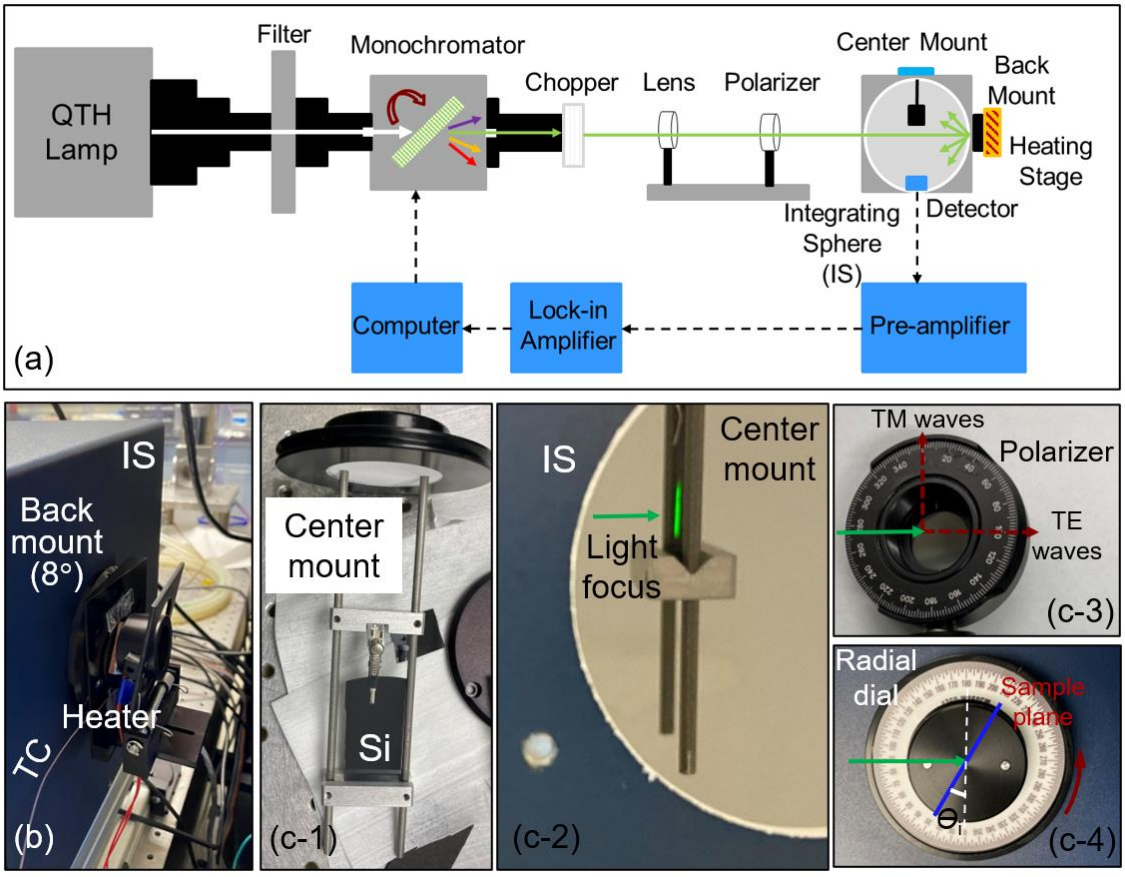

Figure 10: (a) Optical schematic to illustrate the working principle of the tunable light source and the integrating sphere (IS) for spectral-directional hemispherical reflectance measurement. (b) Photo of the 8° sample mount at the back side of the IS with a heater and a thermocouple for temperature-dependent measurement in air from room temperature up to 100°C. (c-1) Photo of the center mount for oblique incident angle measurement. (c-2) Photo of the monochromatic light focused on the sample mounted on the center stage. (c-3) Photo of the optical polarizer used for TE or TM polarization selection. (c-4) Photo of the radial dial on the center sample mount for selecting the incidence angle θ_i.

wavelength by taking a wavelength scan. The reflectance from 0.35 to 1 μm in wavelength was measured by an internal Si detector (SM05PD1A, Thorlabs), while an InGaAs detector (SM05PD5A, Thorlabs) was employed at longer wavelengths from 1 μm up to 1.7 μm. The pre-amplifier is used to amplify the detector signals before the lock-in amplification. An aluminum mirror was used as the reference for the reflectance measurement, and measured data was corrected with theoretical reflectance of Al whose optical constants were taken from Palik [24].

To measure spectral hemispherical reflectance $R_\lambda^\cap$ at near-normal (8°) incidence, the sample was mounted on the back port of the IS. As pictured in Figure 10 (b), a Kapton insulated flexible heater (KHLV-101/10, Omega) was used along with a copper plate to provide sample heating in air for the temperature dependent $R_\lambda^\cap$ measurements. A K-type thermocouple is inserted into the copper plate from the side to measure the sample temperature with a temperature logger (USB-TC01, National Instruments), while a DC power supply is used to vary the sample temperature by manually adjusting the voltage input. After the steady state is reached at a desired sample temperature, the temperature-dependent spectral hemispherical reflectance of the sample is then measured. The same procedure is followed to measure the reflectance at higher temperatures up to 100°C by incrementally increasing voltage input of the power supply.

The spectral hemispherical reflectance $R_\lambda^\cap$ at variable incidence angles and different polarizations are measured with a custom center mount as shown in Figure 10 (c-1) with a Si reference sample held in place by an alligator clip and bottom groove. By adjusting the positions of the focusing lens in front of the IS, the monochromatic light is

refocused onto the sample mounted on the center stage as pictured in Figure 10 (c-2). An optical polarizer (WP25M-UB, Thorlabs) was placed before the IS entrance port to selective transverse-electric (TE) or transverse-magnetic (TM) polarized incident waves by rotating the polarizer as shown in Figure 10 (c-3). Finally, the incidence angle θ_i is varied by rotating the center stage with the marked radial dial shown in Figure 10 (c-4).

In order to validate the optical measurements with the IS setup, a lightly doped 500-μm-thick (110) Si wafer (60 Ω-cm resistivity, boron doped, Virginia Semiconductor) was measured for the near-normal incidence at room temperature from 0.4 to 1.6 μm in wavelength in Figure 38 (a), and at multiple oblique incidence angles (i.e., θ_i = 10°, 30°, 45°, 60°) from 0.4 to 0.9 μm in wavelength in Figure 38 (b) and (c) respectively for TE and TM waves. The measured reflectance matches the theoretical reflectance calculation of Si with optical constants from Palik [80] within acceptable 5% difference.

3.4 Optical Model

The effective medium theory (EMT) is a homogenization method widely used for characterizing the optical properties of an inhomogeneous medium with different material constituents based on the field average. This theory can be used when the characteristic dimension of the constituent is considerably smaller than the wavelength of the incident radiation. In general, two types of approximations, Maxwell Garnett (MG) [81] and Bruggeman (BR) [82], can be adopted for the EMT calculation, both of which provide expressions of the effective dielectric function for the inhomogeneous medium. In this study the BR theory was used because it works better for high volume filling ratios while

the MG method, which neglects the interaction among individual constituents, is known to provide good approximation up to filling ratio of 0.5 [82].

The BR theory treats all constituents equally as fillers in a homogeneous medium which possesses the average properties of the composite. The effective dielectric function $\varepsilon_{\text{eff}}^{\text{BR}}$ of the nanoporous gold layer can be calculated by solving [31]:

$$\frac{f(\varepsilon_1 - \varepsilon_{\text{eff}}^{\text{BR}})}{\varepsilon_{\text{eff}}^{\text{BR}} + g(\varepsilon_1 - \varepsilon_{\text{eff}}^{\text{BR}})} + \frac{(1-f)(\varepsilon_2 - \varepsilon_{\text{eff}}^{\text{BR}})}{\varepsilon_{\text{eff}}^{\text{BR}} + g(\varepsilon_2 - \varepsilon_{\text{eff}}^{\text{BR}})} = 0 \qquad 3.2$$

Considering the randomness of pore shapes, the depolarization factor is taken as g = 1/3 in all three $x/y/z$ directions such that the NPG film can be treated an isotropic structure. By taking ε_1 = 1 for the air pores, and $\varepsilon_2 = \varepsilon_{\text{gold}}$ for the bulk gold matrix, the effective dielectric function of NPG is

$$\varepsilon_{2,\text{eff}} = 0.25\left(x \pm \sqrt{x^2 + 8\varepsilon_{\text{gold}}}\right) \qquad 3.3$$

where $x = (2-3f)\varepsilon_{\text{gold}} + (3f-1)$. Note that the "$\pm$" sign should be decided for positive imaginary part of $\varepsilon_{2,\text{eff}}$. Optical constants from the Johnson and Christy [83] which include the intraband absorptions among different sub-energy levels within the conduction band at wavelengths below 650 nm, were used for the bulk gold in all theoretical calculations.

As illustrated in Figure 11, considering the light incident from air (n_1 =1) at an angle of θ_1 to a semi-infinite isotropic nanoporous gold layer with effective homogeneous dielectric function $\varepsilon_{2,\text{eff}} = m_{2,\text{eff}}^2$, where $m_{2,\text{eff}}$ is the effective complex refractive index, the spectral-directional reflectance at the interface is given for the TE (or *s*-polarized) waves by [84]:

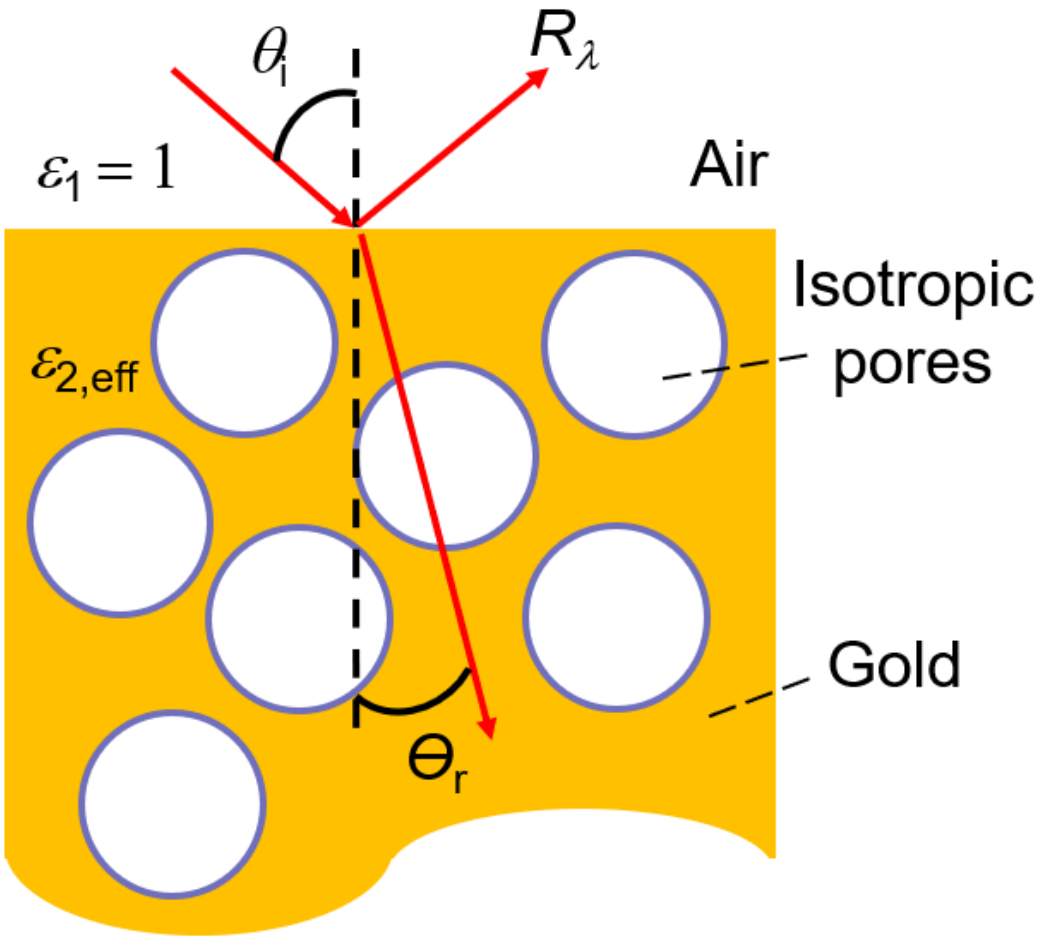

Figure 11: Schematic of a nanoporous gold film with isotropic pores in gold matrix with an effective dielectric function $\varepsilon_{2,\text{eff}}$ from the effective medium theory. The light is incident from air (ε_1 = 1) at an angle of θ_1 and wavelength λ with the spectral reflectance R_λ. As the layer thickness is much larger than the penetration depth, the nanoporous gold layer is considered to be semi-infinite here.

$$R^s = \left|r_{12}^s\right|^2 = \left|\frac{n_1 \cos\theta_i - m_{2,\text{eff}} \cos\theta_2}{n_1 \cos\theta_i + m_{2,\text{eff}} \cos\theta_2}\right|^2 \quad 3.4$$

and for TM (or p-polarized) waves by:

$$R^p = \left|r_{12}^p\right|^2 = \left|\frac{m_{2,\text{eff}} \cos\theta_i - n_1 \cos\theta_2}{m_{2,\text{eff}} \cos\theta_i + n_1 \cos\theta_2}\right|^2 \quad 3.5$$

where r is the Fresnel reflection coefficient, and θ_2 is the refraction angle inside the NPG gold calculated from $\sin\theta_2 = \sin\theta_i / m_{2,\text{eff}}$ based on the Snell's law. The complex refractive index $m_{2,\text{eff}}$ is related with the refractive index $n_{2,\text{eff}}$ and extinction coefficient $k_{2,\text{eff}}$ as $m_{2,\text{eff}} = n_{2,\text{eff}} + ik_{2,\text{eff}}$.

At normal incidence, the spectral reflectance can be simplified as:

$$R_N = |r|^2 = \frac{(n_{2,\text{eff}} - 1)^2 + k_{2,\text{eff}}^2}{(n_{2,\text{eff}} + 1)^2 + k_{2,\text{eff}}^2} \quad 3.6$$

3.5 Modeled and Measured Reflectance Comparison

Figure 12(a) shows the measured spectral near-normal hemispherical reflectance at room temperature for eight fabricated NPG samples with different PVF f values from 45% to 60% and different pore diameters as listed in Table 1. It is seen that the optical reflectance is about 0.15 from 0.4 μm to 0.5 μm regardless, the particular sample, and then starts increasing as high as 95% at longer wavelengths. The reflectance increases more sharply for the NPG sample with smaller PVF. For example, Sample 1 with f = 45% reaches the plateau with reflectance higher than 0.9 starting at the wavelength λ of 0.9 μm, while Sample 2 with f = 53% achieve the same reflectance of 0.9 at λ = 1.2 μm. The measured reflectance spectrum increases less sharply at smaller slopes in wavelengths from 0.5 μm

to 1.6 μm for larger PVF as observed from Sample 1 to Sample 6. Interestingly, both Samples 7 and 8 exhibit smaller reflectance around 0.5 in the near infrared region from the optical measurement than Sample 6, despite all three samples have the same PVF of 60%. Note that in the optical modeling the effect of residual Ag is neglected as most NGP samples have extremely low Ag content with less than 6 vol.%. In fact, by taking into 12 vol.% residual Ag (for Sample 1) in the Bruggeman effective medium model, the calculated optical reflectance showed minor changes compared to the case without residual Ag, which confirms the negligible effect of residual Ag here.

In order to validate the observed behavior of the measured optical reflectance from different NPG samples, theoretical reflectance was calculated under normal incidence based on the aforementioned EMT method and optical model. As shown in Figure 12(b), the theory predicts similar reflectance spectra as the reflectance little changes around 0.15 in the short wavelengths, then sharply increases at wavelengths beyond 0.5 μm, and finally reaches a plateau with reflectance more than 0.9 in the longer wavelength. In addition, the modeling qualitatively captures the dependence on the PVF as the reflectance at a given wavelength decreases monotonically with larger f values from 0.4 to 0.7, which agrees with the observation from measured data for Samples 1 to 6. On the other hand, the optical model used here cannot directly explain different behaviors of Samples 7 and 8 from Sample 6 with the same PVF, because (i) the EMT only considers the sole effect of filling fraction by assuming that the characteristic length (i.e., pore diameter) is much smaller than the wavelength of interests and (ii) the shrinkage effects are neglected. This should be valid for Samples 1 to 6 not only from the acceptable agreement on the reflectance spectra between the measurement and modeling, but also from the small pore diameters less than

35 nm characterized from the SEM. On the other hand, as listed in Table 1, Samples 7 and 8 possess much larger pore diameters of 50 nm and 65 nm, whose effect on the optical properties should not be neglected. In this case, the EMT approximation is not valid and full-wave numerical simulation based on finite-element frequency domain method or finite-difference time domain [82] method should be employed for more accurate modeling.

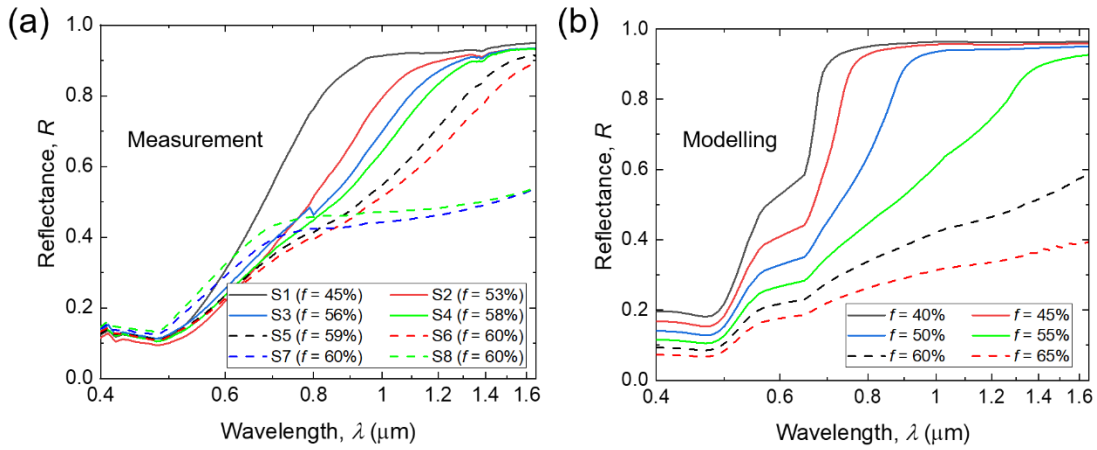

Figure 12: (a) Optical measurements of spectral near-normal hemispherical reflectance of fabricated nanoporous gold samples with different pore volume fractions at room temperature. (b) Predicted spectral normal reflectance of semi-infinite nanoporous gold with different pore volume fractions from the optical modeling.

For better understanding the optical behavior of nanoporous gold with different pore volume fractions, the effective refractive index (n_{eff}) and extinction coefficient (k_{eff}), calculated from the EMT method with f values from 0.4 to 0.65 as well as for bulk gold (i.e., $f = 0$), are respectively shown in Figure 13(a) and (b). In the wavelength range from 0.4 μm to 0.5 μm, both n_{eff} and k_{eff} have a small change with wavelength λ or the PVF f due to large refractive index of bulk gold. More importantly, n_{eff} has values around 1.4, and k_{eff} is less than 1, which results in low normal reflectance around 0.15 within the short

wavelength range simply according to Eq. (3.6) for the NPG as observed in Figure 12. In the intermediate wavelength range from 0.5 μm to 0.8 μm for f = 0.45 or until the optical reflectance reaches the plateau, n_{eff} of NPG is decreased dramatically mainly because of that of bulk gold, while k_{eff} increases considerably with smaller PVF, undoubtedly leading to increasing normal reflectance as seen in Figure 12. It should be noticed that the effective extinction coefficient k_{eff} has three turning points [85] around the wavelengths of 0.5 μm,

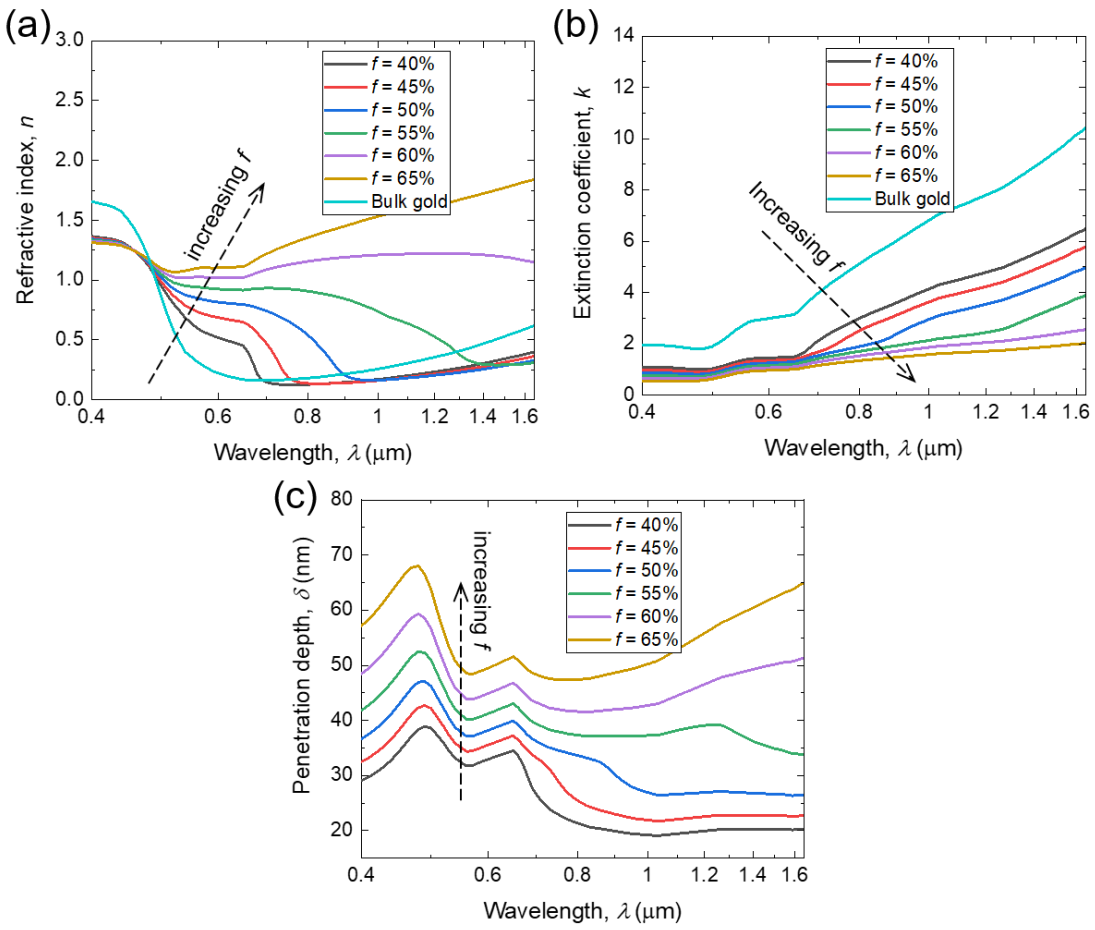

Figure 13: (a) Refractive index n, (b) extinction coefficient k, (c) penetration depth δ of the nanoporous gold in the wavelength range from 0.4 to 1.6 μm calculated from the BR effective medium theory at different volume fractions f of air pores from 40% to 65%.

0.55 μm, and 0.65 μm, which are associated with the intraband transitions of bulk gold. This explains the same three turning wavelengths on the calculated reflectance spectra of nanoporous gold in Figure 12(b). At longer wavelengths, when the effective extinction coefficient k_{eff} becomes much larger than the refractive index n_{eff}, the NPG becomes highly reflective with normal reflectance value is approaching 1 as predicted by Eq. (3.6) with $n_{\text{eff}} << k_{\text{eff}}$. This explains the reason for the high reflectance plateau redshift towards longer wavelengths for nanoporous gold with smaller filling ratios, as clearly observed both experimentally and theoretically in Figure 12.

Besides, the effective penetration depth, defined as $\delta_{\text{eff}} = \frac{\lambda}{4\pi k_{\text{eff}}}$ was calculated as a function of wavelength λ for nanoporous gold with different pore volume fractions *f*. As shown in Figure 13 (c), δ_{eff} increases with bigger pores, while the largest penetration depth is about 70 nm for considered *f* values from 0.4 to 0.65 that cover all the volume fractions from all fabricated NPG samples. Note that the optical power is attenuated to be 37% (i.e., e^{-1}) of the incidence within one δ_{eff} into the medium, 5% (i.e., e^{-3}) within $3\delta_{\text{eff}}$, or 0.7% (i.e., e^{-5}) within $5\delta_{\text{eff}}$ depth. As the thickness of the porous gold samples is about 700 nm, which is 10 times more than the largest δ_{eff} value from the effective medium calculation, the incident light should be entirely attenuated away inside the nanoporous gold layer before reaching the bottom interface. Therefore, it is reasonable to assume the porous gold to be semi-infinite without considering it as a thin film, which validates the simple optical model used here for the theoretical calculations.

Figure 14 (a) and (b) present the measured spectral-directional hemispherical reflectance of fabricated porous gold (Sample 1) at different incidence angles (θ_i = 10°,

30°, 45°, 60°) respectively for TE and TM polarized waves. At the wavelengths less than λ = 0.8 μm where the high-reflectance plateau begins for Sample 1, the measured reflectance increases with larger angles of incidence for TE waves, while it decreases slightly for TM waves at oblique angles. On the other hand, at longer wavelengths beyond λ = 0.8 μm the high reflectance stays around 0.95 and little changes for both polarizations. The similar behaviors are well predicted by the optical modelling for TE and TM waves respectively shown in Figure 14 (c) and (d). Note that for TE waves, the reflectance monotonically increases with incidence angle θ_I as analytically indicated by Eq. (3.4). This is apparent with low reflectance at short wavelengths where n_{eff} is larger or comparable to k_{eff}. At longer wavelengths exceeding λ = 0.8 μm, k_{eff} becomes more than 10 times larger than n_{eff} as seen from Figure 13 for pore filling ratio f = 0.45 (i.e., Sample 1), such that the effect of incidence angle is diminished by the close-to-unity reflectance due to the high optical loss. While TM waves share the same reason of nearly perfect reflection and large k_{eff} values for almost constant reflectance at the longer wavelengths at different incident angles, the slightly decreasing reflectance with larger θ_I at the shorter wavelengths is actually because of Brewster effect. For non- or lightly absorbing materials (i.e., k = 0 or $n >> k$), Eq. (3.5) suggests that there exists an incidence angle, namely Brewster angle $\theta_B = \tan^{-1}(n_{eff})$, at which the reflectance is minimum or zero (for non-absorbing material) [84]. By taking n_{eff} = 1.3 from Figure 13 (a) in the wavelengths from 0.4 μm to 0.5 μm, the Brewster angle is predicted to be θ_B = 52.4°. Note that, the reflectance for TM waves at a given wavelength should decrease with Incidence angle θ_I increasing from normal incidence (0°) to reach a minimum at θ_B = 52.4°, and then increases up to 1 at the grazing

angle (90°). This also explains why the calculated reflectance for θ_i = 45° and 60° is almost the same as shown in Figure 14 (d). In order to better illustrate the angular dependence of the reflectance, Figure 14 (e) and (f) plot the calculated reflectance as a function of incidence angle θ_i at selected two nominal wavelengths of λ = 0.5 μm and 1 μm respectively for TE and TM waves. At the short wavelength λ = 0.5 μm, the reflectance monotonically increases with θ_i from R = 0.1 at θ_i = 0° up to 1 at 90° for TE waves but decreases first to a minimum at θ_B = 52.4° and then reaches R =1 at θ_i = 90° for TM waves. On the other hand, the reflectance at the long wavelength λ = 1 μm remains high above 0.9 for both polarizations, while a minimum reflectance can still be seen for TM waves as diminished Brewster effect due to the large k_{eff} values.

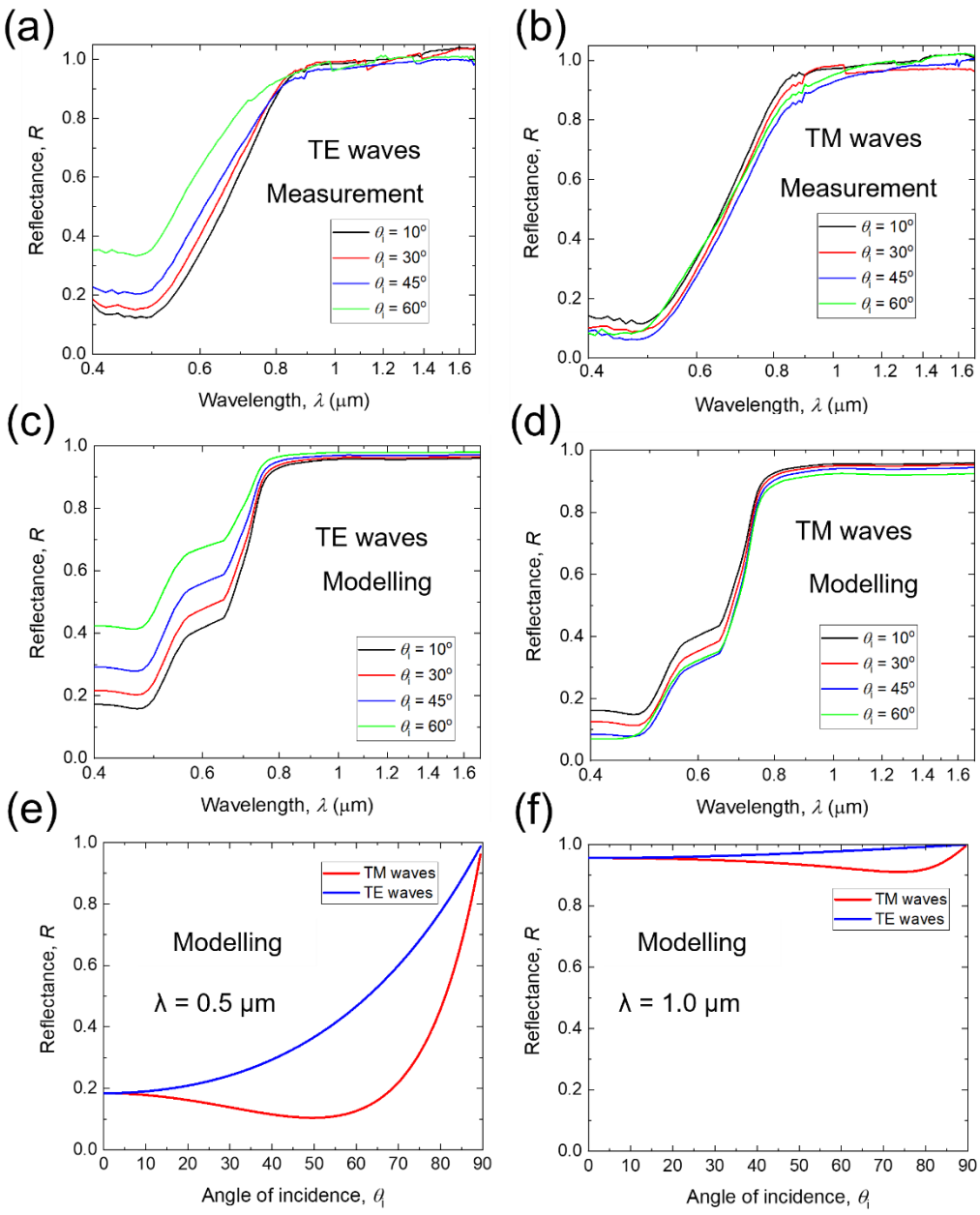

Figure 14: Optical measurements of spectral directional hemispherical reflectance of fabricated nanoporous gold (Sample 1) at different incident angles for (a) TE and (b) TM polarized waves. Modelled spectral directional reflectance of semi-infinite nanoporous gold with volume filling ratio f = 45% at different incident angles for (c) TE and (d) TM polarized waves, and angular reflectance as a function of incidence angle for both polarizations at the selected wavelengths of (e) λ = 0.5 μm and (f) λ = 1 μm.

Finally, the spectral near-normal hemispherical reflectance of the NPG films was measured from room temperature up to 100°C for Samples 2 and 3 as shown in Figure 15 (a) and (b), respectively. Since there was no observable change in the temperature-dependent reflectance spectra from both samples, excellent thermal stability upon heating in ambient with temperatures below 100°C was clearly indicated for the fabricated NPG samples. This was also consistent with observations in literature when the NPG was annealed up to 85°C [86]. However, NPG heating at higher temperatures with excessive thermodynamic energy could possibly trigger morphology change governed by thermal coarsening of nanoporous structure due to the metastability of the ligament-pore network [86]. The thermal stability and temperature-dependent optical properties of NPG need to be studied at temperatures higher than 100°C with more precise control of sample heating.

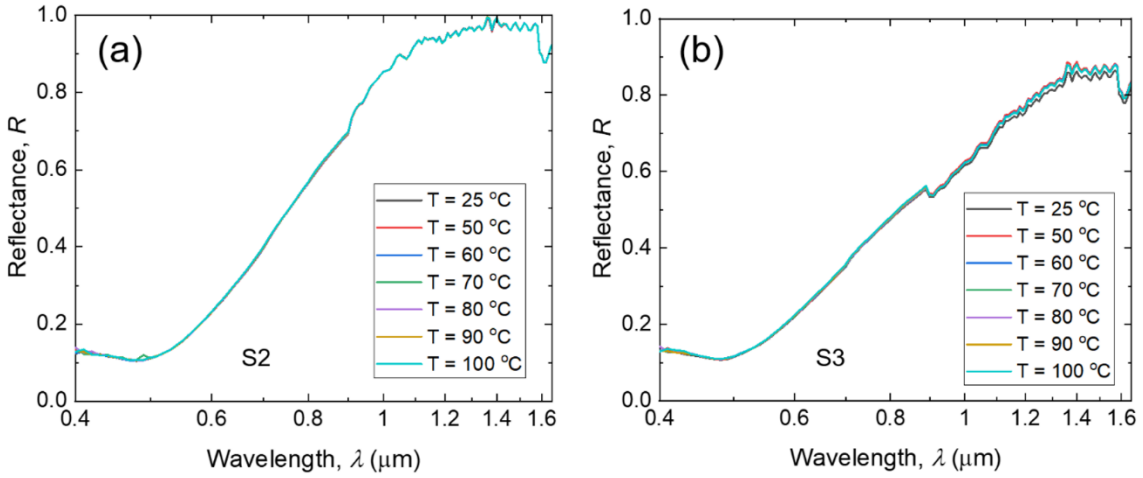

Figure 15: Temperature-dependent spectral near-normal hemispherical reflectance in the visible and near-infrared spectral range from room temperature up to 100°C for fabricated nanoporous gold: (a) Sample 2 (S2) and (b) Sample 3 (S3).

CHAPTER 4

IN-SITU TEMPERATURE DEPENDENT OPTICAL CHARACTERIZATION AND MODELING OF DEALLOYED THIN-FILM NANOPOROUS GOLD ABSORBERS

In this chapter, for understanding the evolution of the morphology at elevated temperatures and optical properties of nanoporous gold thin films fabricated by dealloying (described in the prior chapter) on quartz substrates, the (a) ex-situ hemispherical and (b) in-situ specular temperature-dependent reflectance was studied at wavelengths between 400 and 1000 nm. The morphology evolution of ligaments was captured by SEM analysis of before and after heating samples up to 500 °C and the final ligament diameter showed an Arrhenius relationship with temperature in accordance with theory [44]. The ex-situ set-up measured, at room-temperature, the hemispherical and diffuse reflectance of NPG samples as a function of their annealed temperature. This data suggested that the hemispherical reflectance tends towards that of bulk gold (Figure 18) with increasing annealing temperature. The increasing diffuse reflectance from ex-situ optical measurements confirms stronger scattering effect from increasing surface roughness due to ligament coarsening at elevated temperatures. The in-situ fiber-optic setup continuously measured the spectral specular reflectance during heating which reduced with increasing temperature as a result of increasing ligament diameter. This increase was attributed to surface roughness in the samples which were assumed to be proportional to the ligament size. The in-situ temperature dependent specular reflectance was compared with results obtained from optical modeling based on the Bruggeman (BR) effective medium theory, and Fresnel coefficients including the surface scattering effect.

4.1 Lab-scale Fiber-optic Reflectance Measurement Equipment

The temperature dependent specular reflectance of the fabricated sample was measured using a custom-built fiber optic reflectance setup shown in Figure 16 (a). This setup consists of a broadband quartz tungsten-halogen (QTH) lamp (Thorlabs SLS201) that emits light to be coupled into and transmitted through a bifurcated fiber bundle (Thorlabs RP28) until it exits through a collimator (Thorlabs F260SMA-A). The light is then incident upon the sample through air with the distance between the collimator and the sample surface about 20 mm. The QTH lamp and CCD spectrometer (Thorlabs CCS200) shown in Figure 16 (b) are connected to either end of the bifurcated fiber bundle and the latter receives the reflected light from sample surface returning through the same collimator (Figure 16 (c)) and records the wavelength dependent optical signal. The size of the light spot controlled by an iris is about 4 mm in diameter on sample surface. As the samples are diffuse, the optical setup only collects the normally reflected signals and thereby measures the spectral specular reflectance at normal direction.

The procedure for the optical characterization is as follows. First, the NPG samples were mounted to the heater setup and the collimator is adjusted to reach maximum signal strength for the reflected broadband light to achieve best optical alignment. The heater is then switched on to heat up the sample with temperature changed incrementally to the required value. After the reflected optical signal from the sample surface at a given temperature (S_{sample}) is taken, the sample setup is replaced by a silver mirror mounted on the optical rail whose reflected signal (S_{Ag}) is measured to be used as reference. The integration time (i.e., the acquisition time of 1 signal) from the CCD spectrometer is set to 100 μs, and the values averaged over 100 ms is used for calculation. The measured

reflectance of the sample (R_{sample}) is then calculated by taking the ratio of the reflected signal from the NPG sample to the reflected signal from the silver mirror, followed by the correction with theoretical reflectance of Ag (R_{Ag}) whose optical constants are taken from Palik [80] as:

$$R_{sample} = \frac{S_{sample}}{S_{Ag}} \times R_{Ag} \tag{4.1}$$

Following the same procedure, the reflectance of a lightly doped 500-μm-thick (110) Si wafer (60 Ω-cm resistivity, boron doped, Virginia Semiconductor) was measured under the normal incidence at room temperature from 400 to 1000 nm in wavelength to validate the optical measurements using the fiber-optic setup. The theoretical reflectance of Si with optical constants from Palik [80] matches the measured reflectance within acceptable 5% difference as shown in Appendix B Figure 39.

In order to heat the NPG samples to high temperatures, an ambient heater assembly was built. As shown in Figure 16 (a), a cartridge heater (Omega, CSH-101100) was press-fitted inside a custom-machined stainless-steel base covered by a nickel-plated copper disk where the NPG sample was fixed onto with uniform heating. A K-type thermocouple (TC) probe (Omega KMTXL) with oxidation-resistive sheath was inserted into the copper disk from side for temperature measurement of the sample. Modeling (refer supplementary document) was done and temperature difference between the thermocouple measurement and the porous gold layer will be <7 K for a temperature measurement of 723 K by the TC. The stainless-steel base was placed inside a firebrick for thermal insulation with aluminum casing whereas the sample surface was open to face the collimator (see Appendix B Figure 40 for a complete schematic of the set-up). A proportional–integral–derivative (PID)

temperature controller (Omega CSi8D) was used to heat the sample temperature to a desired setpoint and maintained it within ±7 °C once reached. The in-situ reflectance data was collected from five samples which were heated to different final temperatures (i.e., 125, 200, 275, 350, and 500 °C) in small stepwise increments. The reflectance measurements were collected at 0, 2 and 5 min after each temperature increment crosses the setpoint and the results were then averaged for a given setpoint temperature. Refer to Appendix B Figure 41 and Figure 42 for the temperature histograms of each sample and their raw data collected at 0, 2, and 5 min.

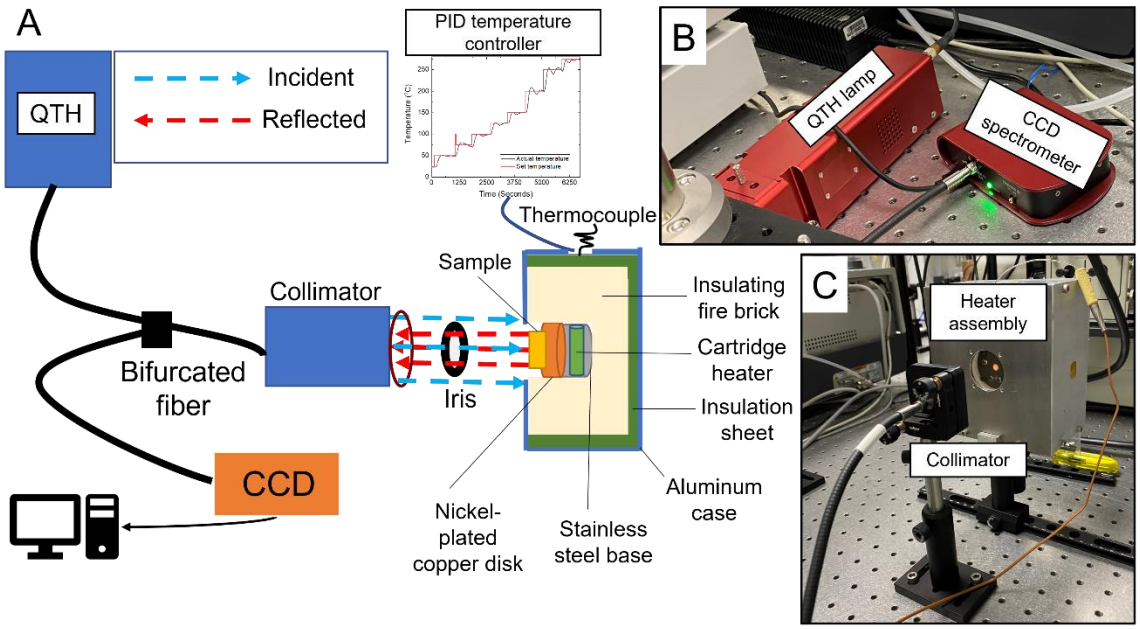

Figure 16: (a) Optical layout of the high-temperature reflectance measurement setup consisting of a QTH light source, a heater assembly, a CCD spectrometer, optic fibers, and a collimator. (b) QTH lamp and CCD spectrometer connected to either ends of the bifurcated fiber cable. (c) Collimator focusing light on the sample mounted inside the heater assembly.

4.2 Thermal Annealing and Ligament Coarsening

Nanoporous gold samples undergo a thermal coarsening process [44] that is manifested as a continuous increase in the ligament diameter with heating temperature driven by surface or bulk diffusion [87] that drives the coalescence of smaller ligaments into larger ones. To correlate the in-situ reflectance data from the fiber-optic probe (Figure 16) to the morphology of the NPG samples, it was first necessary to study separately the morphology evolution of the samples with SEM images before and after heating to benchmark its temperature-dependent morphology. This was accomplished by heating samples to different maximum temperatures and cooling them by blowing air using a fan to analyze its temperature-dependent morphology (Figure 17 – post-heating) and compare it to its initial state (see Figure 17 – Pre-heating and Table 2).

Table 2: Initial and final ligament diameter, maximum sample heating temperature, pore diameter, pore area fraction, residual silver content, and apparent pore volume fraction (*f*) of the fabricated NPG samples.

Sample	Initial ligament diameter (nm)	Maximum temperature (°C)	Final ligament diameter (nm)	Initial pore diameter (nm)	Final pore diameter (nm)	Initial solid area fraction (%)	Initial residual silver content (at. %)	Initial apparent pore volume fraction (vol %)
1	41±13	125	42±13	26±8	24±8	71	1.8±0.3	58.1
2	38±12	200	72±34	24±7	50±16	71	2.4±0.5	57.5
3	40±13	275	111±46	25±8	99±40	71	1.9±0.3	58.0
4	35±12	350	211±80	23±7	214±73	71	2.2±0.2	57.7
5	40±13	500	299±114	26±8	263±85	71	2.1±0.4	57.8

The image analysis on the SEM images shows that the ligament diameter increased after 125 °C proportionally with temperature to a maximum of 299 nm for the heat treatment at 500 °C from an initial size of ranging from 35 to 41 nm (see Table 2).

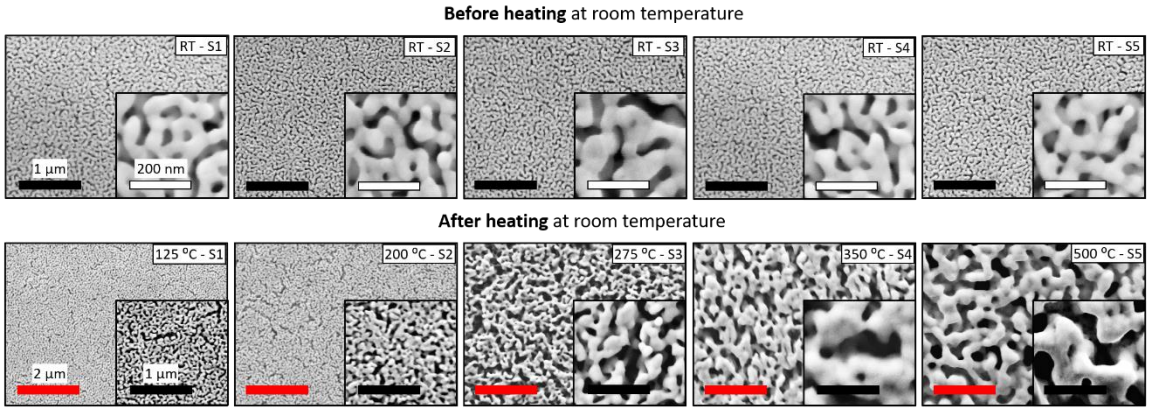

Figure 17: Top view SEM images of fabricated NPG thin-film samples dealloyed at 40 °C for 30 min before and after heating: S1 (125 °C), S2 (200 °C), S3 (275 °C), S4 (350 °C), and S5 (500 °C).

4.3 Room Temperature Hemispherical and Diffuse Reflectance

Hemispherical and diffuse reflectance measurements were done at room temperature before and after the heating process using an integrating sphere to investigate their variation with initial and final ligament diameters. Detailed explanation of the integrating sphere setup and the measurement techniques can be found from Section 3.3. Figure 18 (a) shows the measured near-normal hemispherical reflectance of the NPG samples before and after heating. Note that the hemispherical reflectance before heating of the 5 samples diverged at wavelengths between 700-1000 nm because of their slight differences in their initial ligament, pore volume fraction, residual silver content and pore diameter. After heating, there is a gradual increase in the diffuse reflectance with increasing

processing temperature shown in Figure 18 (b) which accounts for the majority of the increase in the hemispherical reflectance. Sample 'S2' had the lowest hemispherical reflectance before heating among all samples despite having near identical ligament size. The measurement was repeated 3 times to confirm the result. The authors hypothesize that this effect is associated with residual silver content for which Sample 'S2' exhibited the highest value. As for the data after heating, only the diffuse reflectance is expected to increase with increasing ligament size, surface roughness and temperature which is what is observed in Figure 18 (b). It is worth noting that, at 125 °C, the sample exhibited no significant changes in either hemispherical or diffuse reflectance compared to its initial value because this temperature is not high enough to activate thermal coarsening (see

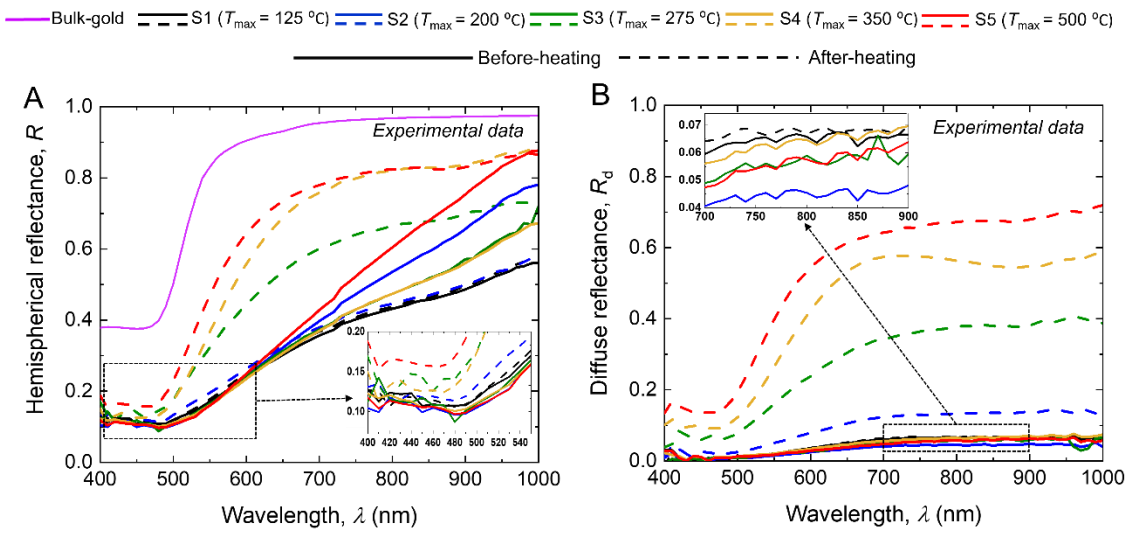

Figure 18: Room-temperature optical measurements of spectral near-normal reflectance of fabricated NPG samples dealloyed at same conditions pre- and post-heat treatment: (a) hemispherical and (b) diffuse reflectance at near-normal incidence. Solid and dashed lines correspond to measurements made before and after the heating cycle. T_{max} indicates the maximum temperature during the heating cycle.

Figure 17) which is consistent with data from differential scanning calorimetry in literature for NPG [88].

4.4 In-situ Temperature Dependent Specular Reflectance

The in-situ specular reflectance measurements (made with the optical fiber set-up shown in Figure 16) as a function of temperature are shown in Figure 19 by sample number each processed to a different maximum temperature before quenching. It is observed that the specular reflectance does not change up to 125 °C for samples 1, 2, 3 and 5 (Figure 19). In sample 4, it started decreasing at temperatures as low as 50 °C as seen from Figure 19 (d) which could be explained by the fact that sample S4 had the smallest initial ligament diameter among all the samples and thus it was the least metastable and susceptible to coarsening initiation at temperatures lower than 125 °C [88]. After 125 °C, the specular reflectance of all samples has a decreasing trend with increasing temperature (Figure 19 (b)). The onset temperature at which the reflectance changes occur varied between 150 and 200 °C for all other samples which, similarly to the hemispherical reflectance data (Figure 18), is in agreement with in-situ temperature dependent TEM observations of NPG evolution[89] and with DSC data by Hakamada et al. [88] indicating the onset temperature of thermal coarsening as low as 200 °C. The specular reflectance at wavelengths below 500 nm does not change with temperature up to 250 °C. For temperatures above 250 °C, the specular reflectance decreases over the entire wavelength regime. Finally, after 400 °C, the specular reflectance curves reach their minimum values and do not present significant changes until 500 °C (see overlapped curves for 400-500 °C in Figure 19 (e)). SEM data

in Figure 17 shows that there is substantial increase in ligament from 211 nm to 299 nm between 350 and 500 °C, and, yet variations in ligament in sample #5 (Figure 19 (e)) between 400 and 500 °C did not produce significant reflectance changes suggesting a saturation in its reduction. Typically, as per other reports in other literature [89], it is expected to go through considerable volume shrinkage due to coarsening at temperatures as low as 200 – 300 °C, achieving major structural densification by 400 °C [89] which may be the possible reason for the overlapping specular reflectance curves in the temperatures between 400 – 500 °C. Note that between 0 and 5 min of any temperature increment, there is about a 5% difference in the spectra suggesting the sample is thermally unstable. However, the difference between the spectra at 0 and 2 min and the spectra at 2 and 5 min is in a decreasing trend, suggesting that the sample is stabilizing with increasing time.

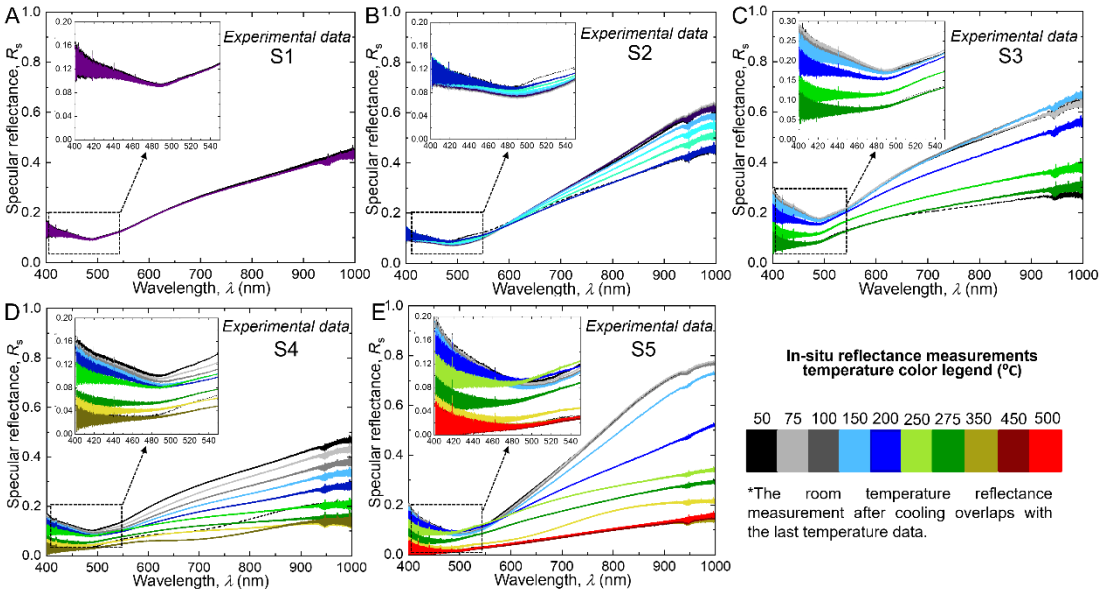

Figure 19: In-situ optical measurements of spectral near-normal specular reflectance of fabricated NPG samples heated to different temperatures as listed in Table 2: (a) Sample 1 (S1, T= 125 °C), (b) Sample 2 (S2, T= 200 °C), (c) Sample 3 (S3, T= 275 °C), (d) Sample 4 (S4, T= 350 °C), and (e) Sample 5 (S5, T= 500 °C) using the fiber optic setup.

4.5 Theoretical Model

The effective medium theory (EMT) is used to describe the effective optical constants of NPG samples, and Bruggeman (BR) theory [82] was used as it is most suitable for large filling volumes and interconnected inclusions. The effective dielectric function ε_{eff}^{BR} of the NPG layer can be determined by [82]:

$$\frac{f(\varepsilon_1 - \varepsilon_{eff}^{BR})}{\varepsilon_{eff}^{BR} + g(\varepsilon_1 - \varepsilon_{eff}^{BR})} + \frac{(1-f)(\varepsilon_2 - \varepsilon_{eff}^{BR})}{\varepsilon_{eff}^{BR} + g(\varepsilon_2 - \varepsilon_{eff}^{BR})} \quad 4.2$$

where f is the volumetric fraction of air pores, $\varepsilon_1 = 1$ is the dielectric function of air pores and $\varepsilon_2 = \varepsilon_{\text{gold}}$ is for the bulk gold matrix obtained from Johnson and Christy [90]. The optical constants of bulk gold obtained from Johnson and Christy [90] is used for the calculations as it included the intraband absorptions among different sub-energy levels within the conduction band that occurs below wavelengths of 650 nm (that falls within the wavelength domain in this study) which is not captured by the Drude-Lorentz model used elsewhere in literature [91]. The depolarization factor is taken to be g = 1/3 due to the randomness of the pore distribution. The effective dielectric function of the NPG structure can be found in a simplified form as

$$\varepsilon_{\text{eff}} = 0.25\left(x \pm \sqrt{x^2 + 8\varepsilon_{\text{gold}}}\right) \quad 4.3$$

where $x = (2-3f)\varepsilon_{\text{gold}} + (3f-1)$. The "$\pm$" sign should be decided for positive imaginary part of ε_{eff}. The specular reflectance at normal incidence for an optically smooth surface between air and the opaque NPG layer can be calculated by [92]:

$$R_N = \frac{\left(n_{eff} - 1\right)^2 + k_{eff}^2}{\left(n_{eff} + 1\right)^2 + k_{eff}^2} \tag{4.4}$$

where n_{eff} and k_{eff} are respectively the refractive index and the extinction coefficient of the porous gold obtained from:

$$\varepsilon_{\text{eff}} = (n_{\text{eff}} + ik_{\text{eff}})^2 \tag{4.5}$$

For rough surfaces with the autocorrelation length and the root-mean-square roughness (σ_{rms}) are much less than the wavelength of the incident light, the specular normal reflectance can be modified to consider the effect of surface roughness via[92]:

$$R = R_N \times |S|^2 \tag{4.6}$$

with scattering factor

$$S = \exp\left[-\frac{1}{2}\left(\frac{4\pi\sigma_{rms}cos\Theta_i}{\lambda}\right)^2\right] \tag{4.7}$$

Note that λ is the wavelength in free space and θ_i is the angle of incidence, which is zero under normal incidence.

Note that in the optical modeling the effect of temperature and apparent pore volume fraction on the reflectance of NPG thin film is neglected and the calculations with these effects included are shown in the Appendix B section.

4.6 Surface Roughness Dependent Reflectance

The relevance of the in-situ specular reflectance measurements shown in Figure 19 depends on the ability to translate this real-time monitoring of wavelength-dependent

information measured from the NPG surface into a prediction of its morphology (e.g., ligament size). Given that the sample is thermally coarsening, ligament size is expected to correlate to its surface roughness, which in turn affects the specular reflectance via the scattering factor shown in Eq. 4.7. Therefore, surface roughness becomes an important temperature-dependent parameter in the optical model for varying specular reflectance at different temperatures. Here, relative specular reflectance (RSR) change is proposed as a factor to predict ligament size based on measured specular reflectance at different temperature and is defined as:

$$RSR_{exp}(T) = \frac{R_i(T_0) - R_f(T)}{R_i(T_0)} \tag{4.8}$$

where $R_f(T)$ and $R_i(T_0)$ are the normal specular reflectance at an elevated temperature T and room temperature T_0, respectively. *RSR* was plotted as a function of $\frac{1}{k_B T}$ (See Figure 20 (a)) at a particular wavelength of 1 μm, where it exhibited the maximum reflectance changes upon heating where k_B is the Boltzmann constant. The *RSR* factor reduces the in-situ reflectance data for all samples in Figure 19 to a single temperature-dependent relation that is invariant to the sample-to-sample variations in specular reflectance.

To predict ligament size using RSR, it was necessary to not only correlate it to temperature but also to roughness and ligament size. This was accomplished in a two-step approach. First, ligament size dependence on temperature was captured using an Arrhenius equation, $L = Ae^{-\left(\frac{nE_a}{k_B T}\right)}$, in which A is a constant, n is coarsening exponent and E_a is the activation energy[93]. By analyzing ligament size data from Figure 17 as a function of the maximum temperature and plotting it against $\frac{1}{k_B T}$ Figure 20(b)), nE_a of 0.1441 eV was

obtained which closely matched results obtained by McCue et al.[44]. Using this fitted Arrhenius equation, the ligament diameter was extrapolated for all temperature (Figure 20 (a)) and, thus, establishing a relationship between the latter and RSR.

Secondly, the specular reflectance and RSR dependence on roughness was captured using a theoretical model which was conducted under normal incidence and is based on the EMT, and optical models discussed previously in section "Theoretical Model." The model Figure 21 (a)) qualitatively captures the increasing trend of specular reflectance with respect to wavelength (Figure 19). Further, the theory predicts reflectance changes with respect to roughness with (i) smaller changes at shorter wavelengths (i.e., <500 nm) and (ii) sharp increases beyond 500 nm, which accurately matches trends in our measurements (Figure 19). While the current model uses the permittivity of bulk gold from Johnson and

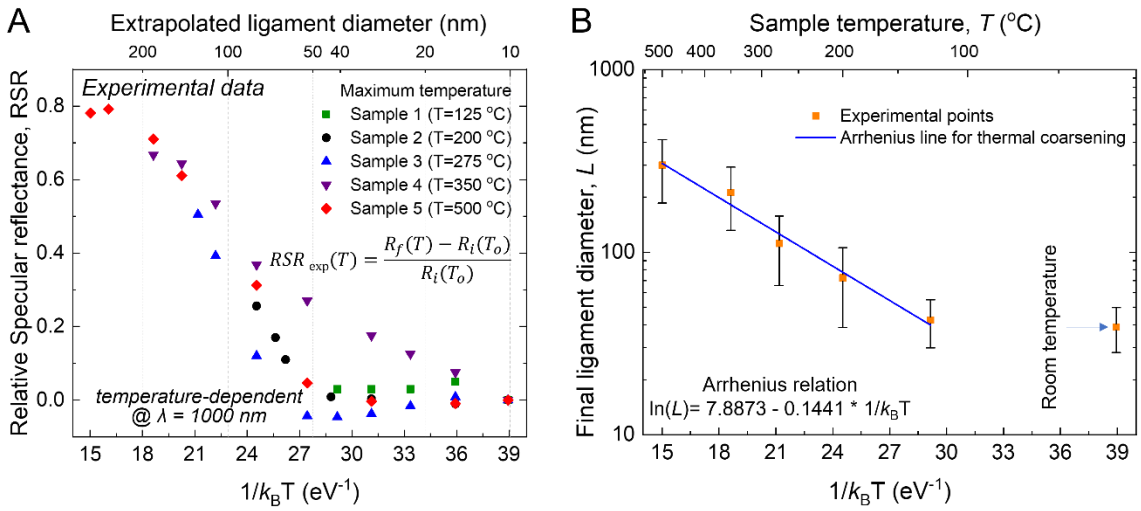

Figure 20: (a) Plot relating the relative specular reflectance at fixed wavelength of 1μm varying with temperature and ligament diameter for 5 samples exposed to different maximum temperatures. (b) Arrhenius plot containing the ligament diameter after coarsening for short durations at elevated temperatures (600-1200 sec). The blue line is the linear fit, whose slope equals $-nE_a$ and the intercept equals $\ln[(kD_0)]^n$.

Christy [90] for calculating reflectance, the effects of temperature dependent permittivity of gold thin films from literature [46] were studied and neglected as a result of light scattering due to roughness being more predominant.

To account for the surface roughness present in NPG, it is assumed that the root-mean-square surface roughness (σ_{rms}) is proportional to the ligament diameter (L), and the following equation holds:

$$\sigma(L) = cL \tag{4.9}$$

in which "c" is an empirical fit constant. Now, the increase in ligament diameter can account for an increase in surface roughness which allows for formulating a theoretical

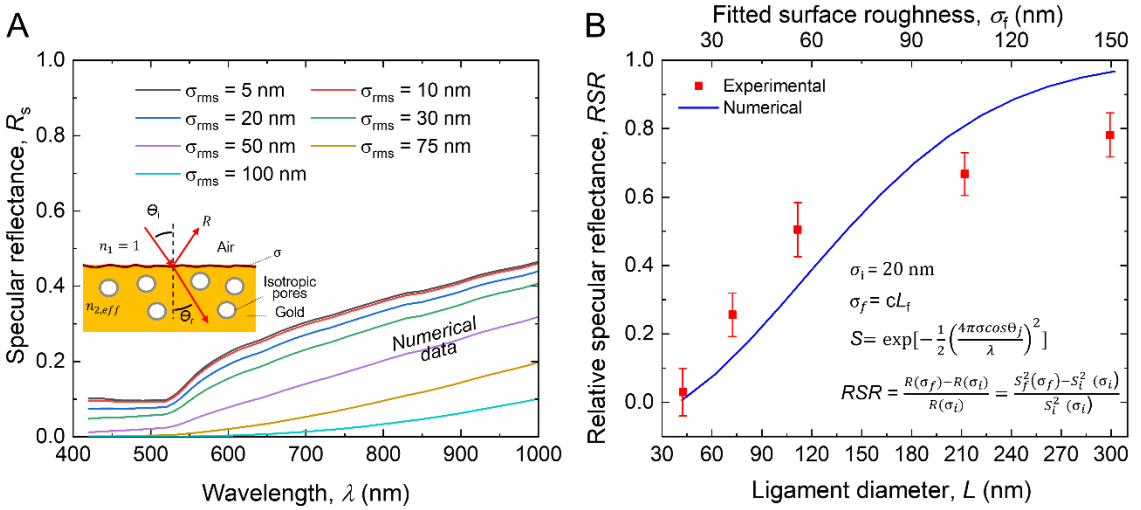

Figure 21: (a) Predicted spectral specular normal reflectance of semi-infinite NPG with root-mean-square roughness values from the optical modeling. (b) Plot relating the relative specular reflectance at fixed wavelength of 1μm varying with final ligament diameter and hence surface roughness for 5 samples exposed to different maximum temperatures considering initial surface roughness of the samples σ_i = 20 nm.

value of *RSR* as a function of roughness and ligament diameter using equations 4.6, 4.7 and 4.9:

$$RSR_{theo}(\sigma_f) = \frac{R(\sigma_i) - R(\sigma_f)}{R(\sigma_i)} = \frac{S_i^2(\sigma_i) - S_f^2\ (\sigma_f)}{S_i^2\ (\sigma_i)} = \frac{S_i^2(cL_i) - S_f^2\ (cL_f)}{S_i^2\ (cL_i)} \qquad 4.10$$

in which $R(\sigma_i)$ and $R(\sigma_f)$ are the reflectance of the sample at room temperature before and after heating respectively, and σ_i and σ_f are the root-mean-square surface roughness of the samples before and after heating respectively, *S* is the scattering coefficient calculated at 1 μm wavelength.

The average initial ligament diameter (L_i) of the 5 samples was ~ 40 ±12 nm. Based on least-squares method, by minimizing the objective function $F(c) = \sqrt{\frac{1}{N}\sum_{j=1}^{5}\left(RSR_{theo} - RSR_{exp}\right)^2}$ between the theoretical and experimental RSR values for all five samples, the only fitting parameter c is found to be 0.5 ± 0.02. As shown in Figure 21(b), the theoretical prediction of *RSR* captures with good agreement the trends in experimental *RSR*. This result strongly supports the argument that ligament size regulates roughness which, in turn, decreases the specular and increases the diffuse components of reflectance. There are at least three reasons for the numerical misfitting in Figure 21(b). Firstly, the spread in the ligament diameter distribution increases with an increase in the average ligament diameter. For example, the initial average ligament diameter of the samples is 39±12 nm and it increases to a final size of 299±114 nm. The current model in this study does not account for spatial variations in ligament diameter such as a skewness in its distribution. Secondly, the roughness is determined indirectly from ligament size using an empirical fit constant '*c*' and a linear relationship between them, which is a

reasonable assumption but an indirect approach to determine σ_{rms}. Thirdly, the dielectric function of the porous gold film used for calculating RSR_{theo} is taken to be a constant value at a particular wavelength. This assumes that the pore volume fraction does not change upon annealing and neglects shrinkage effects upon heat treatment. Thus, further improvement to the *RSR* fit can be attained by measuring the pore volume fraction and the rms surface roughness (σ_{rms}) directly. In comparison to literature, Chen et al. measured initial σ_{rms} to be 9.6 nm for chemically dealloyed NPG films at room temperature[94] and, based on their average ligament size, their empirical fit parameter '*c'* equals 0.47 which closely matches the results from this study. Further Shen et al.[46] concluded that the increased surface roughness incurred by annealing of gold thin-film contributed to increasing imaginary permittivity in the temperature range of 27 to 300 °C. Agreeing with their conclusion, this paper extends the study on the effect of temperature dependent surface roughness on optical properties to a higher temperature of 500 °C using an in-situ fiber optic setup. Surface roughness being much smaller than the wavelength of incident light causing inapplicability of geometry optics or ray bouncing leads to light scattering phenomena yielding a diffusely reflected beam.

CHAPTER 5

RADIATIVE PROPERTIES OF POROUS POWDERS

In this chapter, an integrating sphere is employed to measure the hemispherical reflectance of powder mixtures containing nanoporous copper spherical micron-sized powders and a semi-empirical model derived to predict it. Radiation transport inside dispersed media, such as powder beds, determines light reflection by their surfaces [95]. The two-flux method is used to analytically solve the Radiation Transfer Equation (RTE) [96] and predict the reflectance of pure solid and nanoporous copper powders separately. The obtained experimental results are compared to the theoretical values obtained by solving the RTE in a half-infinite homogenous body with effective radiative properties. The effective dielectric function of the copper and porous copper powders - used in the RTE model - are obtained by using the effective medium theory [82] using as an input the porosity (i.e., pore volume fraction) and its optical properties. The reflectance of the powder mixture as a function of the ratio of the nanoporous and solid copper powder content is calculated using the checkerboard method [97] that treats its reflectance as an average of their reflectance in their pure states (i.e., without mixing) weighted by the surface areas of the individual components. Finally, the error between the analytical and experimental results are plotted as a function of wavelength for different copper and porous copper mixture proportions.

5.1 Optical model

To model the powder mixture, a three-step process was followed as shown in flowchart (Figure 22).

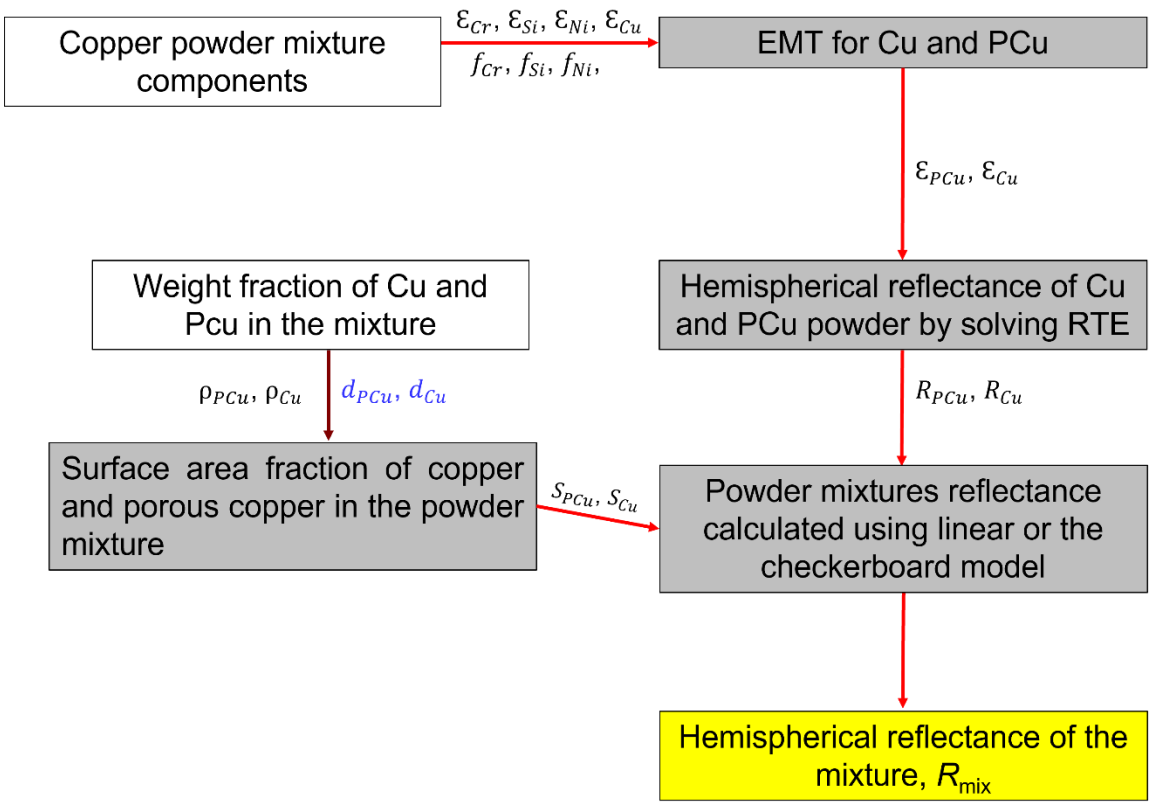

Figure 22: Flowchart depicting the modeling process to calculate the powder mixture reflectance. All the input data for the calculation have been either measured or obtained from reference except the diameters of the copper and PCu powder particles, which are guessed to close fir reflectance curves to the experimental values.

Firstly, the dielectric function of copper (Cu) powder used in the process to fabricate the porous copper (PCu) powder was modeled. The copper powder used was a mixture of 4 major components, namely, copper (96.43%), Nickel (f_{13} = 2.61%), silicon (f_{12} = 0.51%) and chromium (f_{11} = 0.45%). The Bruggeman effective medium theory (BR-EMT) model [82] was used to determine the effective dielectric function of the copper powder as the constituent particle sizes were in the Angstrom (Å) scale. The effective dielectric function of the copper powder ($\varepsilon_{Cu,eff}^{BR}$) was determined by:

$$\frac{f_{11}(\varepsilon_{Cr}-\varepsilon_{Cu,eff}^{BR})}{\varepsilon_{Cu,eff}^{BR}+g(\varepsilon_{Cr}-\varepsilon_{Cu,eff}^{BR})}+\frac{f_{12}(\varepsilon_{Si}-\varepsilon_{Cu,eff}^{BR})}{\varepsilon_{Cu,eff}^{BR}+g(\varepsilon_{Si}-\varepsilon_{Cu,eff}^{BR})}+\frac{f_{13}(\varepsilon_{Ni}-\varepsilon_{Cu,eff}^{BR})}{\varepsilon_{Cu,eff}^{BR}+g(\varepsilon_{Ni}-\varepsilon_{Cu,eff}^{BR})}+(1-$$

$$f_{11}-f_{12}-f_{13})\frac{f_{12}(\varepsilon_{Cu}-\varepsilon_{Cu,eff}^{BR})}{\varepsilon_{Cu,eff}^{BR}+g(\varepsilon_{Cu}-\varepsilon_{Cu,eff}^{BR})}=0 \quad (5.1)$$

The optical constants of copper, nickel, silicon, and chromium were obtained from Palik [80]. The depolarization factor was assumed to be g = 1/3 due to the randomness of the pore distribution. Next, the dielectric function of porous copper powder ($\varepsilon_{PCu,eff}^{BR}$) were determined using the BR-EMT again as the effective lengths were in the nanometer scale compared to wavelength scale in microns:

$$\frac{f_{21}(\varepsilon_{Cu_2O}-\varepsilon_{PCu,eff}^{BR})}{\varepsilon_{PCu,eff}^{BR}+g(\varepsilon_{Cu(II)O}-\varepsilon_{PCu,eff}^{BR})}+\frac{f_{22}(\varepsilon_{air}-\varepsilon_{PCu,eff}^{BR})}{\varepsilon_{PCu,eff}^{BR}+g(\varepsilon_{air}-\varepsilon_{PCu,eff}^{BR})}+(1-f_{11}-f_{12})\frac{(\varepsilon_{Cu,eff}^{BR}-\varepsilon_{Cu,eff}^{BR})}{\varepsilon_{Cu,eff}^{BR}+g(\varepsilon_{Cu,eff}^{BR}-\varepsilon_{PCu,eff}^{BR})}=0 \quad (5.2)$$

Based on the XRD data presented in Figure 45 (APPENDIX C), considerable quantity of Cu_2O was detected in the porous copper powder and hence has been considered for the calculation of dielectric function of PCu. The Cu_2O optical properties were obtained from literature [98]. The porous copper powder particles had a core-shell configuration with copper as the core and Cu_2O as the shell. XRD data suggested 46.1 wt.% is Cu_2O (f_{21}) and the remaining is copper. Also, 75% of pore volume fraction (f_{22}) was considered in calculating the effective dielectric function of the porous copper. The porous copper and copper powders were physically mixed in different proportions to study the variation of hemispherical reflectance.

The next step was to determine the reflectance of the powders in their pure state (i.e., either pure solid or nanoporous powders), for which the model from literature [99] was used to solve the radiation transfer equation. The reflectance of the pure copper and

porous copper powders was determined using this model. Repaving the powder bed with a homogeneous medium with effective absorbing and scattering properties in the half-space $Z < 0$.

$$\cos\theta \frac{\partial I}{\partial Z} = \beta \left[\frac{\omega}{2} \int_{-1}^{1} K(\theta', \theta) I(\theta') d\cos\theta' - I(\theta) \right] \quad 5.3$$

where θ is the polar angle as shown in Figure 23, Z the coordinate along the external normal to the surface of the powder bed, β the extinction coefficient, and ω the albedo. The kernel $K(\theta', \theta) = \frac{1}{2\pi} \int_0^{2\pi} P(\alpha) d\phi$ is calculated from the scattering phase function $P(\alpha)$. α is the scattering angle and depends on the polar angles of incident radiation (θ') and scattered radiation (θ) and is related to the azimuth angle (ϕ) as $cos\alpha = cos\theta\, cos\theta' + sin\theta\, sin\theta' cos\phi$. In Eq. 5.3, a dimensionless coordinate βZ can be introduced to eliminate the parameter β.

In this case, only the scattering phase function and the albedo influenced the reflected radiation by the optically thick powder bed. Since the powder particle sizes considered are larger than the wavelength regime, it falls into the geometric optic domain and in the approximation of geometric optics, the albedo (ω) and phase function (P) are estimated respectively as [100]:

$$\omega = R \quad 5.4$$

$$P = R'(\frac{\pi - \alpha}{2})/R \quad 5.5$$

where $R'(\chi)$ is the directional reflectance, R is the hemispherical reflectance and $\chi = \frac{\pi-\alpha}{2}$ is the incidence angle.

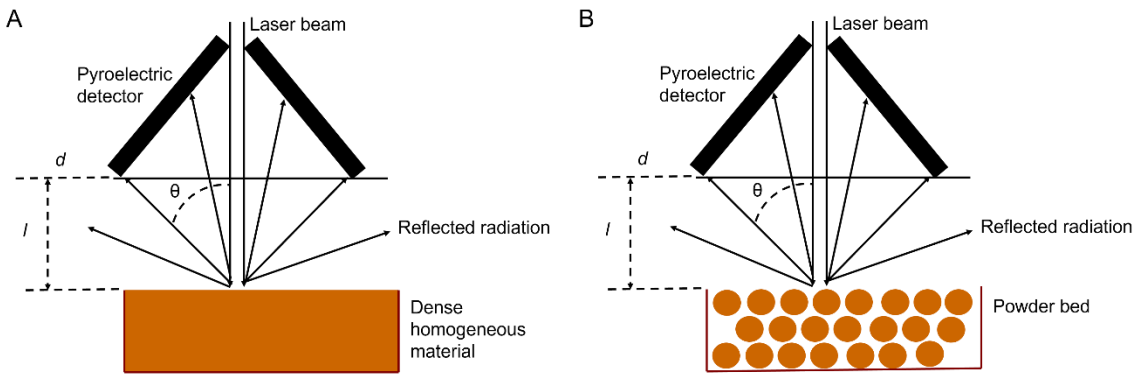

Figure 23: (a) Homogeneous dense material and (b) Powder bed hemispherical reflectance measurement layout where d is base diameter of the conic detector; *l*, distance between the detector and the sample; and θ, maximum reflection angle of collected radiation.

The hemispherical reflectance of a dense and homogeneous material (Figure 23 (a)) can be determined by [84]:

$$R = 2\int_0^1 R'(\chi)\cos\chi d\cos\chi \qquad 5.6$$

Eqns. 5.3 and 5.4 hold for closely packed bed of opaque spheres as suggested by Monte Carlo simulation [96] and hence have been used in this study to calculate the effective reflected radiation. This hemispherical reflectance value (derived from eq. 5.6) is the reflectance of semi-infinite body of solid and nanoporous copper not accounting for its powder form and its multiple internal reflectance.

The Fresnel equations are used to compute the directional reflectance of nonpolarized incoming light using the refraction *n* and extinction *k* indices [100]:

$$R' = \frac{R_\perp + R_\parallel}{w} \qquad 5.7$$

$$R_{\perp} = \frac{(nB-\cos\chi)^2+(n^2+k^2)A-n^2B^2}{(nB+\cos\chi)^2+(n^2+k^2)A-n^2B^2} \quad 5.8$$

$$R_{\parallel} = \frac{(n\gamma-\mathrm{A}/\cos\chi)^2+(n^2+k^2)A-n^2\gamma^2}{(n\gamma+\mathrm{A}/\cos\chi)^2+(n^2+k^2)A-n^2\gamma^2} \quad 5.9$$

$$A^2 = \left(1+\frac{\sin^2\chi}{n^2+k^2}\right)^2 - \frac{4n^2\sin^2\chi}{(n^2+k^2)^2} \quad 5.10$$

$$B^2 = \frac{n^2+k^2}{2n^2}\left(\frac{n^2-k^2}{n^2+k^2} - \frac{\sin^2\chi}{n^2+k^2} + A\right) \quad 5.11$$

$$\gamma = \frac{n^2-k^2}{n^2+k^2}B + \frac{2nk}{n^2+k^2}\left(\frac{n^2+k^2}{n^2}A - B^2\right)^{\frac{1}{2}} \quad 5.12$$

When a ray strikes a particle, it produces a reflected and refracted beam, but the model in this study so far only considered the reflected ray. In the case of a semitransparent particle, this causes an inaccuracy since the refracted light passes through it, leaves at the backside, and contributes to scattering. This enhances the powder's albedo, ω, resulting in a higher effective reflectance. In the case of nanoporous copper, the powder, despite having a significant pore volume fraction, it is treated as being fully absorbing and having no transmission.

Next, the effective reflectance of a powder bed is recalculated using the two-flux model of multiple scattering [96]. The effective reflectance of the powder bed (packed bed of opaque spheres as shown in Figure 23 (b)) is a function of the reflectance ρ of the dense material (Figure 23 (a)) as indicated by Monte Carlo Ray tracing simulation [96] and the two-flux model of multiple scattering [101]. The effective normal-hemispherical reflectance for isotropic scattering of a powder bed with close-packing and phase function $P = 1$, can be calculated as [96]:

$$R_e = \frac{1-\sqrt{1-R}}{1+2\sqrt{1-R}} \quad 5.13$$

To further calculate the reflectance of the mixture of the copper and porous copper powders in varying weight fraction of porous and solid copper powders, the checkerboard method [97] was used. The "checkerboard" or linear mixing model represents a mixture's reflectance spectrum, R_{mix}, as a linear combination of endmember reflectance spectra, R_j, each weighted by their fractional area, S_j. In this case, index 'j' refers to the porous and solid copper powders.

$$R_{mix} = \sum_{j=1}^{n} R_j S_j \qquad 5.14$$

The assumptions that have been made in the model are as follows:

a) The particles are spheres and isotropic scatterers (no preferential direction)

b) The particles are larger than the wavelength of light ($\frac{\pi d}{\lambda} \geq 5$)

c) Each particles scatter radiation independently of its neighbors

d) Scattering reduces to refraction and reflection in geometrical optics approximation

The reflectance of opaque particles has been shown to depend solely on the properties of the surface specimen [102]. Individual components in checkerboard mixing are weighted by area rather than volume or mass proportion. In this study, the physical mixing of the powders was done in terms of weight fraction and hence it was necessary to convert weight-percent composition to surface-area percent. The total surface area of particles of a certain shape may be proven to be inversely related to the average particle size and density as shown in the supplementary section, i.e., the percent surface area of component B (PCu) in a weight mixture of A (Cu) and B is:

$$S_B = \frac{W_B \rho_A d_A}{W_B \rho_A d_A + W_A \rho_B d_B} \qquad 5.15$$

W_A and W_B are the weight fractions (wt.%) of Cu and PCu in the powder mixture respectively; ρ_A and ρ_B, the measured apparent densities of Cu and PCu powders and d_A and d_B are the diameters of copper and porous copper powders. The diameter of the copper and porous copper powder particles ranges from 15-45 μm and 4-25 μm, respectively. Note that the diameters (d_A and d_B) are arbitrarily selected within the range of size distributions of the powders as provided by the vendor. A sensitivity analysis has been presented in the APPENDIX C section to determine the diameters used for calculations.

To benchmark the presented model, experimental results and two different models are compared. First, the hemispherical reflectance of powder mixtures was measured using an integrating sphere. Second, a complete model using equations 5.1-5.14 (model 2) which derives from textbook reflectance values and experimental compositional and morphological data. Third, a shorter model that takes the hemispherical reflectance of pure porous and solid powders (from experimental data) into equation 5.14 (model 1) to predict the reflectance of their mixtures. In summary, the calculation of hemispherical reflectance of the powder mixtures was done in two ways and:

1. The measured hemispherical reflectance values were used for copper and porous copper powders to calculate the wavelength dependent mixture reflectance was calculated for the mixture (model 1).
2. The theoretically calculated values of copper and porous copper powders using the optical model described above were used to calculate the reflectance values of the mixtures at wavelengths 1.07 μm and 2 μm (model 2).

5.2 Optical characterization of powder mixtures

To address the challenges of doing spectrum measurements with individual single particles, a packed particle bed with a regulated bed thickness was used. The geometry of the windowed is shown in Figure 24, where the particles are practically packed tightly within the gap provided by the spacer ring. The packed particle bed is sandwiched between two windows in the wavelength range of interest that have a high transmittance.

The particle bed reflectance is calculated using a ray-tracing model that takes into consideration the multiple reflections and the effect of the window. For ray-tracing computations, an air gap between the window and the particle bed is considered due to the limited contact area between the particles and the window, as illustrated in Figure 24.

The reflectance of the sample setup or the windowed particle bed is [103]:

$$R_{s,\lambda} = R_{w,\lambda} + T_{w,\lambda}^2 \left(\frac{R_{p,\lambda}}{1 - R_{p,\lambda} R_{w,\lambda}} \right) \quad 5.16$$

where R and T denote the reflectance and transmittance respectively and the subscript λ refers to spectral property. The subscripts p, s, and w stand for particle bed, sample (particle bed with window), and window alone, respectively. The sample reflectance was obtained using the integrating sphere (IS). The radiative characteristics of the windows must be predetermined in order to infer the particle bed reflectance from Eq. 5.16.

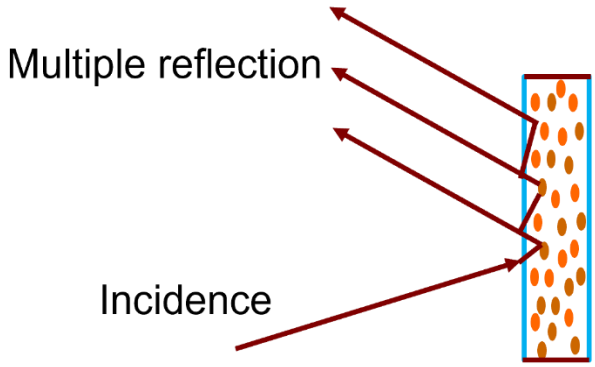

Figure 24: Schematic of a particle bed sandwiched between two transparent window materials, and the ray-tracing diagram of multiple reflections by the window and particle bed (which is thick enough to be opaque).

The optical constants of the window material may be used to determine the window's transmittance and reflectance.

For a slab or plate with a thickness of d, the reflectance and transmittance can be stated as follows:

$$R_\lambda = \rho_\lambda + \left(\frac{\rho_\lambda \tau_\lambda^2 (1-\rho_\lambda)^2}{1-\rho_\lambda^2 \tau_\lambda^2}\right) \quad 5.17$$

$$T_\lambda = \left(\frac{\tau_\lambda^2 (1-\rho_\lambda)^2}{1-\rho_\lambda^2 \tau_\lambda^2}\right) \quad 5.18$$

where ρ_λ is the reflectivity at the interface between air and a semi-infinite window material, and τ_λ is internal transmissivity which can be determined by:

$$\tau_\lambda = e^{-a_\lambda d} \quad 5.19$$

where $a_\lambda = \frac{4\pi\kappa}{\lambda}$ is the absorption coefficient and κ being the extinction coefficient or the imaginary part of the complex refractive index $\underline{n} = n + i\,\kappa$.

The normal incident reflectivity at the interface between air (medium 1) and glass is shown in Figure 25 and can be calculated from Fresnel's coefficient and is expressed:

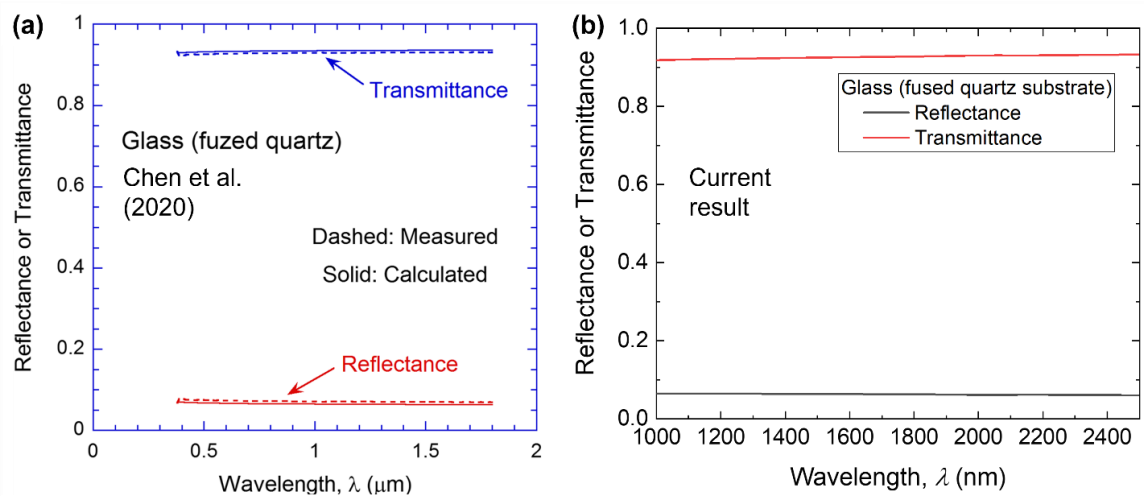

Figure 25: (a) Measured and calculated reflectance and transmittance of glass window from 0.38 μm to 1.8 μm (literature). (b) Calculated reflectance and transmittance of glass window from 1000 nm to 2500 nm using ray tracing model.

$$\rho_\lambda = \left(\frac{(n-1)^2+\kappa^2}{(n+1)^2+\kappa^2}\right) \tag{5.20}$$

The reflectance and transmittance are determined using raytracing model and the particle bed reflectance can be now calculated from Eq. 5.16:

$$R_{p,\lambda} = \frac{1}{R_{w,\lambda} + T_{w,\lambda}^2\left(\frac{1}{R_{s,\lambda}-R_{w,\lambda}}\right)} \tag{5.21}$$

Hemispherical reflectance measurements of powder mixtures were done at room temperature using PerkinElmer UV/Vis integrating sphere to investigate their variation due to different mixing ratios of the copper and porous copper powders. Section 3.3 provides a detailed explanation of the integrating sphere setup and measuring methodologies. The powders were packed in a glass container and mounted on the back port of the IS for the measurements. Figure 26 shows the measured and calculated hemispherical reflectance using eq. 5.20. The copper powders had the maximum reflectance, and the porous copper

powders the least. This is due to the reduced extinction and increased refractive indices of PCu powder compared to the copper powder.

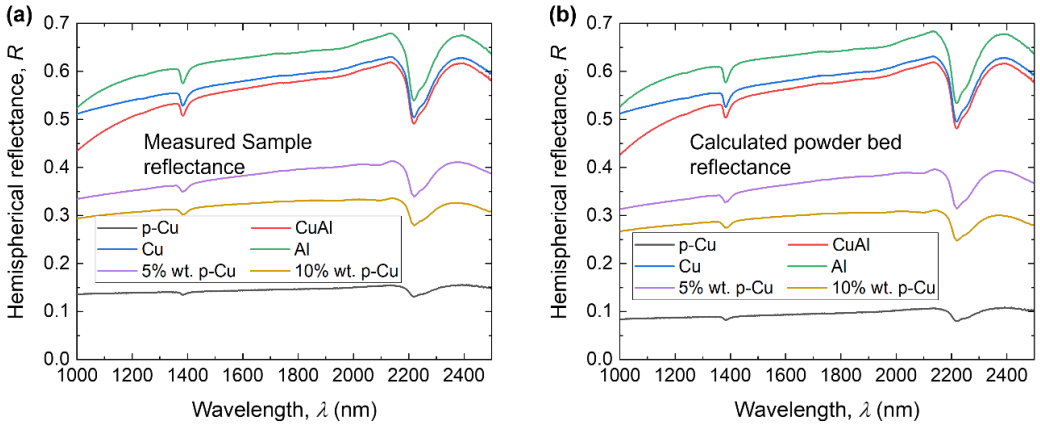

Figure 26: (a) Measured sample hemispherical reflectance of the sample consisting of the powder bed sandwiched between glass slides. (b) Calculated hemispherical reflectance of the powder bed particles from the measured sample reflectance and calculated thick glass.

At 1.07 and 2 μm, the measured and the calculated reflectance of the mixes were compared. The wavelength 1.07 μm was selected to represent the laser light used for 3D printing and 2 μm to check the validity of the model at more than one wavelength. The results are shown in Figure 27. Particle size contribute to the relative surface area as seen from eq. 5.15. It is observed from Figure 27 (a) that PCu powders had larger surface area and hence contributed to majority of the reflectance in powders mixes, despite being present in small weight fractions. The reflectance curves at both the wavelengths as seen from Figure 27 (b) and (c) suggest that the reflectance is more affected by relative surface areas than by compositions. Densities are indications of distances between the particles and particle sizes and hence for better accuracy of the results, the measured apparent densities have been used for the calculations. The error between the experimental and the calculated

values are shown in Figure 27 (d). The error values are lesser than 10 % for weight fraction of PCu up to 10% and the values went as high as 29% for powder mixture which had PCu up to 50% by weight. The possible reasons for the differences observed between the theoretical and experimental reflectance values are: (1) One component may deform more

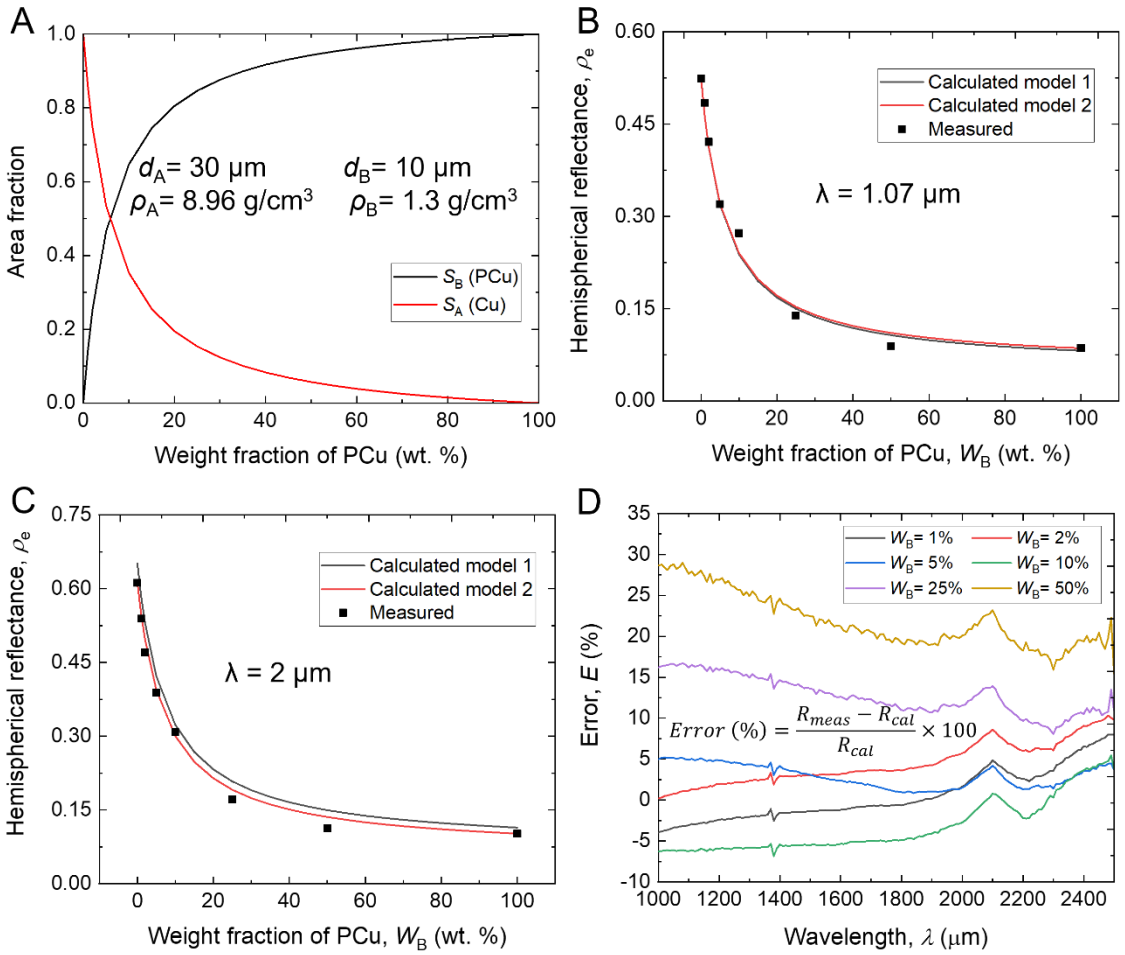

Figure 27: (a) Calculated surface area fractions of copper and porous copper powder particles varying with weight fraction of porous copper calculated using copper (particle A) and porous copper (particle B) measured apparent density values of ρ_A = 8.96 g/cm^3, ρ_A = 1.3 g/cm^3 and diameters d_A=30 µm and d_B=10 µm. The calculated hemispherical reflectance values using model 1 and 2 compared to measured values at wavelength (b) 1.07 µm, and (c) 2 µm. (d) The error percentage between calculated and measured reflectance values using model 1.

under pressure, occupying a little larger surface area than would be predicted, (2) Because the components may have distinct particle shapes, similar particle-size ranges acquired by screening may equate to somewhat different surface areas, and (3) Shrinking of the PCu powder particles after dealloying has been neglected.

The measured and calculated reflectance values were compared further using model 1 described in the Optical Model as shown in Figure 28. Figure 28 (a) shows the hemispherical reflectance measured using an integrating sphere and Figure 28 (b) shows the calculated hemispherical reflectance of the mixtures using the linear or the checkboard model. It is observed that the copper powder had the maximum reflectance value and the porous copper powder, the least, over the entire measured wavelength regime. The mixtures had intermediate values of reflectance between the copper and porous copper powders. The copper powder's reflectance reduced by ~30% by just adding 10% of PCu powder by weight fraction. This suggested that the reflectance depended more on the area fraction of the particles than their weight fractions and hence porous copper contributed heavily to the reflectance values in spite of being present in small quantities.

It was also observed that the difference in between the calculated and measured values reached as high as -50%. This was better understood from Figure 28 (c) where the error is low in most of the wavelength regime except at wavelengths near 2200 nm. Water vapor molecule tends to absorb radiation in this wavelength regime which is seen as a dip in measured reflectance values. This error propagates on to the mixtures and hence the high value of error is observed near this wavelength as seen from Figure 28 (b). Apart from that the error at other wavelengths has values lower than ±20%.

One major assumption of the model is that the photons interact with only one component of the mixture. To further improve the results the non-linear model can be used [97]. This model considers the intimate nature of the components and includes the effect of photons experiencing multiple scattering and hence likely interaction with more than one component of the mixture. The suggested model converts the reflectance spectra to single scattering albedo (SSA) thus accounting for the multiple scattering effects.

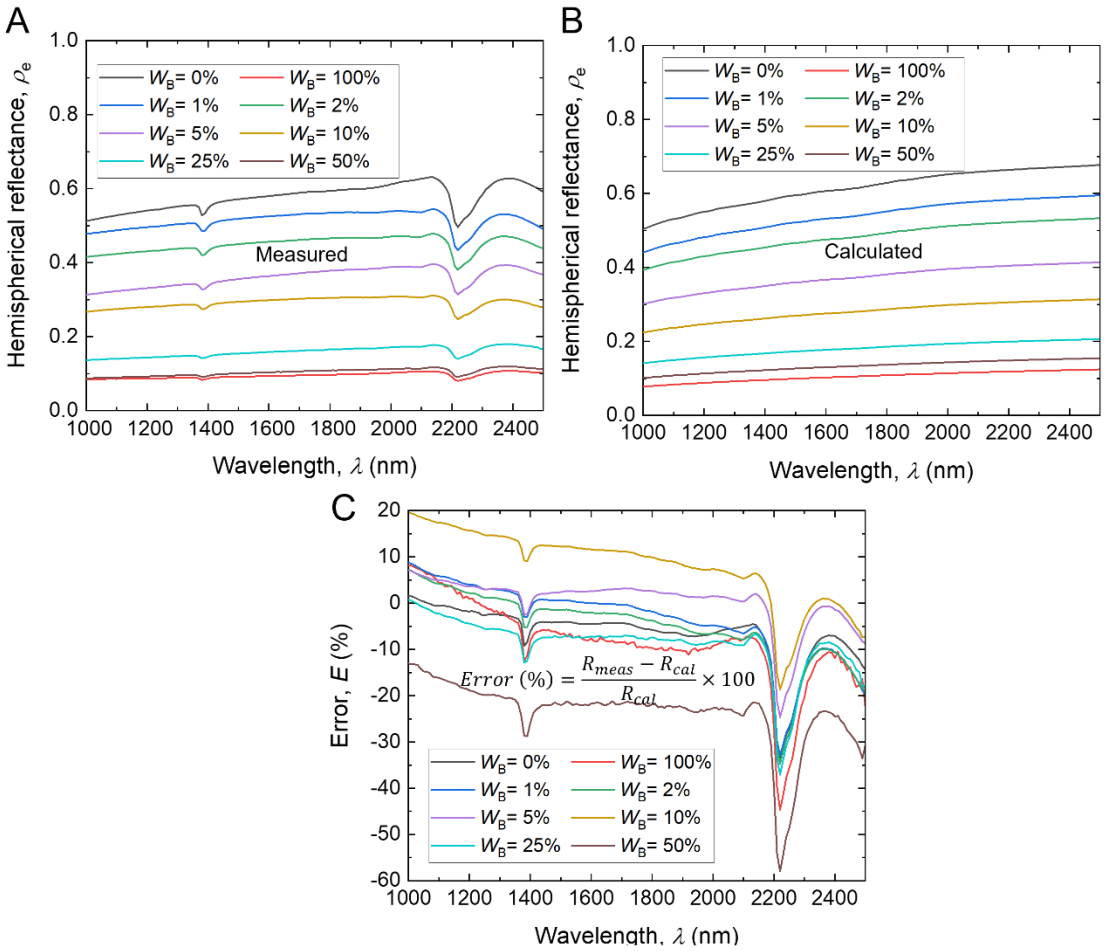

Figure 28: (a) The measured reflectance of mixtures with varying fractions of copper and porous copper powders using an integrating sphere. (b) Calculated reflectance of powder mixtures using the linear or the checkerboard model. (b) The error percentage between calculated and measured reflectance values using model 2.

CHAPTER 6

CONCLUSIONS AND RECOMMENDATIONS

This dissertation has studied the use and characterization of isotropic and uniaxial metamaterials for application in TPV systems, energy-conversion, and 3D printing domain. A theoretical study of an aluminum nanopillar metasurface filter was studied and their application as narrowband optical filters in a TPV system was investigated. The radiative characteristics of the selective filter were explored using FDTD modeling. In comparison with the HFSS results, the FDTD predicted the MP resonance and the transmission peaks with more accuracy and faster computational time. The excitation of MP mode between the nanopillars resulted in the selective transmission at required wavelength. LC circuit model and the EM field distribution was used to explain the underlying physical mechanism. MP resonance could be obtained at desired wavelength by tuning the geometric parameters of nanopillars. The suggested structure's optical property simulation revealed high spectrum selectivity behavior. The suggested AlNP metasurface selective filter combined with a GaSb cell was used to replicate the TPV system performance. At an emitter temperature of 2000 K, the simulated findings suggest a TPV efficiency of 24.1% percent and an output power of 3.67 W/cm^2. When coupled with an ideal cell, the designed filter improved the efficiency of the TPV cell to 31.1%. This study can be further extended by fabricating the samples either using anodized aluminum oxide (AAO) template method described in the APPENDIX A or by photolithography. The fabricated filter can be coupled with the TPV setup and the efficiency can be measured. This study will pave the way for Nanopillar-based spectrally selective filters, as well as the creation of low-cost, high-efficiency TPV devices.

Next, isotropic NPG thin film with varying PVF were successfully fabricated utilizing the Ag-Au thin film co-sputtering and de-alloying techniques. The fabrication conditions such as dealloying time and temperature was carefully correlated with the characterizations of pore diameter and filling ratio. The spectral hemispherical reflectance within the visible and near-infrared region was measured with an integrating sphere at different incidence angles and polarization states, and the experimental data was validated and understood by a simple optical model based on effective medium theory and Fresnel reflections. It was found that for blue light at the short wavelengths, the reflectance of porous gold samples is as low as 0.1 at normal incidence with negligible dependence on pore filling ratio but increases with oblique angles for TE waves. On the other hand, at the longer wavelengths, the reflectance was as high as 0.95 regardless of polarization state due to the large extinction coefficient but decreased significantly with larger pores.

Continuing with the temperature dependent study of NPG thin films showed that the thermal coarsening led to an increase in the surface roughness via an increase in ligament size and, hence, yielded more diffuse and less specular reflectance as confirmed by ex-situ optical characterization. In-situ measurements of specular reflectance yielded a good prediction of ligament size by establishing (i) a theoretical optical model that captured the dependence of ligament size on temperature via an Arrhenius relation, (ii) the scattering coefficient dependence on roughness and (iii) a linear model for roughness dependence on ligament size. By merging these contributions into a single model, a good agreement of theoretical and experimental relative specular reflectance is obtained up to 500 °C. Further near-field radiation measurements setup can be developed to measure the heat flux between NPG thin films as an extension to this study. Monitoring of ligament size via the fiber-

optical sensors described in this paper could have an impact in (i) microelectronics sensors based on nanoporous gold such as SERS substrates for biosensing [104], (ii) the design of nanostructured absorbers for thermophotovoltaics, and (iii) its manufacturing process for attaining close-loop control of ligament size during its synthesis since fiber-optic sensors directly probe and monitor the NPG's ligament size.

Finally, experimental hemispherical reflectance measurements using integrating sphere and theoretical analysis based on RTE and checkerboard method were successfully performed on copper and porous copper powders used for 3D printing. The results from the hemispherical reflectance measurements and optical model concluded that the porous copper powder bed had lower reflectance than the solid. The optical model further showed that the reflectance of the mixtures was a function of the individual component surface area fractions. The surface area fraction was calculated for the individual component with the help of their density, average diameter of the powder particles and weight fraction values. The mixtures containing different proportions of solid and porous copper powders had intermediate reflectance values between the solid and porous copper powders. As an extension to this work, ray tracing optics model can be developed to simulate the radiative properties of powder mixtures. Defining the absorptance in the preliminary powders paves a way in the controllability of optical properties of the end state products produced via 3D printing. These results put a step forward in the scalability of large end products suggesting a path for 3D printed absorber sheets and tubes.

REFERENCES

[1] M. M. A. Gamel *et al.*, *A review on thermophotovoltaic cell and its applications in energy conversion: Issues and recommendations*, vol. 14, no. 17. 2021.

[2] C. Ferrari, F. Melino, M. Pinelli, P. R. Spina, and M. Venturini, "Overview and status of thermophotovoltaic systems," *Energy Procedia*, vol. 45. pp. 160–169, 2014, doi: 10.1016/j.egypro.2014.01.018.

[3] L. P. Wang and Z. M. Zhang, "Wavelength-selective and diffuse emitter enhanced by magnetic polaritons for thermophotovoltaics," *Appl. Phys. Lett.*, vol. 100, no. 6, pp. 2010–2013, 2012, doi: 10.1063/1.3684874.

[4] L. Mao *et al.*, "New development of one-dimensional Si/SiO2 photonic crystals filter for thermophotovoltaic applications," *Renew. Energy*, vol. 97, no. 1, pp. 245–250, 2012, doi: 10.1016/j.renene.2012.03.001.

[5] J. Li, F. Zhao, and W.-C. Shih, "Direct-write patterning of nanoporous gold microstructures by in situ laser-assisted dealloying," *Opt. Express*, vol. 24, no. 20, p. 23610, 2016, doi: 10.1364/oe.24.023610.

[6] S. Basu, Y.-B. Chen, and Z. Zhang, "Microscale radiation in thermophotovoltaic devices—a review," *Int. J. Energy Res.*, vol. 31, no. 6–7, pp. 689--716, 2007, doi: 10.1002/er.

[7] D. Wilt, D. Chubb, D. Wolford, P. Magari, and C. Crowley, "Thermophotovoltaics for space power applications," *AIP Conf. Proc.*, vol. 890, no. March 2007, pp. 335–345, 2007, doi: 10.1063/1.2711751.

[8] L. Fraas, R. Ballantyne, J. Samaras, and M. Seal, "Electric power production using new GaSb photovoltaic cells with extended infrared response," vol. 44, no. 1995, pp. 44–53, 2008, doi: 10.1063/1.47053.

[9] A. Datas, A. Ramos, A. Martí, C. del Cañizo, and A. Luque, "Ultra high temperature latent heat energy storage and thermophotovoltaic energy conversion," *Energy*, vol. 107. pp. 542–549, 2016, doi: 10.1016/j.energy.2016.04.048.

[10] T. Bauer, I. Forbes, and N. Pearsall, "The potential of thermophotovoltaic heat recovery for the UK industry," *Int. J. Ambient Energy*, vol. 25, no. 1, pp. 19–25, 2004, doi: 10.1080/01430750.2004.9674933.

[11] Y. Xuan, X. Chen, and Y. Han, "Design and analysis of solar thermophotovoltaic systems," *Renew. Energy*, vol. 36, no. 1, pp. 374–387, 2011, doi: 10.1016/j.renene.2010.06.050.

[12] W. R. Chan, V. Stelmakh, C. M. Waits, M. Soljacic, J. D. Joannopoulos, and I.

Celanovic, “Photonic Crystal Enabled Thermophotovoltaics for a Portable Microgenerator,” *J. Phys. Conf. Ser.*, vol. 660, no. 1, 2015, doi: 10.1088/1742-6596/660/1/012069.

[13] T. Burger, C. Sempere, B. Roy-layinde, and A. Lenert, “Review Present Efficiencies and Future Opportunities in Thermophotovoltaics,” *Joule*, vol. 4, no. 8, pp. 1660–1680, 2020, doi: 10.1016/j.joule.2020.06.021.

[14] L. M. Fraas, “Economic potential for thermophotovoltaic electric power generation in the steel industry,” in *2014 IEEE 40th Photovoltaic Specialist Conference (PVSC)*, 2014, pp. 766–770.

[15] M. Tan *et al.*, “Investigation of InGaAs thermophotovoltaic cells under blackbody radiation,” *Appl. Phys. Express*, vol. 7, no. 9, pp. 4–7, 2014, doi: 10.7567/APEX.7.096601.

[16] T. C. Narayan *et al.*, “World record demonstration of > 30% thermophotovoltaic conversion efficiency,” *Conf. Rec. IEEE Photovolt. Spec. Conf.*, vol. 2020-June, no. 1906, pp. 1792–1795, 2020, doi: 10.1109/PVSC45281.2020.9300768.

[17] A. LaPotin *et al.*, “Thermophotovoltaic efficiency of 40%,” *Nature*, vol. 604, no. 7905, pp. 287–291, 2022, doi: 10.1038/s41586-022-04473-y.

[18] Z. Utlu and B. S. Önal, “Thermodynamic analysis of thermophotovoltaic systems used in waste heat recovery systems: an application,” *Int. J. Low-Carbon Technol.*, vol. 13, no. 1, pp. 52–60, 2018.

[19] F. Bendelala, A. Cheknane, and H. Hilal, “Enhanced low-gap thermophotovoltaic cell efficiency for a wide temperature range based on a selective meta-material emitter,” *Sol. Energy*, vol. 174, pp. 1053–1057, 2018.

[20] B. Zhao, K. Chen, S. Buddhiraju, G. Bhatt, M. Lipson, and S. Fan, “High-performance near-field thermophotovoltaics for waste heat recovery,” *Nano Energy*, vol. 41, no. August, pp. 344–350, 2017, doi: 10.1016/j.nanoen.2017.09.054.

[21] S. Chakraborty, R. Ghosh, and A. Chatterjee, “ A high temperature optical filter using Si/Si 3 N 4 one dimensional photonic crystal for GaSb thermophotovoltaic applications ,” *Am. J. Electron. Commun.*, vol. 2, no. 2, pp. 19–22, 2021, doi: 10.15864/ajec.2205.

[22] G. Mirbagheri and D. T. Crouse, “Design , fabrication , and spectral characterization of TM-polarized metamaterials-based narrowband infrared filter,” 2022.

[23] A. Pirvaram, N. Talebzadeh, M. Rostami, S. N. Leung, and P. G. O’Brien, “Evaluation of a ZrO2/ZrO2-aerogel one-dimensional photonic crystal as an

optical filter for thermophotovoltaic applications," *Therm. Sci. Eng. Prog.*, vol. 25, no. February, 2021, doi: 10.1016/j.tsep.2021.100968.

[24] D. L. Chubb and B. S. Good, "A combined thermophotovoltaic-thermoelectric energy converter," *Sol. Energy*, vol. 159, pp. 760–767, 2018.

[25] T. Bryce C, S. Stephen A, and E. P. Luther, "Nanoporous metal foams," *Angewandte Chemie - International Edition*, vol. 49, no. 27. pp. 4544–4565, Jun. 21, 2010, doi: 10.1002/anie.200902994.

[26] C. Xu *et al.*, "Low temperature CO oxidation over unsupported nanoporous gold," *J. Am. Chem. Soc.*, vol. 129, no. 1, pp. 42–43, Jan. 2007, doi: 10.1021/ja0675503.

[27] and C.-F. M. Van Noort, Danny, "Porous Gold Surfaces for Biosensor Applications," *Biosens. Bioelectron.*, vol. 15, no. 3–4, pp. 203–209, 2000.

[28] Y. Ding and M. Chen, "Nanoporous metals for catalytic and optical applications," *MRS Bull.*, vol. 34, no. 8, pp. 569–576, 2009, doi: 10.1557/mrs2009.156.

[29] A. Wittstock, J. Biener, and M. Bäumer, "Nanoporous gold: A new material for catalytic and sensor applications," *Phys. Chem. Chem. Phys.*, vol. 12, no. 40, pp. 12919–12930, Oct. 2010, doi: 10.1039/c0cp00757a.

[30] S. O. Kucheyev, J. R. Hayes, J. Biener, T. Huser, C. E. Talley, and A. V. Hamza, "Surface-enhanced Raman scattering on nanoporous Au," *Appl. Phys. Lett.*, vol. 89, no. 5, 2006, doi: 10.1063/1.2260828.

[31] L. H. Qian, X. Q. Yan, T. Fujita, A. Inoue, and M. W. Chen, "Surface enhanced Raman scattering of nanoporous gold: Smaller pore sizes stronger enhancements," *Appl. Phys. Lett.*, vol. 90, no. 15, 2007, doi: 10.1063/1.2722199.

[32] D. Jalas *et al.*, "Effective medium model for the spectral properties of nanoporous gold in the visible," *Appl. Phys. Lett.*, vol. 105, no. 24, Dec. 2014, doi: 10.1063/1.4904714.

[33] A. I. Maaroof, M. B. Cortie, and G. B. Smith, "Optical properties of mesoporous gold films," *J. Opt. A Pure Appl. Opt.*, vol. 7, no. 7, pp. 303–309, Jul. 2005, doi: 10.1088/1464-4258/7/7/007.

[34] J. Biener, G. W. Nyce, A. M. Hodge, M. M. Biener, A. V. Hamza, and S. A. Maier, "Nanoporous plasmonic metamaterials," *Adv. Mater.*, vol. 20, no. 6, pp. 1211–1217, Mar. 2008, doi: 10.1002/adma.200701899.

[35] M. C. Dixon, T. A. Daniel, M. Hieda, D. M. Smilgies, M. H. W. Chan, and D. L. Allara, "Preparation, structure, and optical properties of nanoporous gold thin films," *Langmuir*, vol. 23, no. 5, pp. 2414–2422, Feb. 2007, doi: 10.1021/la062313z.

[36] Y. Lu, Q. Wang, J. Sun, and J. Shen, “Selective dissolution of the silver component in colloidal Au and Ag multilayers: A facile way to prepare nanoporous gold film materials,” *Langmuir*, vol. 21, no. 11, pp. 5179–5184, May 2005, doi: 10.1021/la0500878.

[37] M. Haupt *et al.*, “Nanoporous gold films created using templates formed from self-assembled structures of inorganic-block copolymer micelles,” *Adv. Mater.*, vol. 15, no. 10, pp. 829–831, May 2003, doi: 10.1002/adma.200304688.

[38] N. Jia, L. Cao, and Z. Wang, “Platinum-coated gold nanoporous film surface: Electrodeposition and enhanced electrocatalytic activity for methanol oxidation,” *Langmuir*, vol. 24, no. 11, pp. 5932–5936, Jun. 2008, doi: 10.1021/la800163f.

[39] Y. Li, Y.-Y. Song, C. Yang, and X.-H. Xia, “Hydrogen bubble dynamic template synthesis of porous gold for nonenzymatic electrochemical detection of glucose,” *Electrochem. commun.*, vol. 9, no. 5, pp. 981–988, May 2007, doi: 10.1016/J.ELECOM.2006.11.035.

[40] M. Schwartzkopf *et al.*, “From atoms to layers: In situ gold cluster growth kinetics during sputter deposition,” *Nanoscale*, vol. 5, no. 11, pp. 5053–5062, Jun. 2013, doi: 10.1039/c3nr34216f.

[41] R. Zhang, M. Hummelgard, and H. Olin, “Size and concentration controlled growth of porous gold nanofilm,” *Phys. Status Solidi Appl. Mater. Sci.*, vol. 209, no. 3, pp. 519–523, 2012, doi: 10.1002/pssa.201127405.

[42] M. Al-Hussein *et al.*, “In situ X-ray study of the structural evolution of gold nano-domains by spray deposition on thin conductive P3HT films,” *Langmuir*, vol. 29, no. 8, pp. 2490–2497, Feb. 2013, doi: 10.1021/la3048483.

[43] G. W. Nyce, J. R. Hayes, A. V. Hamza, and J. H. Satcher, “Synthesis and characterization of hierarchical porous gold materials,” *Chem. Mater.*, vol. 19, no. 3, pp. 344–346, Feb. 2007, doi: 10.1021/cm062569q.

[44] I. McCue, J. Stuckner, M. Murayama, and M. J. Demkowicz, “Gaining new insights into nanoporous gold by mining and analysis of published images,” *Sci. Rep.*, vol. 8, no. 1, Dec. 2018, doi: 10.1038/s41598-018-25122-3.

[45] J. Weissmüller and K. Sieradzki, “Dealloyed nanoporous materials with interface-controlled behavior,” *MRS Bull.*, vol. 43, no. 1, pp. 14–19, Jan. 2018, doi: 10.1557/mrs.2017.299.

[46] P. T. Shen, Y. Sivan, C. W. Lin, H. L. Liu, C. Chang, and S. W. Chu, “Temperature- and -roughness dependent permittivity of annealed / unannealed gold films,” *Opt. Express*, vol. 24, no. 17, pp. 19254–19263, 2016.

[47] S. R. Pogson, P. Fox, C. J. Sutcliffe, and W. O’neill, “The production of copper

parts using DMLR," *Rapid Prototyp. J.*, 2003.

[48] V. Lindström *et al.*, "Laser powder bed fusion of metal coated copper powders," *Materials (Basel).*, vol. 13, no. 16, p. 3493, 2020.

[49] T. Q. Tran *et al.*, "3D printing of highly pure copper," *Metals (Basel).*, vol. 9, no. 7, p. 756, 2019.

[50] D. Tiberto, U. E. Klotz, F. Held, and G. Wolf, "Additive manufacturing of copper alloys: influence of process parameters and alloying elements," *Mater. Sci. Technol.*, vol. 35, no. 8, pp. 969–977, 2019.

[51] H. Siva Prasad, F. Brueckner, J. Volpp, and A. F. H. Kaplan, "Laser metal deposition of copper on diverse metals using green laser sources," *Int. J. Adv. Manuf. Technol.*, vol. 107, no. 3, pp. 1559–1568, 2020.

[52] C. Silbernagel, L. Gargalis, I. Ashcroft, R. Hague, M. Galea, and P. Dickens, "Electrical resistivity of pure copper processed by medium-powered laser powder bed fusion additive manufacturing for use in electromagnetic applications," *Addit. Manuf.*, vol. 29, p. 100831, 2019.

[53] M. Colopi, L. Caprio, A. G. Demir, and B. Previtali, "Selective laser melting of pure Cu with a 1 kW single mode fiber laser," *Procedia Cirp*, vol. 74, pp. 59–63, 2018.

[54] S. D. Jadhav, J. Vleugels, J. Kruth, J. Van Humbeeck, and K. Vanmeensel, "Mechanical and electrical properties of selective laser-melted parts produced from surface-oxidized copper powder," *Mater. Des. Process. Commun.*, vol. 2, no. 2, p. e94, 2020.

[55] S. D. Jadhav *et al.*, "Influence of carbon nanoparticle addition (and impurities) on selective laser melting of pure copper," *Materials (Basel).*, vol. 12, no. 15, p. 2469, 2019.

[56] L. Wang, "Spectral Control of Thermal Radiation by Excitation of Magnetic Polaritons," in *Annual Review of Heat Transfer*, vol. 23, V. Prasad, Y. Jaluria, and Z. Zhang, Eds. New York: Begel House Inc., 2020, pp. 167–197.

[57] L. P. Wang and Z. M. Zhang, "Measurement of coherent thermal emission due to magnetic polaritons in subwavelength microstructures," *J. Heat Transfer*, vol. 135, no. 9, pp. 1–9, 2013, doi: 10.1115/1.4024469.

[58] L. Wang, A. Haider, and Z. Zhang, "Effect of magnetic polaritons on the radiative properties of inclined plate arrays," *J. Quant. Spectrosc. Radiat. Transf.*, vol. 132, pp. 52–60, 2014, doi: 10.1016/j.jqsrt.2012.09.010.

[59] L. Zhang, X. Lang, A. Hirata, and M. Chen, "Wrinkled Nanoporous Gold Films

with," *ACS Nano*, vol. 5, no. 6, pp. 4407–4413, 2011, [Online]. Available: http://www.ncbi.nlm.nih.gov/pubmed/21705826.

[60] T. R. Jr, J. Lazo-Wasem, and E. Gratrix, "Front Surface Tandem Filters using Sapphire (Al2O3) Substrates for Spectral Control in Thermophotovoltaic Energy Conversion Systems," 2005, [Online]. Available: http://www.rugate.com/Front Surface Tandem Filters Using Sapphire.pdf.

[61] S. G. Babiker, Y. Shuai, M. O. Sid-Ahmed, and M. Xie, "Design of a one - Dimensional Si/SiO2 photonic crystals filter for thermophotovoltaic application," *2013 16th Int. Multi Top. Conf. INMIC 2013*, vol. 9, pp. 177–181, 2013, doi: 10.1109/INMIC.2013.6731346.

[62] G. Meng *et al.*, "Facile and scalable patterning of sublithographic scale uniform nanowires by ultra-thin AAO free-standing membrane," *RSC Adv.*, vol. 2, no. 28, pp. 10618–10623, 2012, doi: 10.1039/c2ra21643d.

[63] C. Zhao *et al.*, "Growth of vertically aligned ZnO nanowire arrays on ZnO single crystals," *Materials Letters*, vol. 154. pp. 40–43, 2015, doi: 10.1016/j.matlet.2015.04.053.

[64] Z. H. Wu, X. Y. Mei, D. Kim, M. Blumin, and H. E. Ruda, "Growth of Au-catalyzed ordered GaAs nanowire arrays by molecular-beam epitaxy," *Appl. Phys. Lett.*, vol. 81, no. 27, pp. 5177–5179, 2002, doi: 10.1063/1.1532772.

[65] J. Y. Chang, H. Wang, and L. Wang, "Tungsten Nanowire Metamaterials as Selective Solar Thermal Absorbers by Excitation of Magnetic Polaritons," *J. Heat Transfer*, vol. 139, no. 5, pp. 1–8, 2017, doi: 10.1115/1.4034845.

[66] Q. Ni, H. Alshehri, Y. Yang, H. Ye, and L. Wang, "Plasmonic light trapping for enhanced light absorption in film-coupled ultrathin metamaterial thermophotovoltaic cells," *Front. Energy*, vol. 12, no. 1, pp. 185–194, 2018, doi: 10.1007/s11708-018-0522-x.

[67] K. Park and W. P. King, "Performance analysis of near-field thermophotovoltaic devices considering absorption distribution," in *RADIATIVE TRANSFER-V. Proceedings of the Fifth International Symposium on Radiative Transfer*, 2007.

[68] K. Park, S. Basu, W. P. King, and Z. M. Zhang, "Performance analysis of near-field thermophotovoltaic devices considering absorption distribution," vol. 109, pp. 305–316, 2008, doi: 10.1016/j.jqsrt.2007.08.022.

[69] J. K. Tong, W. C. Hsu, Y. Huang, S. V. Boriskina, and G. Chen, "Thin-film 'thermal well' emitters and absorbers for high-efficiency thermophotovoltaics," *Sci. Rep.*, vol. 5, pp. 1–12, 2015, doi: 10.1038/srep10661.

[70] L. Tang, H. Ye, and J. Xu, "A novel zinc diffusion process for the fabrication of

high-performance GaSb thermophotovoltaic cells," *Sol. Energy Mater. Sol. Cells*, vol. 122, pp. 94–98, 2014, doi: 10.1016/j.solmat.2013.11.027.

[71] T. L. Bergman, T. L. Bergman, F. P. Incropera, D. P. Dewitt, and A. S. Lavine, *Fundamentals of heat and mass transfer*. John Wiley & Sons, 2011.

[72] R. Bhatt, I. Kravchenko, and M. Gupta, "High-efficiency solar thermophotovoltaic system using a nanostructure-based selective emitter," *Sol. Energy*, vol. 197, pp. 538–545, 2020.

[73] R. Bhatt and M. Gupta, "Design and validation of a high-efficiency planar solar thermophotovoltaic system using a spectrally selective emitter," *Opt. Express*, vol. 28, no. 15, pp. 21869–21890, 2020.

[74] A. Kohiyama, M. Shimizu, K. Konno, T. Furuhashi, and H. Yugami, "Effective photon recycling in solar thermophotovoltaics using a confined cuboid emitter," *Opt. Express*, vol. 28, no. 26, pp. 38567–38578, 2020.

[75] J. Stuckner, K. Frei, I. McCue, M. J. Demkowicz, and M. Murayama, "AQUAMI: An open source Python package and GUI for the automatic quantitative analysis of morphologically complex multiphase materials," *Comput. Mater. Sci.*, vol. 139, pp. 320–329, Nov. 2017, doi: 10.1016/J.COMMATSCI.2017.08.012.

[76] A. A. El Mel *et al.*, "Unusual dealloying effect in gold/copper alloy thin films: The role of defects and column boundaries in the formation of nanoporous gold," *ACS Appl. Mater. Interfaces*, vol. 7, no. 4, pp. 2310–2321, 2015, doi: 10.1021/am5065816.

[77] A. Chauvin, L. Horak, E. Duverger-Nédellec, M. Dopita, P. Y. Tessier, and A. A. El Mel, "Effect of the substrate temperature during gold-copper alloys thin film deposition by magnetron co-sputtering on the dealloying process," *Surf. Coatings Technol.*, vol. 383, no. December 2019, 2020, doi: 10.1016/j.surfcoat.2019.125220.

[78] L. H. Qian and M. W. Chen, "Ultrafine nanoporous gold by low-temperature dealloying and kinetics of nanopore formation," *Appl. Phys. Lett.*, vol. 91, no. 8, 2007, doi: 10.1063/1.2773757.

[79] S. Parida, D. Kramer, C. A. Volkert, H. Rösner, J. Erlebacher, and J. Weissmüller, "Volume change during the formation of nanoporous gold by dealloying," *Phys. Rev. Lett.*, vol. 97, no. 3, pp. 4–7, 2006, doi: 10.1103/PhysRevLett.97.035504.

[80] E. D. Palik, *Handbook of Optical Constants of Solids*. Academic Press, 1998.

[81] X. L. Liu, L. P. Wang, and Z. M. Zhang, "Wideband tunable omnidirectional infrared absorbers based on doped-silicon nanowire arrays," *J. Heat Transfer*, vol. 135, no. 6, pp. 1–8, 2013, doi: 10.1115/1.4023578.

[82] H. Wang, X. Liu, L. Wang, and Z. Zhang, “Anisotropic optical properties of silicon nanowire arrays based on the effective medium approximation,” *Int. J. Therm. Sci.*, vol. 65, pp. 62–69, Mar. 2013, doi: 10.1016/j.ijthermalsci.2012.08.018.

[83] R. W. Johnson, P. B. and Christy, “Optical Constants of the Noble Metals,” *Phys. Rev. B*, vol. 6, no. 12, pp. 4370--4379, 1972, doi: 10.1103/PhysRevB.6.4370.

[84] Z. Zhang, *Nano Microscale Heat Transfer*. New York, NY : McGraw-Hill, 2007.

[85] C. Louis and O. Pluchery, *Gold Nanoparticles for Physics, Chemistry and Biology*. IMPERIAL COLLEGE PRESS, 2012.

[86] R. N. Viswanath, V. A. Chirayath, R. Rajaraman, G. Amarendra, and C. S. Sundar, “Ligament coarsening in nanoporous gold: Insights from positron annihilation study,” *Appl. Phys. Lett.*, vol. 102, no. 25, Jun. 2013, doi: 10.1063/1.4812290.

[87] C. Herring, “Effect of change of scale on sintering phenomena,” *J. Appl. Phys.*, vol. 21, no. 4, pp. 301–303, 1950, doi: 10.1063/1.1699658.

[88] M. Hakamada and M. Mabuchi, “Thermal coarsening of nanoporous gold: Melting or recrystallization,” *J. Mater. Res.*, vol. 24, no. 2, pp. 301–304, 2009, doi: 10.1557/jmr.2009.0037.

[89] A. A. El-Zoka, J. Y. Howe, R. C. Newman, and D. D. Perovic, “In situ STEM/SEM study of the coarsening of nanoporous gold,” *Acta Mater.*, vol. 162, pp. 67–77, 2019, doi: 10.1016/j.actamat.2018.09.002.

[90] P. B. Johnson and R.-Wjp. Christy, “Optical constants of the noble metals,” *Phys. Rev. B*, vol. 6, no. 12, p. 4370, 1972.

[91] D. Garoli *et al.*, “Fractal-Like Plasmonic Metamaterial with a Tailorable Plasma Frequency in the near-Infrared,” *ACS Photonics*, vol. 5, no. 8, pp. 3408–3414, 2018, doi: 10.1021/acsphotonics.8b00676.

[92] J. M. Vaughan, “The fabry-perot interferometer: History, Theory,” *Pract. Appl.*, p. 583, 1989.

[93] N. A. Gjostein, *Surfaces and Interfaces I. Chemical and Physical Characteristics*. Syracuse University Press, 1967.

[94] A. Y. Chen, S. S. Shi, Y. D. Qiu, X. F. Xie, J. F. Gu, and D. Pan, “Pore-size tuning and optical performances of nanoporous gold films,” *Microporous Mesoporous Mater.*, vol. 202, no. C, pp. 50–56, 2015.

[95] A. V Gusarov, E. H. Bentefour, M. Rombouts, L. Froyen, C. Glorieux, and J.-P. Kruth, “Normal-directional and normal-hemispherical reflectances of micron-and

submicron-sized powder beds at 633 and 790 nm," *J. Appl. Phys.*, vol. 99, no. 11, p. 113528, 2006.

[96] A. V. Gusarov and J. P. Kruth, "Modelling of radiation transfer in metallic powders at laser treatment," *International Journal of Heat and Mass Transfer*, vol. 48, no. 16. pp. 3423–3434, 2005, doi: 10.1016/j.ijheatmasstransfer.2005.01.044.

[97] K. M. Stack and R. E. Milliken, "Modeling near-infrared reflectance spectra of clay and sulfate mixtures and implications for Mars," *Icarus*, vol. 250, pp. 332–356, 2015.

[98] M. R. Querry, "Optical constants," Missouri Univ-Kansas City, 1985.

[99] A. V. Gusarov, E. H. Bentefour, M. Rombouts, L. Froyen, C. Glorieux, and J. P. Kruth, "Normal-directional and normal-hemispherical reflectances of micron- and submicron-sized powder beds at 633 and 790 nm," *J. Appl. Phys.*, vol. 99, no. 11, 2006, doi: 10.1063/1.2205358.

[100] J. R. Howell, M. P. Mengüç, K. Daun, and R. Siegel, *Thermal radiation heat transfer*. CRC press, 2020.

[101] A. V. Gusarov, I. Yadroitsev, P. Bertrand, and I. Smurov, "Model of radiation and heat transfer in laser-powder interaction zone at selective laser melting," *J. Heat Transfer*, vol. 131, no. 7, pp. 1–10, 2009, doi: 10.1115/1.3109245.

[102] E. A. Schatz, "Reflectance of Compacted Powder Mixtures," *J. Opt. Soc. Am.*, vol. 57, no. 7, p. 941, 1967, doi: 10.1364/josa.57.000941.

[103] C. Chen, C. Yang, D. Ranjan, P. G. Loutzenhiser, and Z. M. Zhang, "Spectral radiative properties of ceramic particles for concentrated solar thermal energy storage applications," *Int. J. Thermophys.*, vol. 41, no. 11, pp. 1–25, 2020.

[104] D. Garoli *et al.*, "Nanoporous gold leaves: preparation, optical characterization and plasmonic behavior in the visible and mid-infrared spectral regions," *Opt. Mater. Express*, vol. 5, no. 10, p. 2246, 2015, doi: 10.1364/ome.5.002246.

[105] Q. Ni, R. Ramesh, C.-A. Chen, and L. Wang, "Semiconductor-based selective emitter with a sharp cutoff for thermophotovoltaic energy conversion," *Opt. Lett.*, vol. 46, no. 13, pp. 3163–3166, 2021.

[106] S. Adachi, "Optical dispersion relations for GaP, GaAs, GaSb, InP, InAs, InSb, Al x Ga1− x As, and In1− x Ga x As y P1− y," *J. Appl. Phys.*, vol. 66, no. 12, pp. 6030–6040, 1989.

[107] W. Lee and S. J. Park, "Porous anodic aluminum oxide: Anodization and templated synthesis of functional nanostructures," *Chem. Rev.*, vol. 114, no. 15, pp. 7487–7556, 2014, doi: 10.1021/cr500002z.

[108] Y. Lei and W. K. Chim, “Shape and size control of regularly arrayed nanodots fabricated using ultrathin alumina masks,” *Chem. Mater.*, vol. 17, no. 3, pp. 580–585, 2005, doi: 10.1021/cm048609c.

[109] Y. Lei, K. S. Yeong, J. T. L. Thong, and W. K. Chim, “Large-scale ordered carbon nanotube arrays initiated from highly ordered catalyst arrays on silicon substrates,” *Chem. Mater.*, vol. 16, no. 14, pp. 2757–2761, 2004, doi: 10.1021/cm049588p.

[110] H. Reddy, U. Guler, A. Kidishev, and V. M. Shalaev, “Temperature-dependent optical properties of gold thin films,” *Opt. Mater. Express*, vol. 6, no. 9, pp. 2776–2802, 2016.

APPENDIX A

OPTICAL FILTER

FDTD validation

For simulating nano-scale optical systems, the Finite-Difference Time-Domain (FDTD) approach provides a rigorous and powerful tool. The maximal problem size is limited solely by the computational power available, as FDTD solves Maxwell's equations directly without any physical approximation. The FDTD approach solves Maxwell's equations on a mesh and computes *E* and *H* at grid points spaced Δx, Δy, and Δz away in all three spatial dimensions, with E and H interlaced. Scattering, transmission, reflection, absorption, and other effects are included in FDTD. To validate the FDTD simulations in the paper, we reproduced the results of spectral emittance varying with nanowire height obtained in literature [65] as shown in Figure 29.

The following steps were followed in the Lumerical FDTD software run the simulations:

1. The simulation region was set to required dimensions and the injection direction was set be the positive *X* direction
2. The *Y* and the *Z* dimensions were set to match the periodicity
3. Next under mesh settings the mesh size (Δ*X*, Δ*Y*, and Δ*Z*) were selected to be 5 nm.
4. To check the convergence, the mesh sizes were made finer 3 and 4nm and the results were compared.
5. It was required for the light to propagate in the *X* direction to infinity and hence perfectly matched layer (PML) boundary was assigned.
6. Periodic boundary conditions were assigned in both *Y* and *Z* directions
7. Plane wave light source with Bloch/ Periodic conditions was created

8. Finally, the required geometry and the power monitors were created at required locations to get the transmittance and the reflectance of the structure.

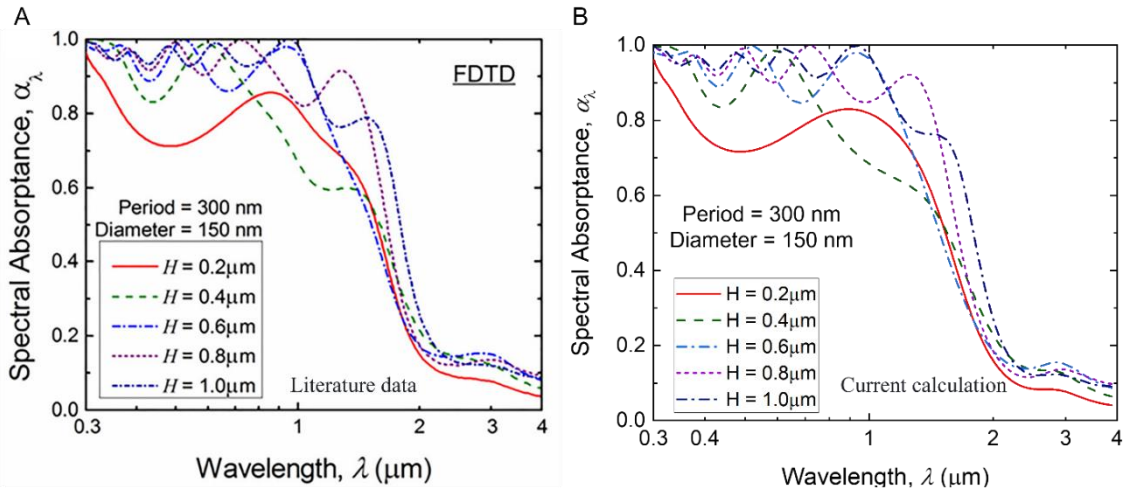

Figure 29: The spectral absorptance of the selective absorber varying with nanowire height based on FDTD simulation from (a) literature and (b) current modeling.

Raytracing optics incorporated with FDTD and comparison with HFSS

To compare the results obtained from FDTD, simulations was performed in ANSYS HFSS using interpolated frequency sweep. Frequency dependent material properties were obtained from Palik data and inputted into Ansys for aluminum and glass. Incident plane wave with frequency ranging from 150 THz to 750 THz corresponding to wavelengths of 0.4 μm to 2 μm. Radiation boundary conditions are applied to the top and bottom surfaces of the air volume and master/slave boundary conditions to the volume surrounding unit cell of the peridoic structure. The delta-S parameter is the difference between the magnitude of the S11 parameters of the initial mesh and the refined mesh, at each frequency was made the criterion of convergence. Maximum delta-S of 0.001 was

used for a minimum of twenty consecutive converged mesh refinement passes to check the convergence. The solution frequency was set to be at 175 THz of the frequency sweep corresponding to ~1.78 μm. Simulated spectral reflectance of the AlNPs on quartz substrate. The Nanopillars array is formed on glass substrate of thickness 0.2 μm. The structure's reflectance and transmittance is obtained by squaring the magnitude pf the S_{11} and S_{21} parameter that represents the amount of incident light being reflected and transmittae by the structure. Ray tracing optics was used to calculate the final reflectance and transmittance of the structure inorder to consider the entire thickness of the substrate. Radiative properties of thin coatings on a substrate is done for variety of reasons: to eliminate transmission of ultraviolet radiation, to increase or decrease transmission over certain spectral regions. The substrate is usually thick enough to be considered incoherent while being semi-transparent for energy transfer consideration.

The result from HFSS is compared to the FDTD as shown in Figure 30. Both the numerical methods predict the transmission peaks due to MP. For the base geometry, the resonance wavelength values are differed between the numerical simulations.

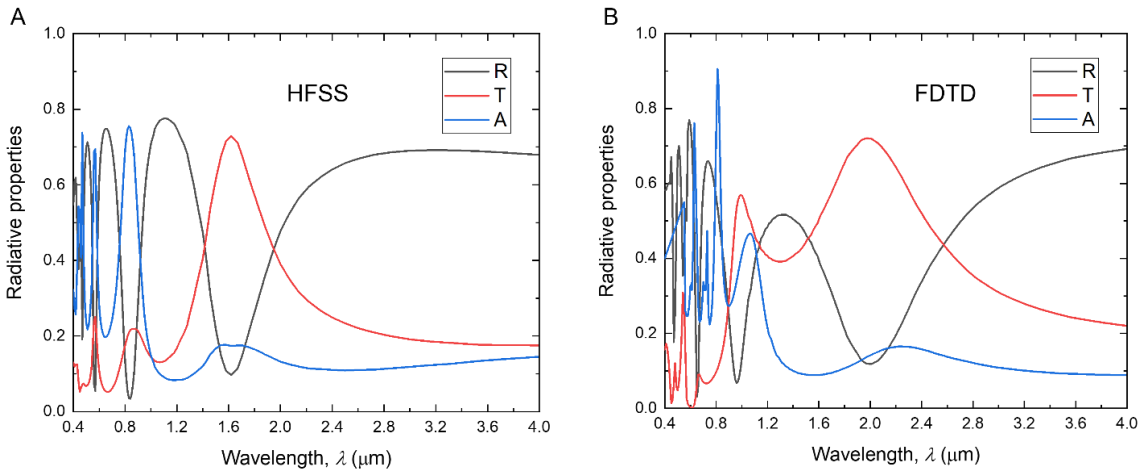

Figure 30: The spectral reflectance, transmittance, and absorptance of the selective metasurface filter at normal incidence for TM polarized light based on (a) HFSS and (b) FDTD simulations with nanopillar diameter, d = 370 nm with period, a = 450 nm and heigh, h = 700 nm.

Validation of TPV system efficiency calculations:

The TPV system efficiency calculations were first validated by obtaining results from literature [105]. The cell IQE and absorptance obtained from Tang et al. [70] are plotted along with the refractive index (*n*) and extinction coefficient (*k*) of GaSb [106] as shown in Figure 31 :

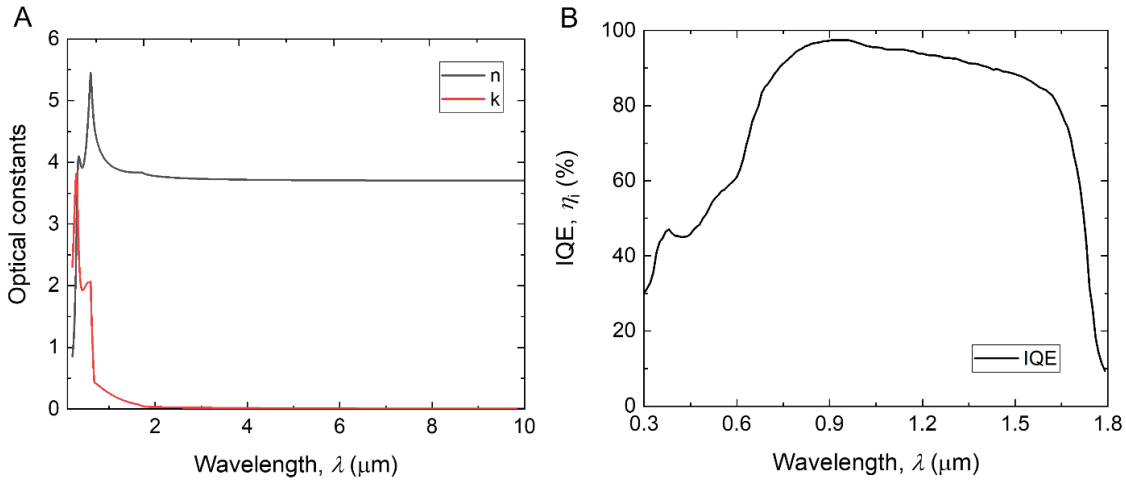

Figure 31: (a) The refractive index (*n*) and extinction coefficient (*k*) of GaSb cell obtained from adachi. (b) The IQE of GaSb cell used in the study obtained from Tang et al.

The emitter and the cell efficiency were plotted as a function of emitter temperature for the validation using the calculation method used in this paper as shown in Figure 32.

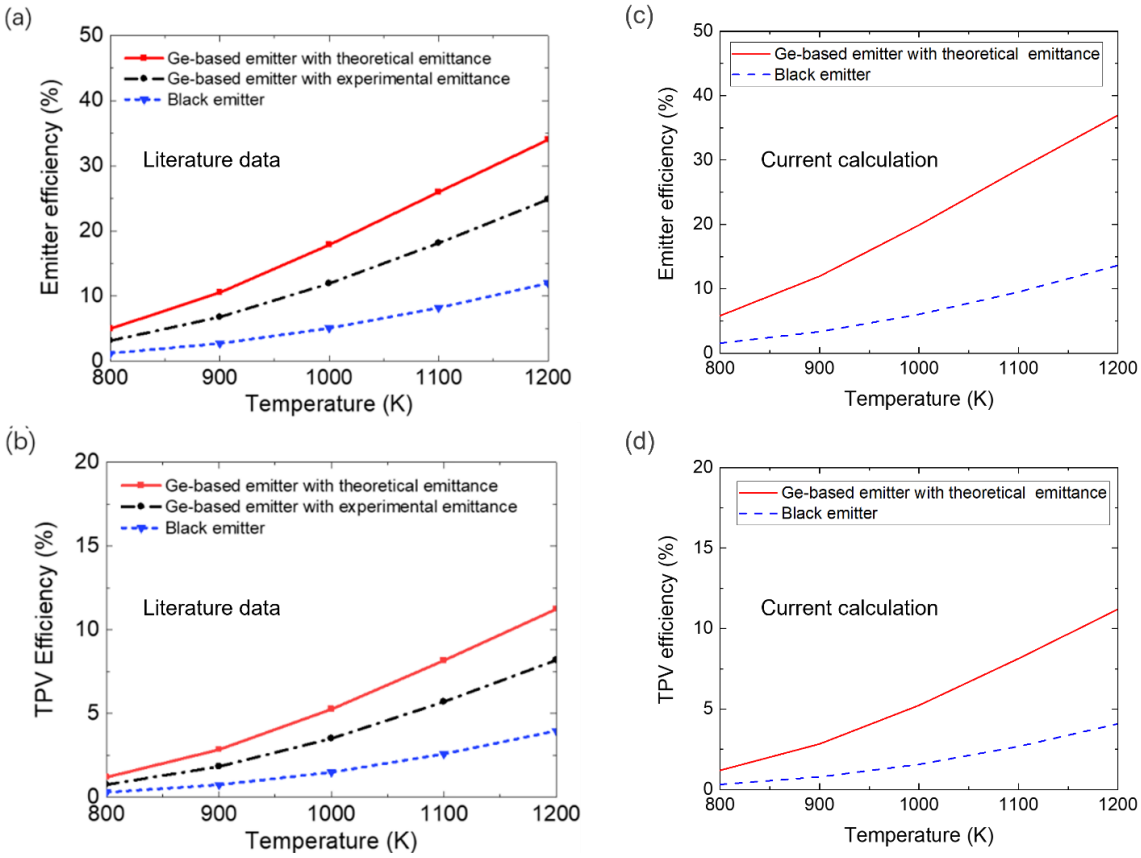

Figure 32: (a) Spectral efficiency (literature), (b) TPV efficiency (literature), (c) Spectral efficiency (current calculation) and (d) TPV efficiency (current calculation) at different temperatures from 800 K to 1200 K with theoretical Ge-based emitter, fabricated Ge-based emitter and black emitter paired with a GaSb cell.

Proposed Fabrication process and other structural design

Previously, ultrathin anodized aluminum oxide (AAO) templates were utilized to create periodic nanostructures quickly and cheaply[107]–[109]. Here AAO templates will be used in the proposed fabrication of aluminum nanopillar (AlNP) metasurface filter. The proposed filter design can be fabricated in a 3-step process. AAO templates can be purchased from commercial vendors (TopMembranes UT450-370-1200). Firstly, the purchased AAO

templates comes on a PMMA layer due to its fragility because of their microscale thickness. The template is dipped in acetone to remove the PMMA layer and then transferred on to the quartz substrate. Next, aluminum can be deposited onto the sample via e-beam deposition and finally the Kapton tape can be used to peel off the AAO layer leaving behind the aluminum nanopillar on the quartz substrate. The proposed fabrication process is simple and inexpensive. Few challenges associated with the proposed fabrication process can be the uniformity of structures over a large area and irregularities in the height of nanopillar structures because of the wrinkles that can be formed during the template transfer process.

Absorption plots varying with geometric parameters of the nanowires:

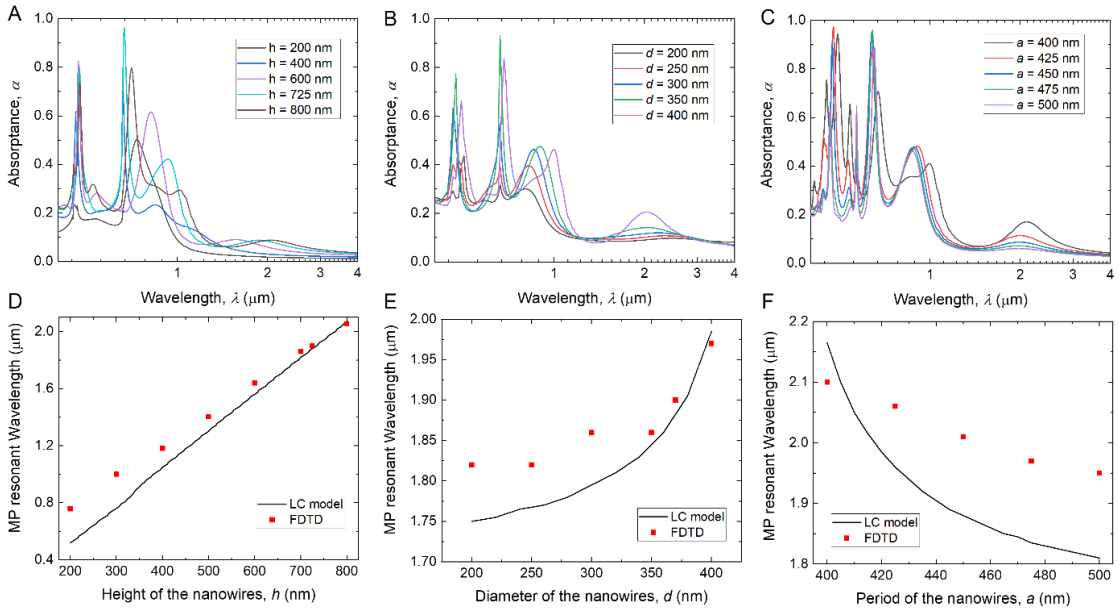

Figure 33: The spectral absorptance with respect to different nanopillars: (a) diameter, (b) height and (c) period simulated by FDTD. The MP1 wavelengths predicted by FDTD, and LC circuit model with respect to different nanopillars: (d) diameter, (e) height and (f) period.

For reference to section 0 in the main text the absorption of metasurface was plotted varying with the geometrical properties of the nanopillar. The absorption plots shown in the Figure 33 verify the existence of MP and the variation of MP resonance peak wavelength with geometric parameters like the diameter, heigh and the period of aluminum nanopillars on the quartz substrate.

GaSb TPV cell with different below bandgap (bbg) absorptance

The nominal value of the bbg absorptance of the cell was varied to check its effect on the cell performance parameters. Figure 34(a) and (b) show that the spectral and the overall TPV efficiency is dependent on the bbg absorptance. At low bbg absorptance, both the efficiencies improve and start decreasing with an increase in the value of absorptance below the bandgap of the GaSb cell. From Figure 34(c) we can observe that the bbg absorptance of the cell primarily affects the net radiative heat flux to the cell. Due to higher absorptance below the bandgap, the cell absorbs incoming radiation in this energy regime that does not promote the carrier generation and hence not contributing to useful power output. Figure 34(d) shows that the power output is not varying with respect to bbg absorptance.

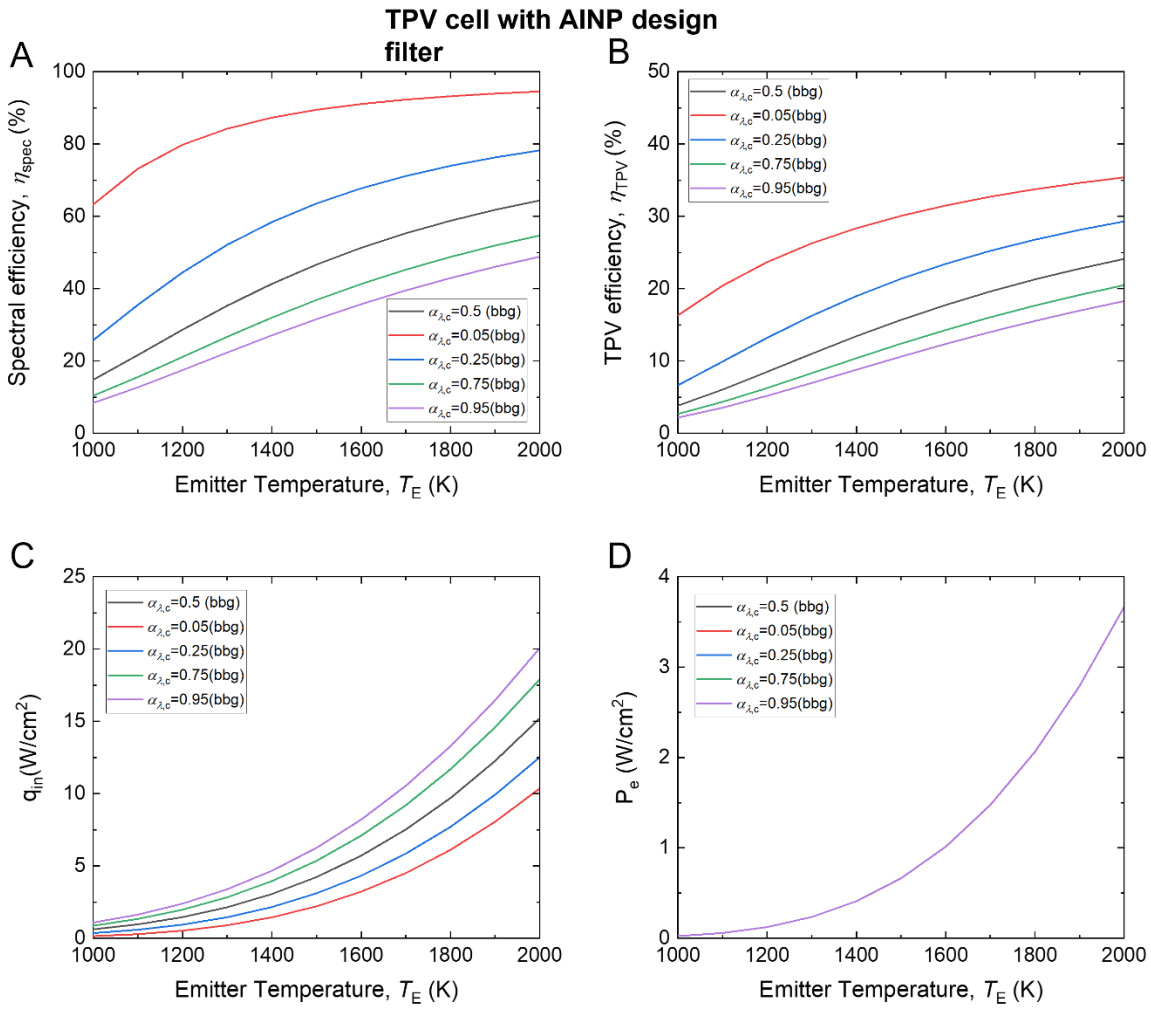

Figure 34: (a) Spectral efficiency, (b) TPV efficiency, (c) net radiative heat flux and (d) output power at different temperatures from 1000 K to 2000 K with theoretical AlNP metasurface filter, and black emitter paired with a GaSb cell for different bbg absorptance of the cell.

FDTD Convergence absorptance plots

With nonuniform meshing, a minimum mesh size of 5 nm is employed, and the numerical error is less than 1% when compared to a simulation with a minimum element size of 3 nm.

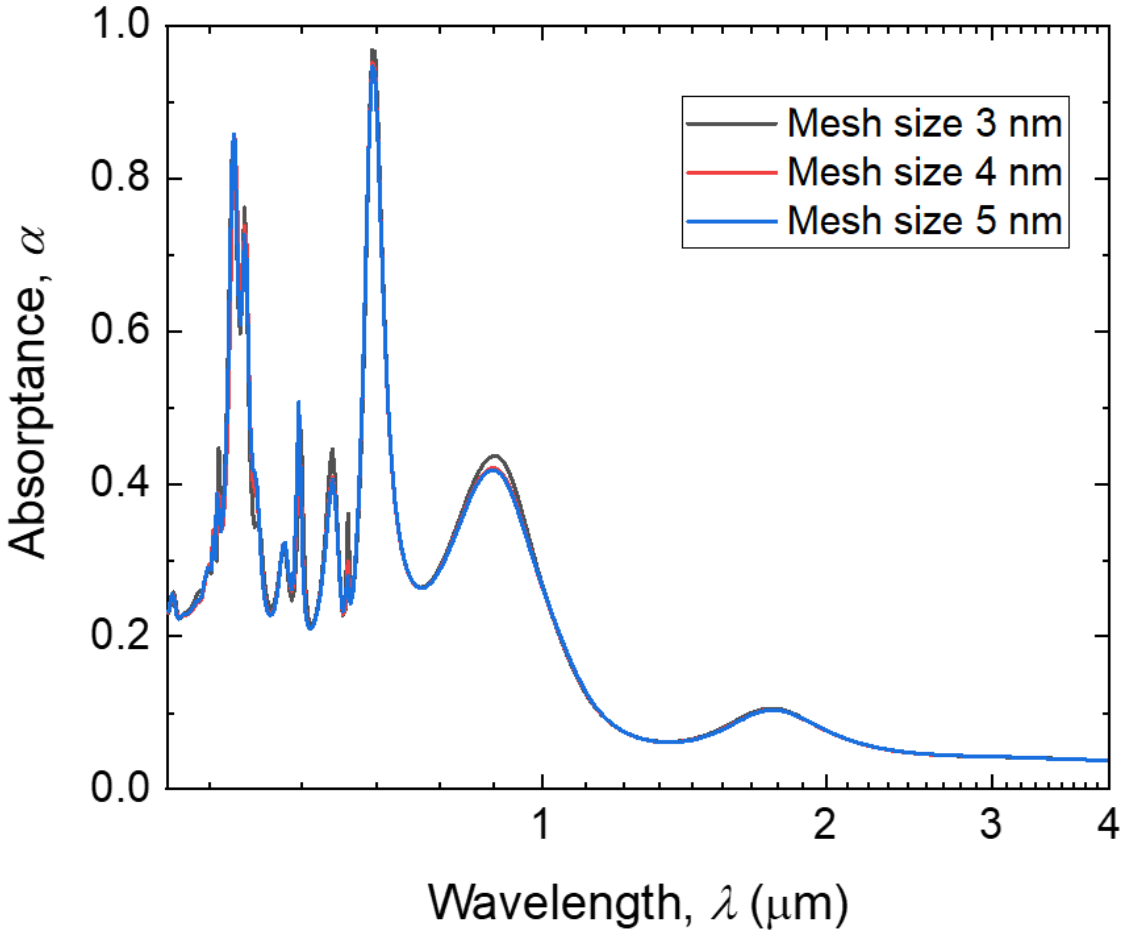

Figure 35: Convergence plot for FDTD comparing the absorptance of the metasurface structure for mesh sizes 3, 4 and 5 nm.

APPENDIX B

NANOPOROUS GOLD THERMAL PROPERTIES AND HEATER SETUP

Pore volume fraction calculation

The apparent pore volume fraction (APVF) f, of the samples can be calculated as a function of initial volume fraction of silver and residual silver content after dealloying.

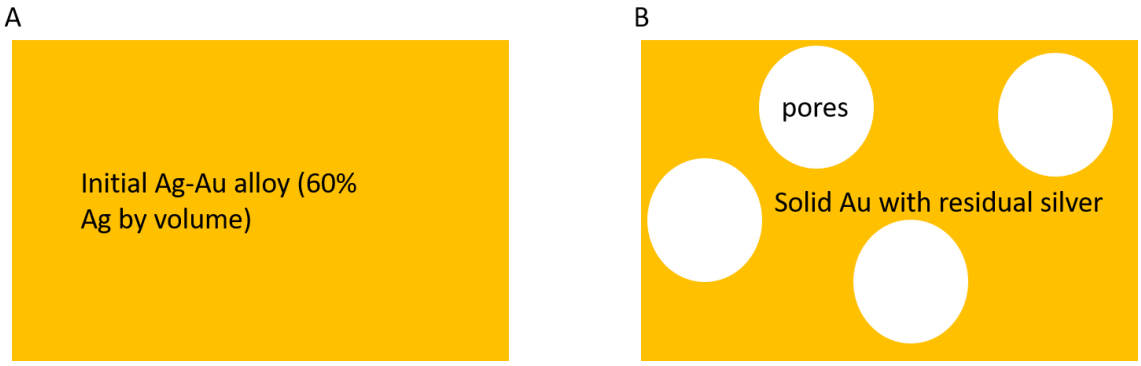

Figure 36: (a) Initial Ag-Au alloy after co-sputtering with 60% of Ag by volume. (b) Porous gold layer after dealloying for 30 mins at 40 °C containing 1-3% of residual silver content.

The initial volume of the co-sputtered Ag-Au alloy and the final volume of the dealloyed sample from Figure 36 can be defined in the following manner:

$$Vf_{Au}^{i} \times V_{total} + Vf_{Ag}^{i} \times V_{total} = V_{total}^{i} \quad (1)$$

$$Vf_{Au}^{f} \times V_{solid} + Vf_{Ag}^{f} \times V_{solid} + V_{pores} = V_{total}^{f} \quad (2)$$

where Vf_{Au}^{i} is the initial volume fraction of gold, and Vf_{Ag}^{i} is the initial volume fraction of silver. Vf_{Au}^{f} is the final volume fraction of gold, Vf_{Ag}^{f} is the final volume fraction of silver, V_{solid} is the total final volume of the solid, and V_{pores} is the total final volume of pores after dealloying. Assuming the volume of the layer does not shrink, we can safely assume the volume of the layer before and after the dealloying process are the same, i.e., $V_{total}^{i} = V_{total}^{f} = V_{total}$. The leads to the following equation:

$$Vf_{Au}^{i} \times V_{total} + Vf_{Ag}^{i} \times V_{total} = Vf_{Au}^{f} \times V_{solid} + Vf_{Ag}^{f} \times V_{solid} + V_{pores} \quad (3)$$

Another important assumption is that gold does not get etched during the dealloying process leads to the next equation:

$$Vf_{Au}^{f} \times V_{solid} = Vf_{Au}^{i} \times V_{total} \quad (4)$$

Substituting for $Vf_{Au}^{f} \times V_{solid}$ in eq. (3) as $Vf_{Au}^{i} \times V_{total}$ from eq. (4), we get:

$$Vf_{Ag}^{i} = Vf_{Ag}^{f} \times \frac{V_{solid}}{V_{total}} + \frac{V_{pores}}{V_{total}} \quad (5)$$

Using the relation $\frac{V_{solid}}{V_{total}} + \frac{V_{pores}}{V_{total}} = 1$, we get our final relation for the APVF (f) as:

$$f = \frac{V_{pores}}{V_{total}} = \frac{Vf_{Ag}^{i} - Vf_{Ag}^{f}}{1 - Vf_{Ag}^{f}} \quad (6)$$

Heat transfer resistance network

The in-situ thermal reflectance setup employs a K-type thermocouple (TC) to measure the temperature on nickel-coated copper plate T1, below the glass slide. Note that the distance between the sample surface to the center of copper (where the thermistor is located) is considered to be half the thickness of the copper plate to which the sample is fastened with estimated contact resistance $R_{contact}$ between the copper plate and the glass slide as small as 50 e^{-6} $m^2K\ W^{-1}$ and the thermal resistance value through different films R_{films} as 50 e^{-6} $m^2K\ W^{-1}$ (see Figure 37(a) for a detailed 3D numerical analysis for temperature distribution). According to the equivalent thermal resistance diagram in Figure

37(b), one-dimensional heat transfer through the glass slide can be determined in a steady state, without considering the radiation loss from the sides and the temperature of the sample can be estimated as:

$$\frac{T_1 - T_s}{R_{Cu} + R_{contact} + R_{Sub} + R_{films}} = h\,(T_s - T_a) + \varepsilon_s(T_s^4 - T_a^4) \qquad 7$$

The modeling was done and temperature difference between the thermocouple measurement and the porous gold layer will be <7 °C for a temperature measurement of 500 °C by the TC.

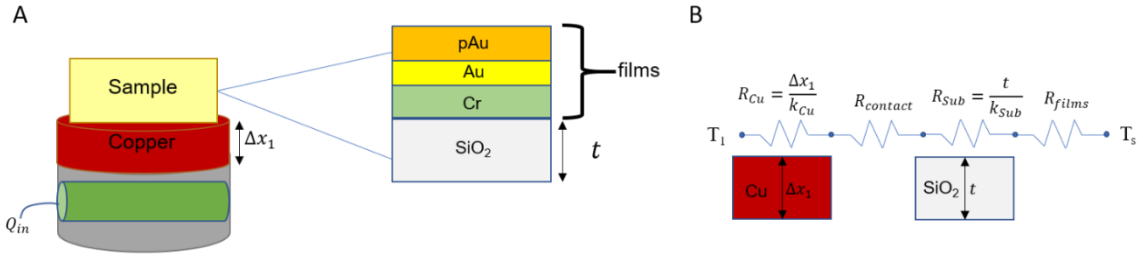

Figure 37: In-situ temperature measurement setup and heat transfer model. (a) Illustration of the sample holder setup. (b) Equivalent thermal resistance network.

Reference Silicon sample measurement for IS setup

We measured the TE and TM polarized reflectance again with undoped silicon sample at shorter spectrum from 0.4 to 0.9 μm for incidence angles 10º, 30º, 45º, and 60º, which match very well with the modeling results as shown in Figure 38 (b) and (c) with 5% acceptable difference.

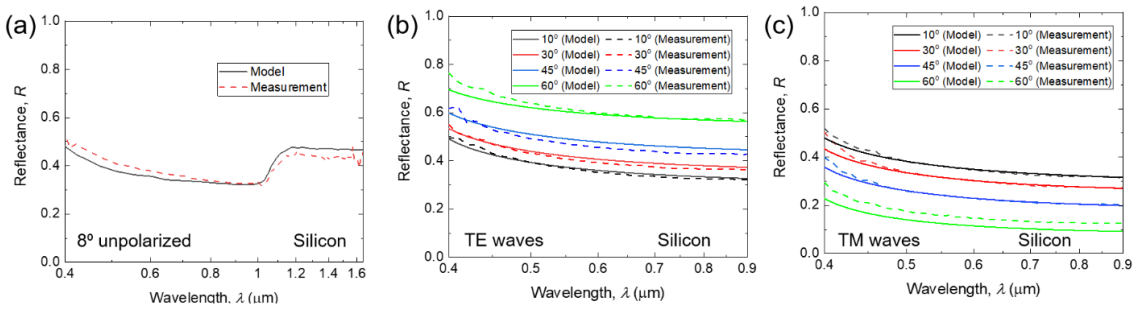

Figure 38: Validations of spectral optical reflectance measurements with the integrating sphere in comparison with theoretical modelling: (a) spectral near-normal hemispherical reflectance of undoped silicon wafer at room temperature; (b) spectral directional hemispherical reflectance of undoped silicon wafer at multiple incidence angles (i.e., 10º, 30º, 45º, and 60º) for TE polarized waves and (c) TM polarized waves.

Reference Silicon sample measurement for in-situ setup

Silicon sample was installed on to the heater setup and the collimator was adjusted to obtain maximum reflected signal intensity (S_{Si}) of the broadband light. The sample setup is replaced by silver mirror (S_{Ag}) which is used as the background. The measurements were done three times and the reflectance value was averaged. The measured reflectance value of the silicon (R_{Si}) is calculated by obtaining the reflected signal ratio from silicon to the silver mirror and corrected using the theoretical reflectance value of silver (R_{Ag}) whose

optical constants are obtained from Palik data [80] and compared to the theoretical reflectance of silicon as shown in Figure 39.

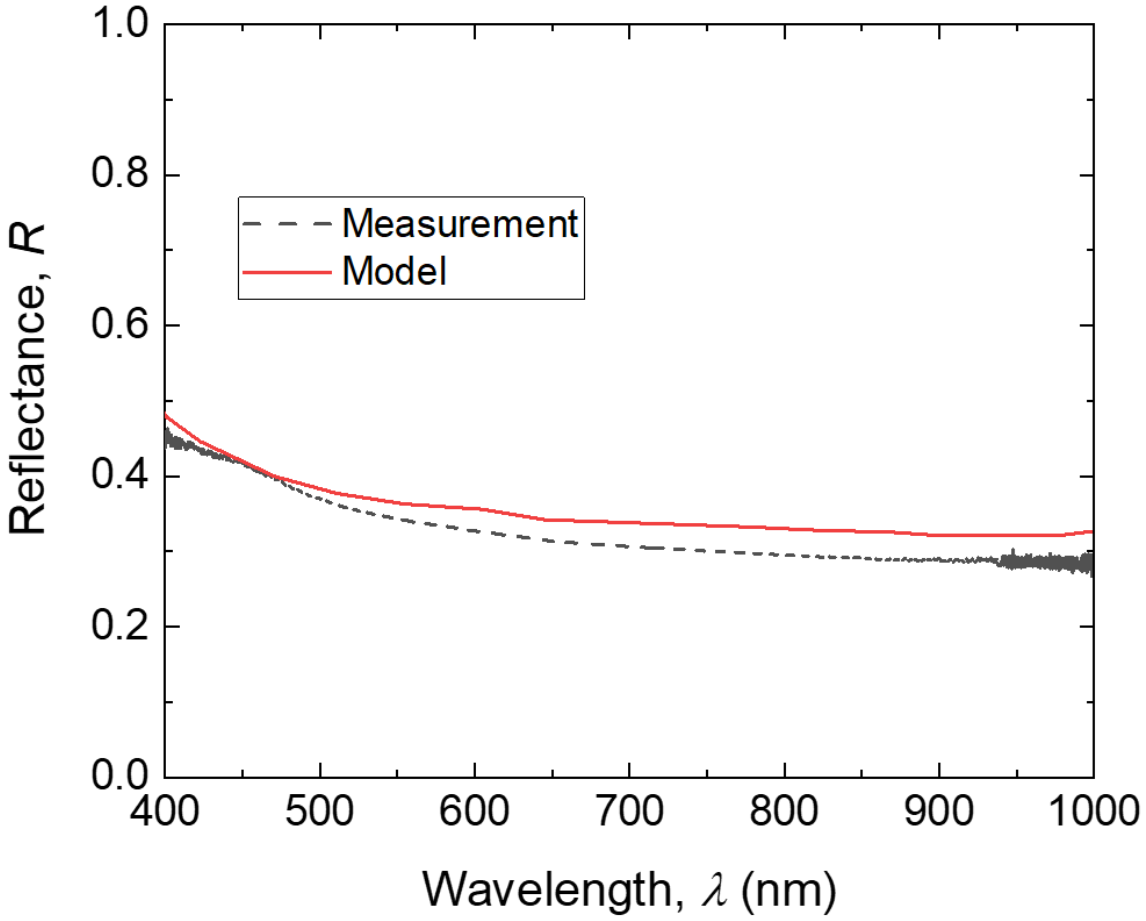

Figure 39: Near normal specular reflectance of lightly doped silicon measured using the in-situ temperature dependent reflectance fiber-optic setup compared to the theoretical value.

Heater setup

The heater setup consisted of nickel-plated copper disk of diameter 1.688 inch and thickness 0.125 inch as shown in Figure 40(a). The copper disk had four thru screw holes of diameter 0.140 inch to attach the sample and four threaded thru holes to fasten #6-32 screws to the stainless-steel base. The stainless-steel base of diameter 1.688 inch and thickness 0.55 inch had two thru holes along the circumference of 0.75-inch diameter to press fit the cartridge heater as shown in Figure 40(b). The cartridge heater CSH-101100 manufactured by omega with outer diameter 0.75 inch and length 5 inch was press fitted in the stainless-steel cage. The cartridge heater is designed and manufactured with 300

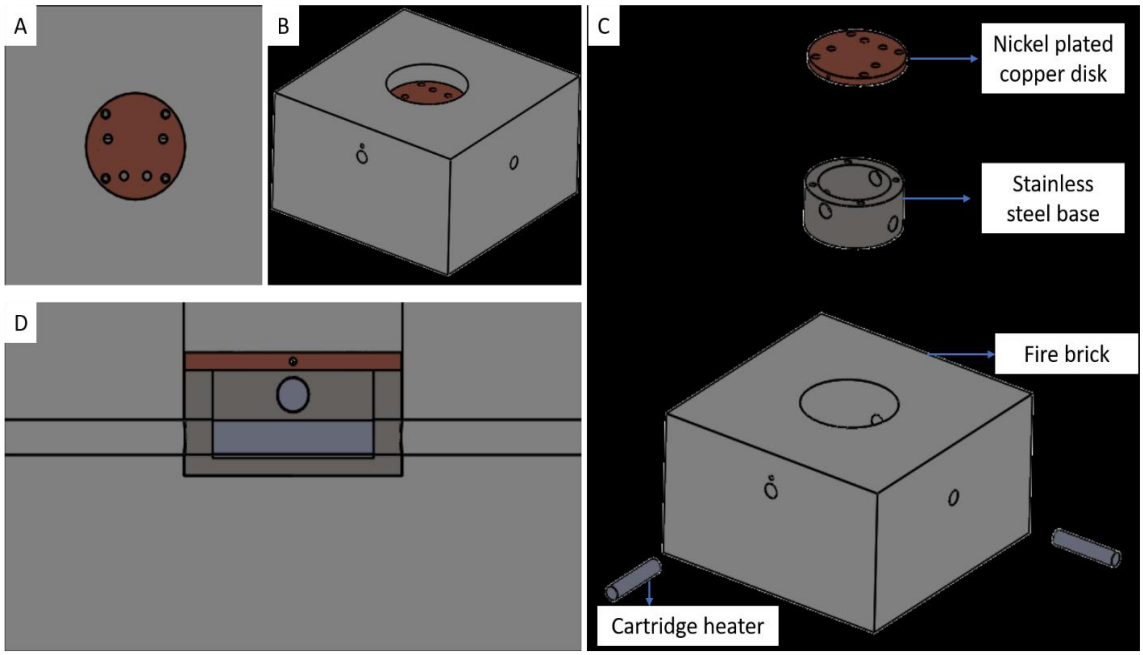

Figure 40: (a) Front view of the nickel-plated copper disk with diameter 1.688 inch containing 4 thru threaded holes to attach the sample and 4 thru holes to fasten to the steel base. (b) Isometric view of the heater setup encapsulated by firebrick. (c) Exploded view showing cartridge heater, fire brick, steel base and nickel-plated copper disk. (d) Side view of the heater setup showing the press fitted cartridge heater, fire brick, steel base

series stainless steel sheaths to precise dimensions and tolerances to ensure maximum heat

transfer for minimum core temperature and faster heating. The heater was rated at a maximum sheath temperature 760 °C. The entire heater setup was encapsulated by a fire brick to prevent the aluminum outer cage from getting to hot temperatures.

The power to the cartridge heater was provided by a transformer controlled by the PID controller manufactured by Omega (model number: CSi8D). The measurements were taken when the system was underdamped with an overshoot of 10 °C. The PID controller was controlled by a lab view interface where the required temperature is given as the input,

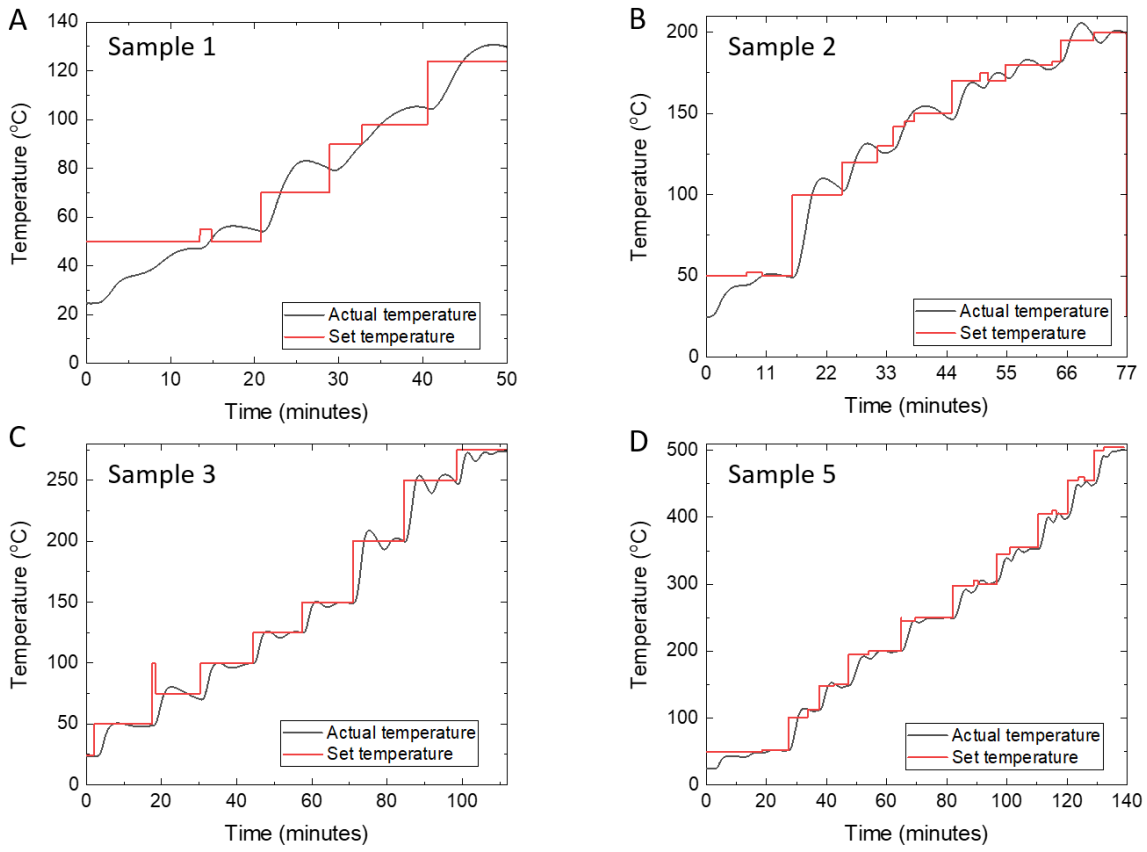

Figure 41: Temperature histogram of sample (a) 1, (b) 2, (c) 3, and (d) 5

and the controller cuts off the transformer once the set temperature is reached. The temperature histograms of the sample temperatures are presented below in Figure 41.

The reflectance measurements were collected at 0, 2 and 5 min after each temperature increment crosses the setpoint and the results were then averaged for a given setpoint temperature. Figure 42 shows the time dependent specular reflectance at the maximum exposed temperature of the sample.

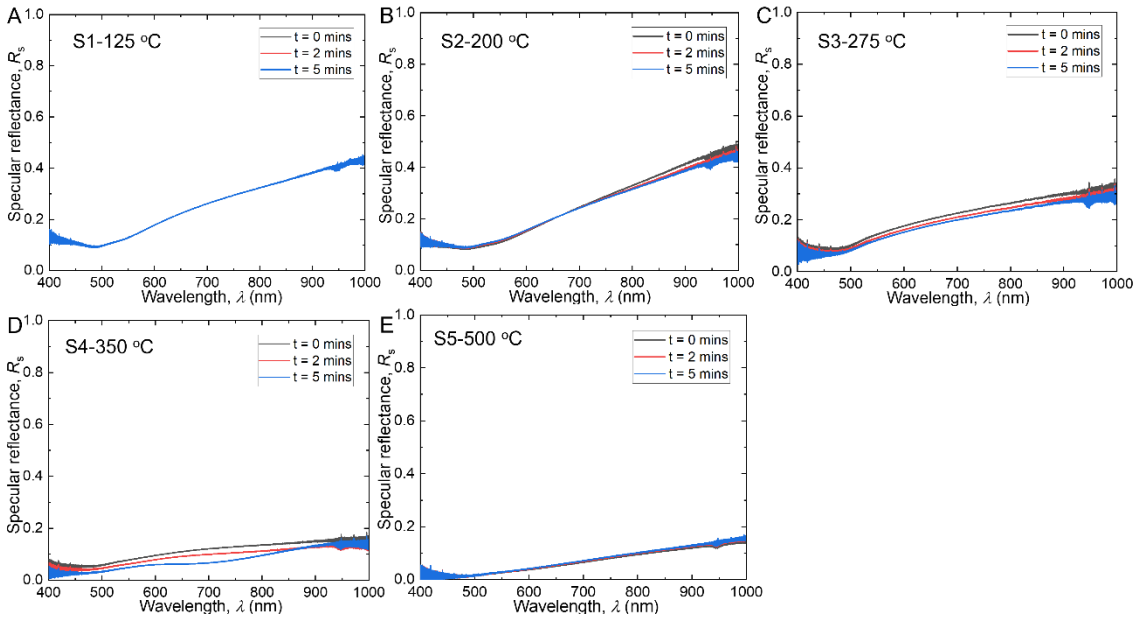

Figure 42: Time dependent specular reflectance of samples measured at 0,2 and 5 mins at the maximum exposed temperature (a) S1-125 ^{o}C, (b) S2-250 ^{o}C, (c) S3-275 ^{o}C, (d) S4-350 ^{o}C and (e) S5-500 ^{o}C

Temperature and apparent pore volume fraction effect on the reflectance calculation

There is negligible change in the reflectance calculated with respect to temperatures up to 500 °C for the wavelength regime considered in this paper. The refractive index (n)

and the extinction coefficient (k) is plotted as a function of temperature in Figure 43 (a) and (b) respectively.

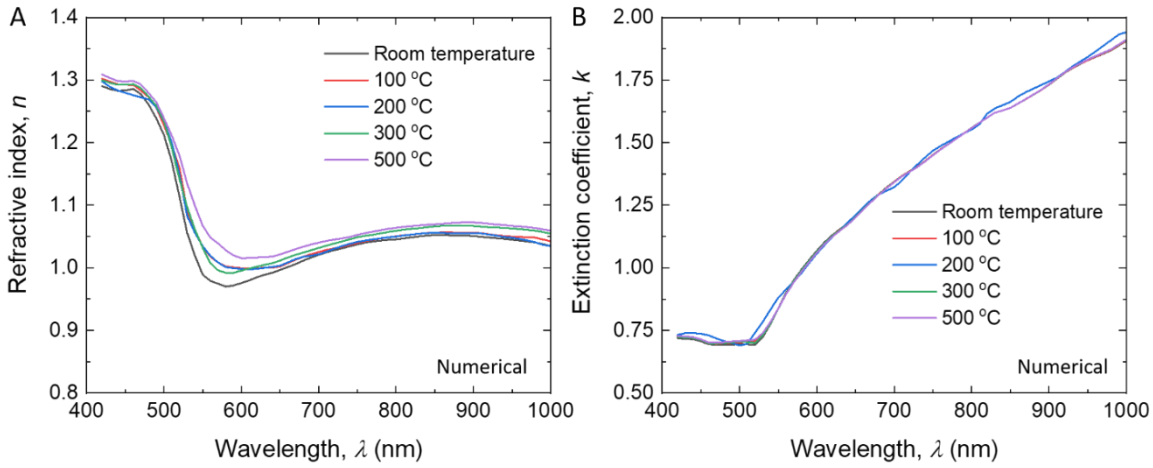

Figure 43: (a) Refractive index n, (b) extinction coefficient k of the nanoporous gold in the wavelength range from 400 to 1000 nm calculated from the BR effective medium theory at different temperatures for a fixed volume fraction of f = 58%.

In fact, by taking the dielectric function of gold at 500 °C [110] in the Bruggeman effective medium model, the calculated optical reflectance changes very little compared to the case calculated using dielectric function of gold at room temperature as shown in Figure 44(a), which confirms the negligible effect of temperature on the dielectric function of gold for the considered wavelength range in this paper. Since the initially calculated apparent volume fraction have the same value, the calculated hemispherical reflectance do not show much variance as seen from Figure 44(b).

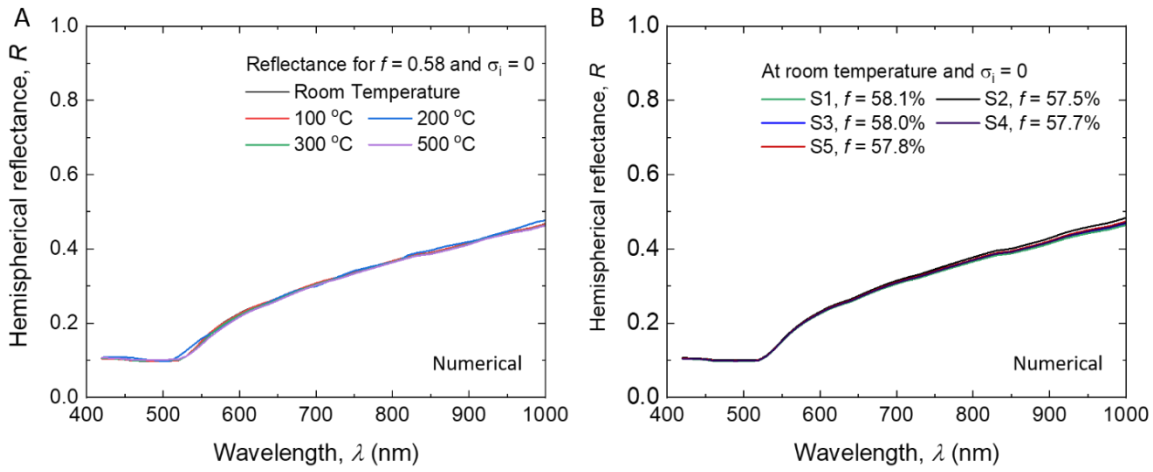

Figure 44: Predicted spectral normal reflectance of semi-infinite nanoporous gold (a) with varying dielectric function of gold thin film as a function of temperature (b) with different pore volume fractions of the samples from the optical modeling.

APPENDIX C

POWDER OPTICAL MODEL SUPPORTING MATERIAL

XRD data for porous copper powders

The XRD data for the porous copper powder suggested that there was 46.1% of Cu_2O by weight. This is seen from Figure 45.

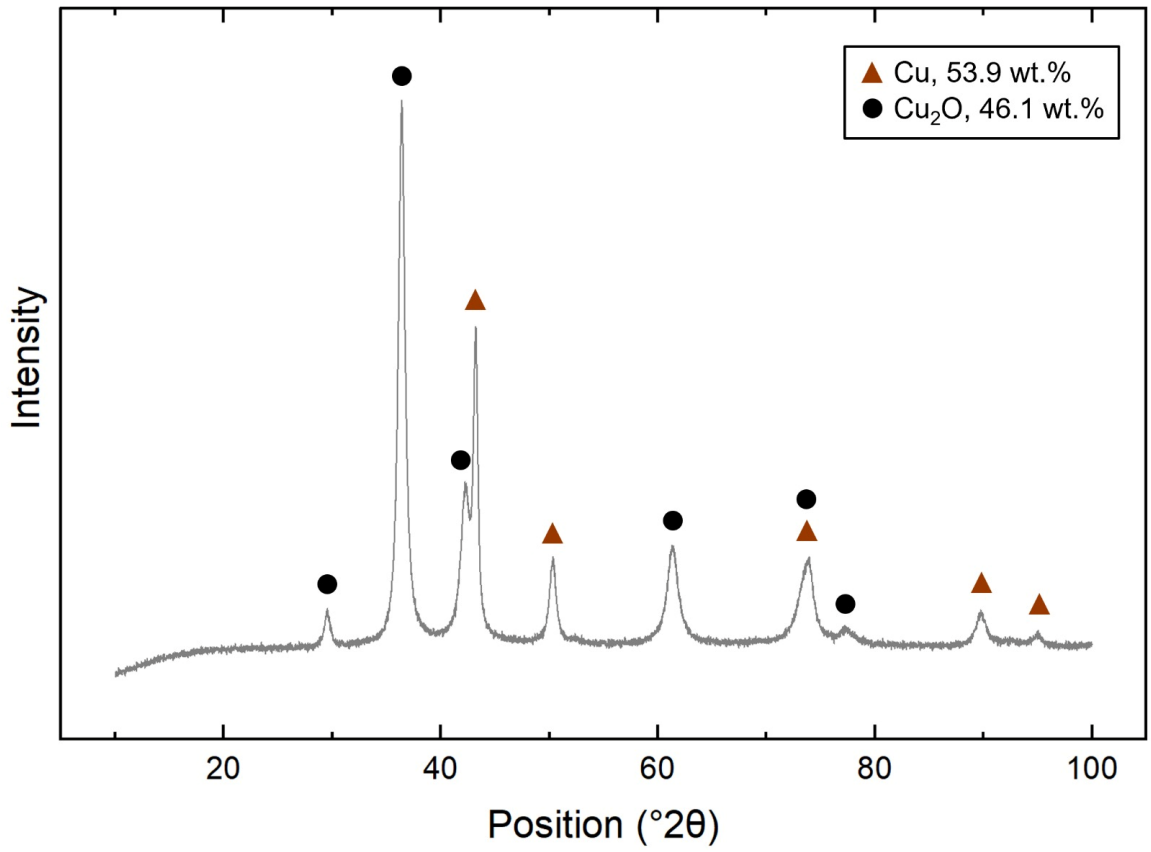

Figure 45: XRD data for porous copper powder suggesting the presence of 46.1% of Cu_2O by weight.

Surface area fraction derivation

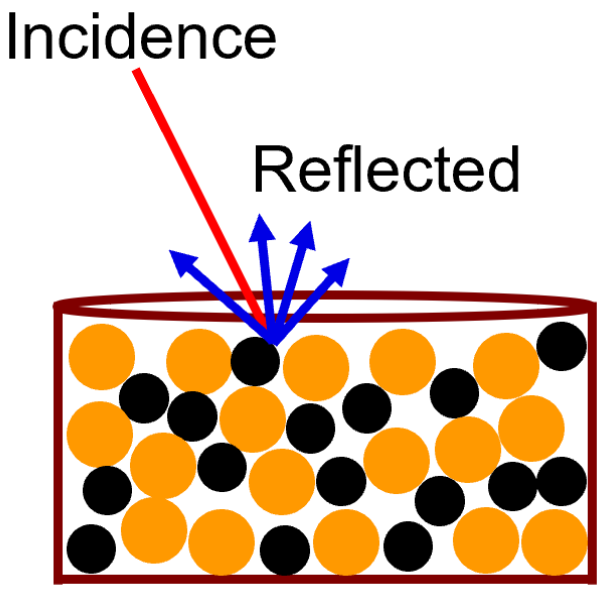

Figure 46: Schematic of porous copper and copper powder mixture reflectance calculation using the checkerboard method.

Consider mixtures of copper and porous copper powders in different weight proportions as shown in Figure 46. The reflectance of opaque particles has been shown to depend on only the properties of the specimen surface area and hence the reflectance of the mixtures can be calculated as a function of their surface area fractions as per the linear or the checkerboard model presented in the main text.

The total surface area of particles of any specific shape can be shown to be inversely proportional to the average particle size and to the average particle density, i.e., the percent surface area of component B in a binary mixture of A and B is:

$$S_B = \frac{W_B \rho_A d_A}{W_B \rho_A d_A + W_A \rho_B d_B} \quad (1)$$

W_A and W_B are the weight fractions (wt.%) of Cu and PCu in the powder mixture respectively; ρ_A and ρ_B, the measured apparent densities of Cu and PCu powders and d_A and d_B are the diameters of copper and porous copper powders.

To derive the above equation for surface area fraction, we start with the volumes of the copper and porous copper powders:

The total volume of the mixture *V is:*

$$V = V_A + V_B \tag{2}$$

Assuming particles of spherical shape, volume of sphere $= \frac{4}{3}\pi(\frac{d}{2})^3$ and surface area of sphere $= 4\pi(\frac{d}{2})^2$.

The Surface area to volume ratio for a sphere can hence be defined as:

$$\frac{SA\prime}{V\prime} = \frac{6}{d} \tag{3}$$

The total surface area of the powder mixture can be defined as the sum of their individual surface areas:

$$SA = SA_A + SA_B \tag{4}$$

Then we can write the surface area fraction of porous copper, S_B:

$$S_B(\%) = \frac{SA_B}{SA_A + SA_B} = \frac{\frac{6V_B}{d_B}}{\frac{6V_A}{d_A} + \frac{6V_B}{d_B}} \tag{5}$$

Dividing and multiplying eq. (5) by $V_A + V_B$ we get surface area fraction in terms of volume fraction, we get:

$$S_B(\%) = \frac{\frac{6V_B}{d_B}}{\frac{6V_A}{d_A} + \frac{6V_B}{d_B}} = \frac{\frac{f_B}{d_B}}{\frac{f_A}{d_A} + \frac{f_B}{d_B}} \tag{6}$$

Substituting density, $\rho = \frac{M}{V}$ in eq. (6), we obtain surface area fraction in terms of weight fraction as follows:

$$S_B(\%) = \frac{\frac{f_B}{d_B}}{\frac{f_A}{d_A} + \frac{f_B}{d_B}} = \frac{\frac{w_B}{\rho_B d_B}}{\frac{w_A}{\rho_A d_A} + \frac{w_B}{\rho_B d_B}} \tag{7}$$

Eq. (7) can be rearranged to obtain eq. (1).

Sensitivity Analysis

The diameters of the particles were the only arbitrarily chosen values in the determination of the surface area fraction values. In order to justify the selection of the specific diameter values for d_A and d_B, a sensitivity analysis was performed as shown in Figure 47. The diameter of these particles were varied within the upper and lower bound values, i.e., the diameter of PCu particles (d_B) was varied from 5-25 μm for a fixed copper

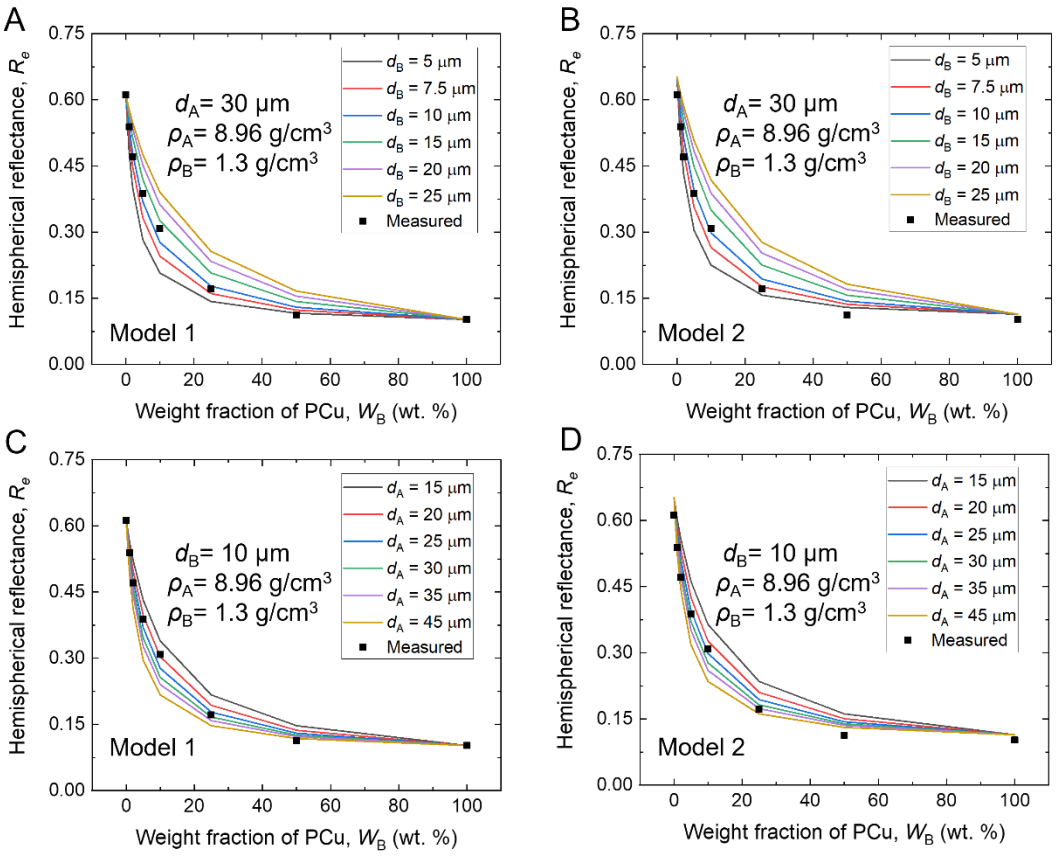

Figure 47: Sensitivity analysis showing the reflectance of a function of varying weight fractions of porous copper in the powder mixture for changing d_B from 5-25 μm and fixed d_A of 30 μm using (a) Model 1 (b) Model 2 and changing d_A from 15-45 μm and fixed d_B of 10 μm using (a) Model 1 (b) Model 2 at a wavelength of 2 μm.

particle diameter 30 µm and the diameter of Cu particles (d_A) was varied from 15-45 µm for a fixed porous copper particle diameter 10 µm. The calculated reflectance using model 1 and 2 was plotted as a function of varying weight fractions of porous copper in the powder mixture to compare with the experimental results. The analysis concluded that the best fit was obtained when d_A= 30µm and d_B= 10 µm. This analysis was also performed at the laser wavelength of 1.07 µm to obtain more accurate results from the optical models discussed in the main text.

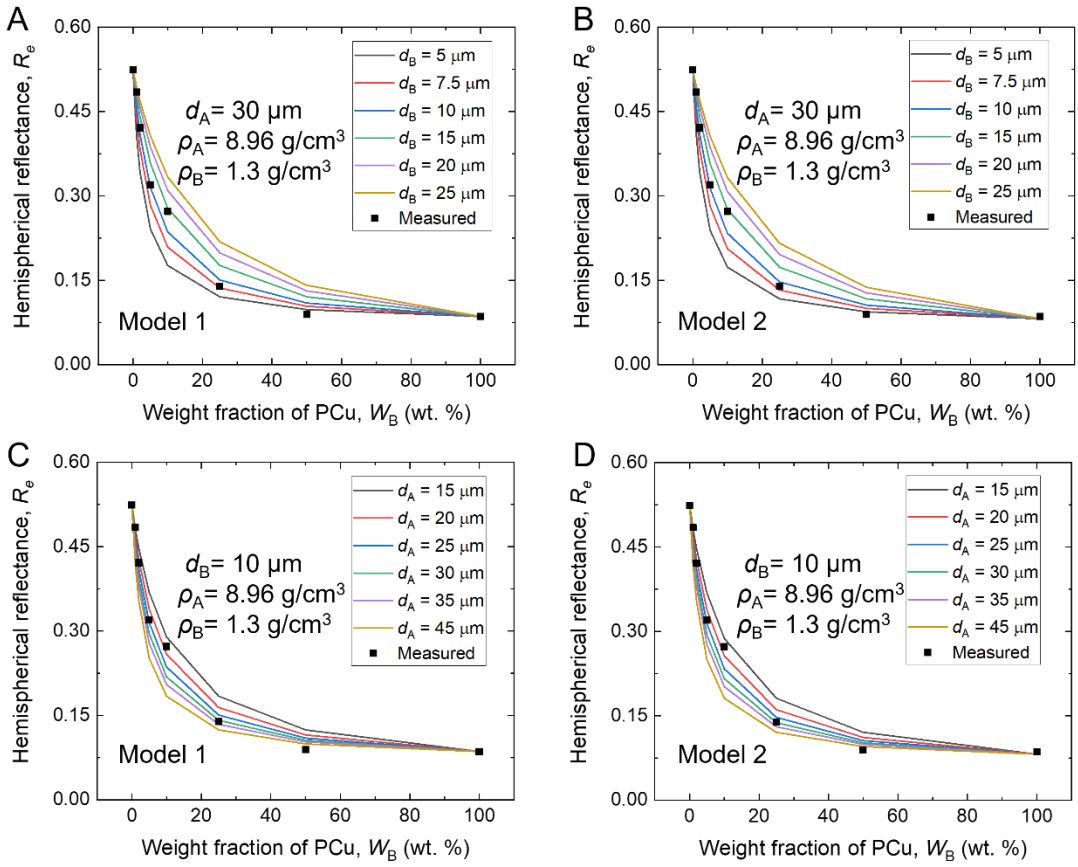

Figure 48: Sensitivity analysis showing the reflectance of a function of varying weight fractions of porous copper in the powder mixture for changing d_B from 5-25 µm and fixed d_A of 30 µm using (a) Model 1 (b) Model 2 and changing d_A from 15-45 µm and fixed d_B of 10 µm using (a) Model 1 (b) Model 2 at a wavelength of 1.07 µm.